Temperature Programmed Desorption and Infrared Spectroscopic Studies of Interfacial Hydrogen Bonds for Small Molecules Adsorbed on Silica and Within Metal Organic Frameworks

Joshua Erold Robert Abelard

Thesis submitted to the faculty of the Virginia Polytechnic Institute and State University in partial fulfillment of the requirements for the degree of

Doctor of Philosophy
In
Chemistry

John R. Morris, Chair

Amanda J. Morris

Brian M. Tissue

Diego Troya

April 13, 2017

Blacksburg, VA

Keywords: Vacuum, Surface, Aromatic, Benzene, Mustard, Chemical Warfare Agent,

Silica, Hydrogen Bond, Metal Organic Framework

Temperature Programmed Desorption and Infrared Spectroscopic Studies of Interfacial Hydrogen Bonds for Small Molecules Adsorbed on Silica and Within Metal Organic Frameworks

Joshua Erold Robert Abelard

Abstract

Hydrogen bonds are arguably the most important reversible intermolecular forces. However, surprisingly few studies of their fundamental nature at the gas-surface interface have been performed. Our research investigated sulfur mustard (HD) adsorption by characterizing interfacial hydrogen bonding and dispersion forces for the simulant molecules 2-chloroethyl ethyl sulfide (2-CEES) and methyl salicylate on well-characterized hydroxyl-functionalized surfaces (silica and UiO-66). Our approach utilized infrared spectroscopy to study specific surface-molecule interactions and temperature-programmed desorption to measure activation energies of desorption. 2-CEES has two polar functional groups, the chloro and thioether moieties, available to accept hydrogen bonds from free surface silanol groups. Diethyl sulfide and chlorobutane were investigated to independently assess the roles of the chloro and thioester moieties in the overall adsorption mechanism and to explore the interplay between the charge transfer and electrostatic contributions to total hydrogen bond strength. The results indicate that both SiOH---Cl and SiOH---S hydrogen bonds form when 2-CEES adsorbs to silica or hydroxylated UiO-66. However, a more stable configuration in which both polar groups interact simultaneously with adjacent silanol groups likely does not form. A systematic study of chloroalkanes revealed that dispersion forces involving the methylene units in 2-CEES contribute to nearly half of the total activation energy for desorption from silica. Methyl salicylate possesses aromatic, hydroxyl, and ester functional groups, each of which is a potential hydrogen bond acceptor. We found that uptake on silica is mainly driven by the formation of carbonyl-silanol and hydroxyl-silanol hydrogen bonds with additional contributions from weaker interactions. In an effort to learn more about the SiOH---π bond, the adsorption of simple substituted benzene derivatives on silica was investigated to probe the effects of electron withdrawing and donating substituents. Results indicate that the substituted benzene derivatives adsorb to silica via a cooperative effect involving SiOH---π hydrogen bonds and additional substituent−surface interactions. The strength of the SiOH---π bond is enhanced by electron donating groups and weakened by electron withdrawing groups.

Temperature Programmed Desorption and Infrared Spectroscopic Studies of Interfacial Hydrogen Bonds for Small Molecules Adsorbed on Silica and Within Metal Organic Frameworks

Joshua Erold Robert Abelard

General Audience Abstract

Hydrogen bonding and dispersion forces are arguably the most important reversible intermolecular forces. The fundamental nature of both forces has been studied extensively in the gas and solution phases. However, only a few analogous studies have been performed at the gas-surface interface. The primary objective for the research described here was to investigate the fundamental nature of sulfur mustard (HD) adsorption by characterizing interfacial hydrogen bonding and dispersion forces for the surrogate (simulant) molecules 2-chloroethyl ethyl sulfide (2-CEES) and methyl salicylate. From these studies, we have gained a richer understanding of several types of important hydrogen bonds including SiOH---Cl, SiOH---S, SiOH---π, SiOH---HO, and SiOH---O=C. Additionally, we have measured the strength of surface-adsorbate dispersion forces for methylene units in straight-chain hydrocarbons and halide moieties in substituted benzene derivatives. Together with previous work in the Morris group, this thesis provides the most comprehensive experimental study of interfacial hydrogen bonding and dispersion forces to date. Part of the ultimate impact of this research will be to guide new filtration, decontamination, and soldier protection strategies.

Acknowledgements

The work in this document would not have happened without the support of many people. I specifically want to thank my PhD advisor, Dr. John Morris for his mentorship during my time at Virginia Tech. I thank my labmates for training me on instruments when I was new in the group and collaborating with measurements. I thank my MS advisor Dr. David Thompson for teaching me to see the beauty in science. I thank my parents for showing me by example how to persevere when challenges seem overwhelming. And I thank my close friends in Blacksburg for reminding me that there is more to life than school.

Table of Contents

Chapter 1: Introduction

1.0 Introduction

At room temperature and ambient pressure, more than 1 x 10^{23} gas molecules will collide with a thumbnail-sized surface (1 cm^2) in one second. Each of these collisions has the potential to lead to uptake of the gas-phase molecule on the surface and a subsequent reaction if the surface is reactive. A fundamental understanding of the forces that affect adsorption and chemistry at the gas-surface interface is therefore a crucial step in answering scientific questions that involve gas-phase molecules. Two such questions currently of interest to scientists are the fate of toxic chemicals in the environment (such as industrial waste and chemical warfare agents used in battlefields) and the development of novel materials to protect people from exposure to these chemicals. The research described in this thesis used a variety of analytical methods to determine the uptake mechanisms and adsorbate-surface binding energies (activation energies of desorption) for several small molecules on an important surface at a high level of detail. Specifically, we investigated the nature of sulfur mustard uptake on silica and metal organic frameworks.

In compliance with regulations that restrict work with chemical warfare agents, simulant molecules with lower toxicity but similar properties were used throughout our experiments. Efforts to establish correlations between the observed behavior of simulants and the expected behavior of sulfur mustard prompted further work to better understand the roles of individual moieties, especially methyl, chloro, thioether, and aromatic groups, in adsorption. Furthermore, several of the simulants relevant to sulfur mustard research, such as chloroalkanes and substituted benzene derivatives, are also common industrial waste chemicals. Thus, the experiments performed here contributed to new insights into not only the uptake of toxic chemicals on surfaces but also the

fundamental nature of surface hydrogen bonding and other reversible surface-adsorbate interactions.

1.1 Chemical warfare agents and toxic industrial compounds

1.1.1 History of sulfur mustard and simulants

Sulfur mustard (HD) is a highly dangerous compound that was first identified as a blister-forming skin irritant in the late nineteenth century and then used as a weapon in the First World War by the German Army.[1] HD is a vesicant agent, which means that it rapidly attacks skin and mucous membranes to cause extreme pain, blisters, and severe tissue damage.[2] Exposure to a small amount of HD is not typically fatal if appropriate medical care is available, but survivors suffer from an increased risk of developing cancer. Furthermore, HD has been shown to behave as a teratogen.[3] Alkylation of biomolecules, especially nucleic acids, is the primary chemical pathway responsible for the harmful effects of HD exposure. As shown in **Figure 1**, such reactions simultaneously modify the biomolecule (DNA in the provided example) and produce HCl as a byproduct. Thus the victim suffers from not only cellular damage, but also acid burns.

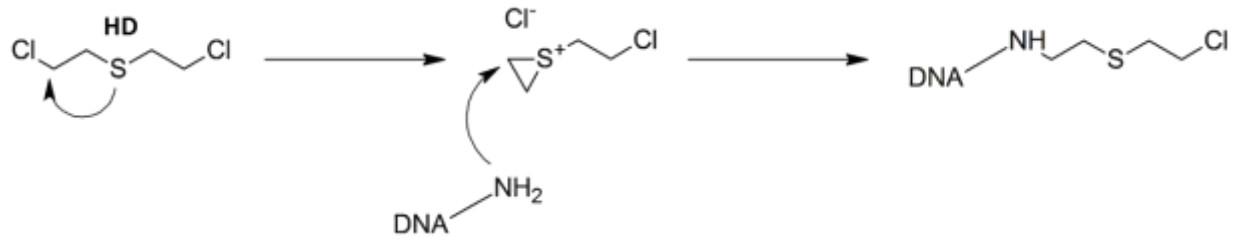

Figure 1. *Reaction of HD with a nucleic acid in DNA.*

Although international treaties after WWII have significantly reduced the likelihood of HD use in warfare, this agent remains a significant threat because it is a simple molecule that can easily be synthesized and used by for terrorism.[4] Furthermore, studies have shown that HD may not readily decompose in the environment and can pose a serious health hazard months or even years

after initial release in an area.[5,6] Therefore, novel methods to clean HD-contaminated surfaces and protect soldiers from exposure remains an important research topic.

Applied research to develop materials, equipment, and strategies for protection and decontamination is well beyond the scope of this thesis. The focus here is to gain fundamental insight into the nature of the surface-adsorbate interactions that drive uptake of HD and to measure the strengths of these interactions. This information can then be used by other researchers to better understand the ability of HD to stick on various surfaces such as sand, military equipment, and sorbent materials intended to trap CWA molecules.

Due to the hazardous nature of CWAs, only a few special research facilities in the US, such as Edgewood Chemical Biological Center (ECBC), have the appropriate certifications and safety measures to work with HD. Research groups without access to those facilities work with simulants, which are molecules that mimic certain chemical or physical properties of the agent but are less toxic. Methyl salicylate, 2-chloroethyl ethyl sulfide (2-CEES), and 2-chloroethyl phenyl sulfide (2-CEPS), and diethyl malonate (DEM) are the most common simulants for HD. Molecular structures for these compounds are provided in **Figure 2**, and **Table 1** lists several of their chemical, toxicological, and physical properties. Among these simulants, 2-CEES has the most similar chemical structure to HD (the only difference is the substitution of a chlorine atom by a hydrogen atom) and is therefore a logical choice for studies that investigate chemical reactivity of HD.

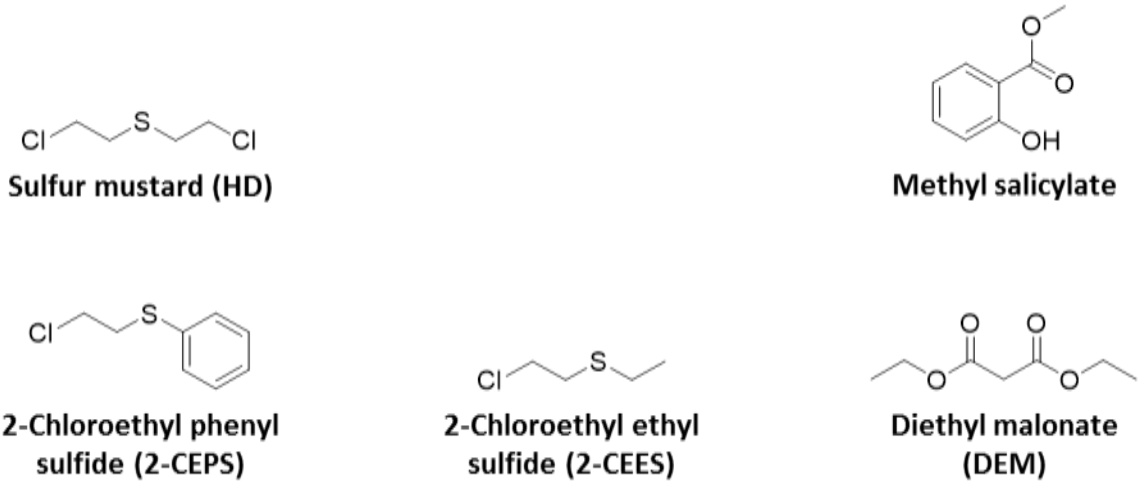

Figure 2. *Schematics for sulfur mustard and four common simulants.*

Table 1*. Physical, chemical, and toxicological properties for sulfur mustard and its four most common simulants.*[78]

molecule	mass (g/mol)	vapor pressure at 298 K (kPa)	density of neat liquid (g/mL)	melting point (K)	boiling point (K)	solubility (mg/L)	Oral LD_{50} (mg/kg)
HD	159	0.015	1.27	218	492	684	20
2-CEES	125	0.45	1.07	157	431	1062	566
2-CEPS	172	0.0025	1.17	257	531	84	
DEM	160	0.036	1.05	200	474	23200	15000
Methyl salicylate	152	0.00053	1.17	223	497	700	887

2-CEES is a less ideal simulant for some other types of studies, especially large-scale environmental fate and equipment exposure tests. Although 2-CEES is less toxic that HD, it still behaves as an alkylating agent and can have detrimental physiological effects on people and animals.[9] Methyl salicylate, also known as wintergreen oil, has much lower toxicity than 2-CEES. In fact, it can be used in low concentrations as a dermal liniment or flavoring in food. DEM is a natural product from grapes and is harmless at low concentrations (ppm levels). Clearly, the relevance of DEM and methyl salicylate to HD arises from similarities in properties rather than molecular structure. All three molecules share similar molecular weight and vapor pressure, which

are important parameters for processes strongly influenced by bulk thermodynamic properties such as evaporation. Research has shown that fabric and dermal penetration behavior are also similar.[10]

Several agent-simulant comparisons have been made. For example, one study compared mass transport for gas-phase HD, 2-CEES, 2-CEPS, DEM, and methyl salicylate.[11] A droplet of simulant or agent was allowed to evaporate in a chamber with controlled airflow, and the concentration of vapor-phase simulant or agent was measured at multiple points downwind of the droplet. Methyl salicylate was found to be the closest mimic of HD in both evaporation rates and downwind concentrations. Thus, mass transport was shown to be a process affected mainly by bulk thermodynamic properties.

Another study measured the adsorption kinetics of HD and 2-CEES on silica nanoparticles impregnated with a variety of additives intended to enhance decomposition.[12] Samples of clean sorbent material were exposed gas-phase agent or simulant at a constant pressure in a sealed chamber. The weight increase of the sorbent material was recorded as a function of time with a balance inside the chamber. Trichloroisocyanuric acid (TCCUA) impregnated silica was found to have the highest adsorption potential for both 2-CEES and HD and NaOH impregnated silica had the lowest adsorption potential for both molecules. Thus, 2-CEES served as an effective mimic for HD. Although the literature provides some insight into the suitability of each simulant for different types of CWA research (e.g. reactivity or environmental fate), none of the HD simulant-agent comparison studies thus far have provided a detailed comparison of desorption energies and the geometries of bound molecules. Our research aims to address this gap in the literature for 2-CEES and methyl salicylate.

1.1.2 Aromatic toxic industrial compounds

The research conducted on methyl salicylate, specifically characterizing the role of the aromatic moiety in surface binding, sparked our interest to better understand the nature of π hydrogen bonds. Therefore, an investigation into the uptake of simple aromatic molecules was conducted. Interactions between aromatic systems and hydroxyl groups may not be highly relevant to the uptake of chemical warfare agents, but they do play a significant role in the surface chemistry of an important class of toxic industrial compounds (TICs). Benzene and simple substituted benzene derivatives such as toluene and chlorobenzene are widely used in research and industry as reagents and solvents. ACS estimates indicate that U.S. chemical plants produce billions of pounds of these compounds annually.[13] Although many efforts have been made to limit release of hazardous chemical waste into the environment, complete containment is not yet a reality. Due to the massive total quantities involved, the consequences of allowing even a small percentage of waste to enter the environment can be serious. Therefore, scientists have significant motivation to learn how these compounds interact with surfaces both to better predict their fate in the environment and to develop more effective sorbents.

1.2 Silica

1.2.1 Structure and properties of silica

A majority of the work described in this thesis characterized gas-surface interactions on silica. Several factors influenced the choice to use this material. Quartz, the most common polymorph of SiO_2 in the environment, is one of the most abundant minerals in the Earth's crust. It is ubiquitous in natural environments (e.g. sand) and is frequently used in man-made devices such as glass and coatings. Insight into the surface chemistry of CWAs and TICs on silica is

necessary to understand the fate of these compounds in the environment. Furthermore, silica-based materials can be used as a sorbent material to trap and break down hazardous compounds.[14] A deeper knowledge about the forces responsible for molecular uptake has potential to drive improvements in future sorbent materials.

The structure of silica has been characterized in great detail. The most typical crystal structure of SiO_2 is based on a simple tetrahedral geometry with a silicon atom surrounded by four oxygen atoms as shown in **Figure 3**. Multiple polymorphs (extended crystalline structures) exist for silica. The amorphous particulate silica used here lacks any long-range order beyond the local tetrahedral arrangement of SiO_2 units. **Figure 4** shows the two different types of adsorption site available on a typical metal oxide surface. Metal atoms behave like Lewis acids, and hydroxyl groups provide Bronsted acid sites. Silica at room temperature only offers Bronsted sites because hydroxyl groups bind strongly to any available Si atoms.

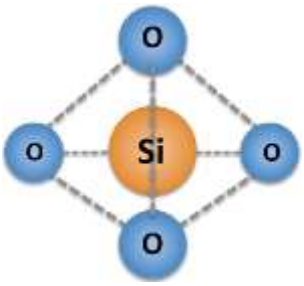

Figure 3. *Tetrahedral building block of SiO_2*

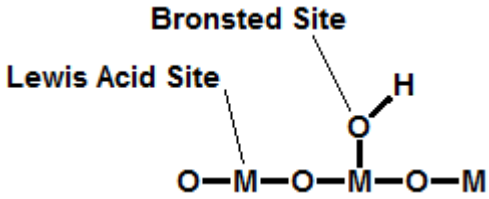

Figure 4. *Bonding sites on a metal oxide surface.*

Silanol groups on the amorphous silica surface can be categorized into three types, shown in **Figure 5**.[15] The referenced study[15] used B3LYP calculations to create realistic models of amorphous silica surfaces at different OH densities. Isolated silanol groups have no nearby neighbors, geminal groups share a single silicon atom, and vicinal groups have neighboring silanol groups on adjacent silicon atoms. Measurements indicate that the highest possible concentration of silanol groups is 4.6 OH/nm^2,[16] which is equivalent to an average distance of 0.76 nm between nearest neighbors. Exposure to high temperatures causes a decrease in the extent of hydroxylation, and the loss of each type of hydroxyl group as a function of temperature has been carefully characterized with a combination of IR and ^{29}Si nuclear magnetic resonance (NMR) spectroscopic measurements, (see **Figure 6**).[16] At 673 K, the concentration of hydrogen-bonded (vicinal) groups is no longer spectroscopically detectable. Above 673 K, the surface is dominated by isolated silanol groups with a small number of germinal groups remaining. The concentration of isolated and geminal groups are both nearly zero at temperatures above 1000 K, well above the typical range for adsorption and diffusion studies, and a highly reactive, fully dehydroxylated surface remains. Silica samples used in this work were heated to 700 K before use. Therefore, we estimate that the concentration of hydroxyl groups on samples tested here was 2 OH/nm^2.

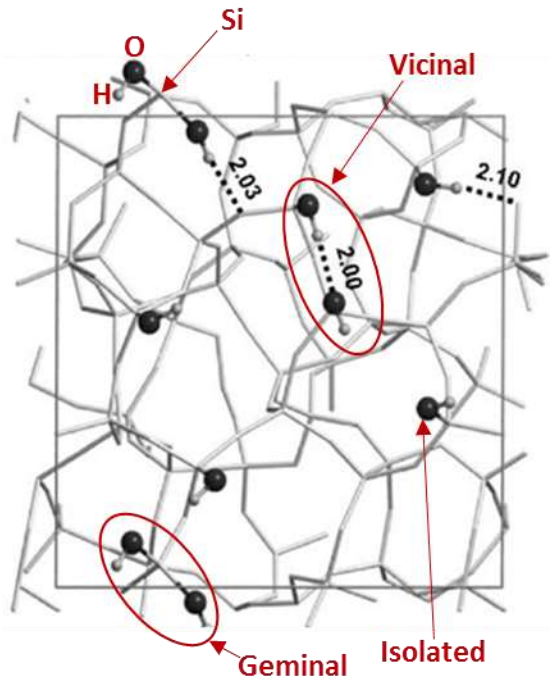

Figure 5. *B3LYP/6-31G(d,p)-optimized amorphous silica surfaces at 4.5 OH/nm^2. H-bond contacts are indicated in Å. Types of silanol group (vicinal, germinal, and isolated) are indicated with arrows. Adapted with permission from Ugliengo et al.*[15]

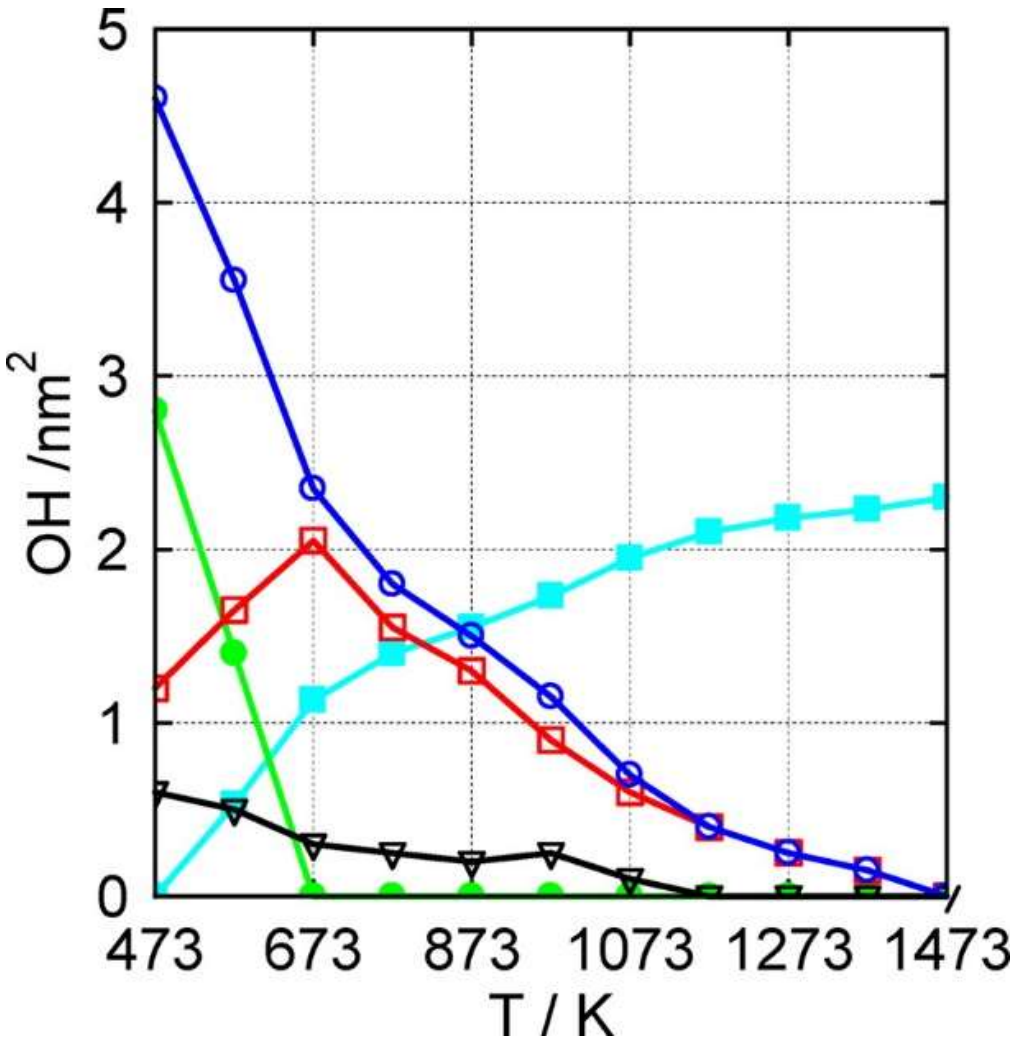

Figure 6. *Distribution of the OH surface groups per square nanometer as a function of the silica sample treatment temperature: (blue open circles) average concentration of total OH/nm2; (cyan solid squares) average concentration of Si–O–Si; (red open squares) average concentration of free OH groups; (green solid circles) average concentration of H-bonded OH groups; (black open downward pointing triangles) average concentration of geminal groups. Reprinted (adapted) with permission from Rimola et al*[16] *Copyright 2013 American Chemical Society.*

1.2.2 Gas adsorption on silica

Uptake on silica is largely driven by the formation of hydrogen bonds between silanol groups and regions of charge asymmetry in adsorbed molecules. Infrared spectra collected during uptake on an initially clean surface clearly demonstrate the formation of hydrogen bonds. For example, the spectra in **Figure 7** were collected as an initially clean sample of silica was exposed

to chloroethane vapors. The region between 3750 and 3500 cm^{-1} is associated with the silanol O-H stretch. Assignments for the other IR bands visible in these spectra will be provided in later chapters. A scan of clean silica was used as a background for all spectra shown in **Figure 7**; therefore, the initial scan of silica at 0 seconds is a flat line. As the surface is exposed to chloroethane, a sharp inverted band centered at 3750 cm^{-1} emerges. This band is assigned to free silanol groups, and its inverted shape is indicative of a depletion of these bands. Concurrently, a broad band at 3570 cm^{-1}, the expected location for the O-H stretch in the SiOH---Cl hydrogen bond, emerges. As is shown in a later chapter, the rate of change in the band assigned to free silanol groups agrees with the rate of change for adsorbate on the surface.

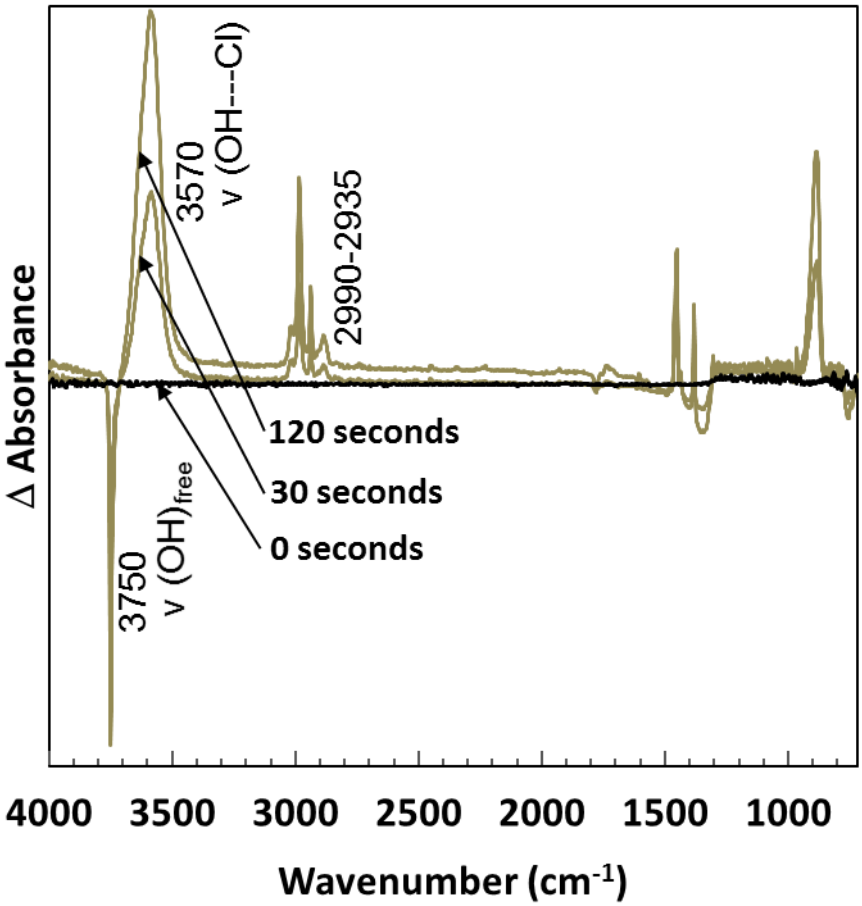

Figure 7. *Spectra collected during uptake of chloroethane on silica. The reference spectrum is clean silica.*

The red shift in the silanol band with adsorption is due to charge transfer between the hydrogen bond donor and acceptor pair. Upon hydrogen-bond formation, electrons from the hydrogen-bond acceptors populate the σ^* antibonding orbital on the silanol O-H bond, thereby weakening the O–H bond and adding significant anharmonicity to the stretching mode.[17,18] The increase in peak intensity is due to the greater oscillator strength of hydrogen-bonded donor stretches.[19] Band broadening is attributed to the inhomogeneity in the configuration of the hydrogen-bonded molecules, which affects the strength and anharmonicity of each bond in different ways. Furthermore, coupling to other modes may have reduced the lifetime of the O–H vibration and increased the homogeneous band broadening.[20–23]

Traditional descriptions of hydrogen bonds often treated them as electrostatic interactions between an electronegative atom and an acidic proton. For example, the IUPAC definition of a hydrogen bond states "It is best considered as an electrostatic interaction…"[24]. However, as discussed above, hydrogen bonds involve partial chemical bonding between a Lewis acid-base pair of the general form X–H---Y that includes a degree of charge transfer from Y to X–H.[25] In fact, results from a computational study suggest that charge transfer interactions may be the dominant factor in the formation of hydrogen bonds, and dipole-dipole interactions may be a secondary consequence that provides additional contributions.[25] Similar investigations into the fundamental nature of hydrogen bonds have led to a proposed revision of the IUPAC definition to explicitly discuss charge transfer between the hydrogen bond donor and acceptor as a significant component of the total hydrogen bond energy.[26] This new insight indicates that molecules bound to surfaces through hydrogen bonding are not simply physisorbed; there are likely chemical interactions (charge transfer) that lead to partial covalency of the molecule-surface bond. In this way, hydrogen bonds may be critical to the activation of molecules for further chemistry.[27,28]

Research to develop a more comprehensive description for the nature of a hydrogen bond is ongoing. An important component of these investigations is to characterize hydrogen bonds that would be considered unconventional by traditional descriptions of hydrogen bonding. For instance, according to the classical views often presented in textbooks, both X and Y in a hydrogen bond of the general form X–H---Y should be electronegative atoms (e.g. O or N).[26] The notion that a hydrogen bond requires electronegative atoms is challenged by numerous examples of hydrogen bonds where the non-hydridic moieties are electron rich (e.g. lone pairs and π electrons) but not electronegative. Benzene and other aromatic molecules have been shown to behave as strong hydrogen-bond acceptors when paired with hydroxyl groups to form O–H---π hydrogen bonds.[29–

[36] The hydrogen bonding character of aromatic-containing compounds arises from an elevated electron density in the ring, which can interact with hydrogen-bond donors through both charge transfer and electrostatic forces.[37] Furthermore, apolar C–H---O interactions are known to play an important role in crystal and protein structures. [25,38] Although weaker than typical O–H---O interactions, they exhibit properties typical of hydrogen bonds.[25]

Another outcome of recent investigations into hydrogen bonding is an improved understanding of the correlation between the vibrational frequency of the O-H bond and the strength of the hydrogen bond. Many attempts have been made to indirectly assess the strength of hydrogen bonds (a value that cannot easily be measured directly in experiments) with spectroscopic measurements of the extent of charge transfer.[39–42] These studies are generally consistent with the so-called "Badger Bauer relationship", which predicts a linear correlation between the shift of the X–H IR band and the strength of the hydrogen bond for similar acceptor-donor pairs.[39,42] This correlation has been verified for several systems. For example, the Morris group recently tested the adsorption of a series of organophosphorus compounds on partially hydroxylated silica and demonstrated that the activation energies of desorption, which vary from 43 to 58 kJ/mol, correlate linearly with the vibrational energy of the silanol O–H group.[40,41]

In contrast, other examples demonstrate that the Badger Bauer relationship cannot be assumed for dissimilar acceptor-donor pairs. For example, a comprehensive computational study[43] of hydrogen-bonding interactions at the ωB97X-D/aug-cc-pVTZ level of theory showed that the OH stretching frequency for the hydrogen-bond donor in H_2O shifted by 88 cm^{-1} when it formed a bond with the chloro group of methyl chloride. Conversely, the OH stretching frequency shifted by more than 200 cm^{-1} when water formed a hydrogen bond with the S moiety of dimethyl sulfide. Despite the large differences in the OH stretching frequency for these two hydrogen bonds,

the calculated energies of the bonds differed by only 2 kcal/mol.[43] The understanding that emerged from this study was that though the spectroscopic signature of a hydrogen bond is highly dependent on the extent of charge transfer, the total strength of the bond is influenced by the interplay between charge transfer and electrostatic interactions. The above example may be interpreted as evidence that the O–H---Cl hydrogen bond consists of a stronger electrostatic and a weaker charge transfer component than the O–H---S hydrogen bond.

An important goal of the work presented in this thesis was to investigate the nature of adsorbate-surface hydrogen bonding on silica with a similar perspective as the above studies for a variety of donor moieties. Specifically, we sought to measure the total strength of several types of hydrogen bonds and deduce the extent of charge transfer from spectroscopic evidence. Further details of experimental goals are presented in the subsequent sections.

Dispersion forces are another important interfacial interaction that have been found to contribute significantly to the total binding energy between surfaces and adsorbates. In fact, linear hydrocarbons were observed to bind to MgO(100) (with more than 70 kJ/mol for decane) mainly through dispersion forces. The researchers reported a linear relationship between hydrocarbon chain lengths and desorption energies, with each additional CH_2 unit contributing an extra 7 kJ/mol. Many of the molecules investigated in this thesis contain CH_2 units and other moieties that can contribute to dispersion forces; therefore, an important component of our analysis was to characterize the role these forces play in uptake on silica.

1.2.3 2-CEES uptake on silica

For molecules like HD and 2-CEES that have functional groups with available lone pairs of electrons, one of the most likely initial binding pathways to silica is through the formation of

hydrogen bonds with surface silanol groups. Uptake of 2-CEES on a mixed TiO_2–SiO_2 composite material was previously characterized with infrared spectroscopy.[14,44–46] The data revealed extensive changes in the SiO-H IR band upon adsorption, indicative of SiOH---Cl and SiOH---S hydrogen-bond formation. However, the nature of these hydrogen bonds in uptake on pure silica has not yet been determined.

Two scenarios could account for the reported spectroscopic evidence of SiOH---Cl and SiOH---S hydrogen bonds. If the density of surface silanol sites is high, each 2-CEES molecule could form multiple hydrogen bonds as both the S and Cl moieties simultaneously hydrogen bond to adjacent silanol groups in a bidentate arrangement. As discussed above, the silica used for all experiments described here has between two and four silanol groups per nm^2. At this density, the average spacing between silanol groups is small enough for a single 2-CEES molecule to potentially span two hydrogen-binding sites. Alternately, if the SiOH---Cl and SiOH---S hydrogen-bond strengths are similar, each adsorbed 2-CEES molecule may occupy a single silanol group with a distribution of the molecules bound by a SiOH---Cl hydrogen bond and the remainder by a SiOH---S hydrogen bond. A computational study of hydrogen bonding interactions showed that the energy of the bond formed between the hydrogen bond donor in H_2O and the chloro group of methyl chloride is only 2 kcal/mol stronger than the bond between water and the S moiety of dimethyl sulfide.[43] It follows that the energies of the SiOH---Cl and SiOH---S hydrogen bonds between 2-CEES and silica are likely also similar. Based on these studies, bi- and mono-dentate adsorption mechanisms both appear plausible. Thus, an important component of our studies on 2-CEES uptake was to determine the ratio between 2-CEES molecules and surface silanol groups. Another research goal was to investigate the role of dispersion forces between silica and the CH_2 linkers in 2-CEES. Previous work provided evidence that dispersion forces can contribute nearly

7 kJ/mol per methylene unit to the desorption energy of linear alkanes on MgO(100).[47] However, this same trend has not yet been observed on amorphous silica.

The analytical techniques employed here allow a detailed investigation of the hydrogen bonds and dispersion interactions responsible for molecular uptake. Various attractive forces (electrostatics, charge transfer, and dispersion) contribute to the total energy of a hydrogen bond.[26] As discussed above, IR spectroscopy is sensitive to the extent of charge transfer between the hydrogen bond donor and acceptor moieties. Temperature programmed desorption (TPD) analysis measures the total strength of all surface-adsorbate interactions, which include dispersion forces and all components of hydrogen bond energy.

We employed both IR and TPD measurements to characterize uptake of a series of straight-chain thioethers and chloroalkanes and thus obtain a detailed understanding of 2-CEES uptake. Schematics and properties for these molecules are provided in **Figure 8** and **Table 2**. The contribution of dispersion forces from the CH_2 groups was evaluated with a series of linear chloroalkanes (chloroethane, 1-chloropropane, 1-chlorobutane, and 1-chloropentane). The nature of the SiOH---Cl hydrogen bond is expected to be similar for these molecules, so any differences in desorption energy can be attributed mainly to dispersion forces. Uptake of diethyl sulfide was compared to uptake of 1-chlorobutane to identify differences between the SiOH---Cl and SiOH---S hydrogen bonds. These molecules have the same number of alkyl linkers, and contributions from dispersion forces are expected to be similar. Any differences in desorption energy can be attributed mainly to the hydrogen bonding interactions. Thus, analysis with TPD and IR provides a comparison not only of hydrogen bond strengths, but also the contributions of multiple types of attractive forces (i.e. electrostatics and charge transfer) to the total hydrogen bond energy.

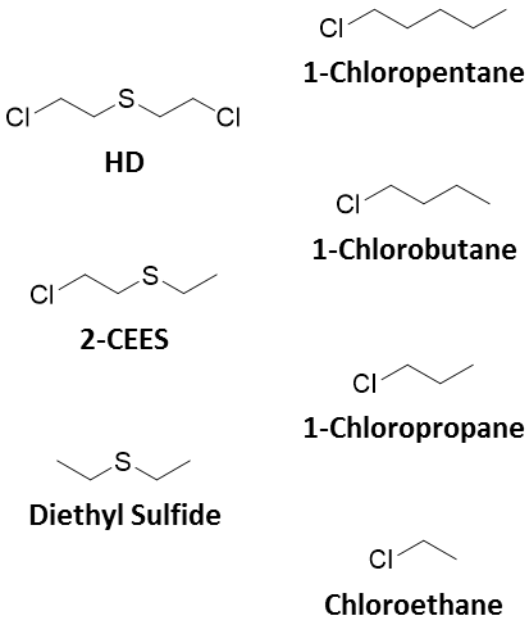

Figure 8. *Schematics for HD, 2-CEES, diethyl sulfide, and selected chloroalkanes*

Table 2. *Chemical and physical properties for HD, 2-CEES, diethyl sulfide, and selected chloroalkanes*[48]

molecule	dipole (D)	volume (cubic angstroms)	polarizability (cm^3)	vapor pressure at 298 K (kPa)	density of neat liquid (g/mL)	mass (g/mol)	boiling point (K)	melting point (K)
HD		125		0.01470	1.27	159	490	288
2-CEES		111		0.5	1.07	125	429	
Diethyl sulfide	1.5	97	10.5	8.03	0.837	90	365	193
Chloroethane	2.1	60	6.6	134.6	0.9	65	285	135
1-Chloropropane	2.1	79		45.9	0.89	79	320	150
1-Chlorobutane	1.9	93		10.7	0.88	93	351	150
1-Chloropentane	2.2	110		4.14	0.88	107	381	174

The data obtained for 1-chlorobutane and diethyl sulfide were compared to 2-CEES results to develop a better understanding of the adsorption mechanism for 2-CEES, specifically if a single adsorbate molecule is able to occupy multiple silanol sites. The intensity of an IR band is directly correlated to the amount of species. Therefore, IR spectra contain information about the percentage of occupied and free silanol groups as well as the amount of adsorbate on the surface. 1-chlorobutane and diethyl sulfide are both expected to adsorb with a 1:1 adsorbate-to-SiOH ratio.

If 2-CEES adsorbs with a 1:2 adsorbate-to-SiOH ratio, the capacity for uptake of adsorbates before the SiOH groups become saturated would be expected to decrease by a factor of two.

A direct comparison of simulant and agent adsorption behavior was conducted with the help of collaborators at ECBC who investigated HD uptake with an instrument very similar in design to the chamber described in the experimental section below. HD has the same molecular structure as 2-CEES except for the addition of a terminal chlorine atom; therefore, HD and 2-CEES are expected to have similar binding mechanisms and desorption energies. The extra heteroatom may increase desorption energy somewhat due to added surface–adsorbate dispersion interactions, but this will be highly dependent on the geometry of the adsorbed molecules and degree of silica hydroxylation. Notwithstanding, the overall desorption energy for HD from silica is expected to be the same as for 2-CEES within the limits of experimental accuracy and precision.

1.2.4 Methyl salicylate uptake on silica

Methyl salicylate uptake on silica was investigated with a series of experiments designed to answer similar questions as were addressed in the analysis of 2-CEES. The activation energy of desorption was measured to directly assess how the combined strengths of the surface-adsorbate interactions for methyl salicylate compare to 2-CEES and HD. Efforts were also made to explore the fundamental nature of the surface-adsorbate interactions responsible for methyl salicylate uptake, specifically which moieties form hydrogen bonds with the surface and the strength of each interaction. The molecular geometry of adsorbed methyl salicylate is not directly relevant to the uptake of live agent due to the dissimilarity in molecular structure; however, it is pertinent to the surface science of toxic aromatic industrial compounds.

Methyl salicylate contains multiple moieties (aromatic ring, carbonyl, ether, and hydroxyl) capable of forming hydrogen bonds with silica. The hydrogen bonding behavior of each of these functional groups has been studied individually,[33,43] but the uptake mechanism of aromatic molecules with multiple strong hydrogen bond acceptors and donors on silica is not well understood. In the case of methyl salicylate, an intramolecular hydrogen bond between the hydroxyl and carbonyl groups is known to exist.[49] This internal hydrogen has been shown to be present in the gas phase, in neat liquid form, and when dissolved in solvents. Researchers have interpreted the persistence of the intramolecular hydrogen bond in these conditions as evidence for a lack of intermolecular hydrogen bonding. Thus, an important goal of our work was to determine the fate of the internal hydrogen bond in methyl salicylate after absorption. To investigate the role of each moiety in methyl salicylate, a series of similar aromatic molecules and acetone were tested. Molecular structures and physical properties for these compounds are provided in **Figure 9** and **Table 3**. TPD measurements and IR analysis of these molecules adsorbed on silica were performed to determine the role played by each functional group and thus infer the uptake mechanism of methyl salicylate.

Table 3. *Physical and chemical properties for the compounds employed in this work.*[48,50]

molecule	dipole (D)	volume (cubic angstroms)	polarizability (cm^3)	vapor pressure at 298 K (kPa)	density of neat liquid (g/mL)	mass (g/mol)	boiling point (K)	melting point (K)
Methyl salicylate	2.2	137		0.00457	1.17	152	495	264
Methyl 2-methyl benzoate		145			1.07	150	480	
Benzaldehyde		103	12.8	0.133	1.04	106	451	216
m-cresol	1.6	109	13.05	0.0147	1.03	108	475	285
Acetone	2.9	65	6.27	30.6	0.78	58	329	179
Benzene	0.0	78	9.95	12.7	0.88	78	353	279

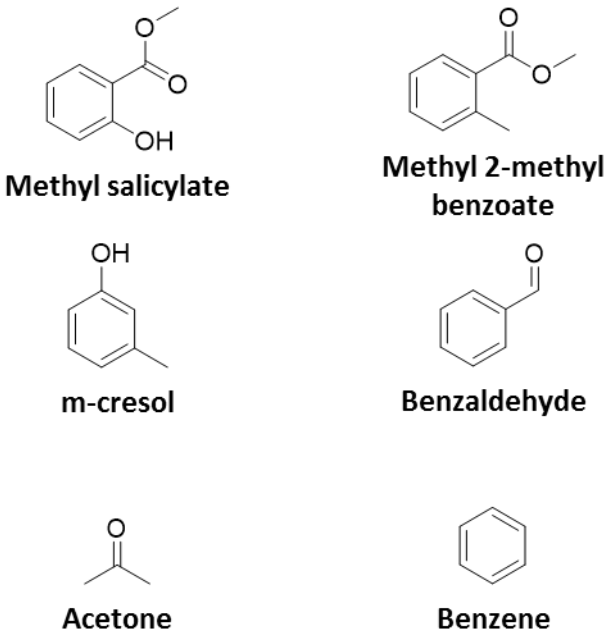

Figure 9*. Schematics for methyl salicylate, acetone, benzene, and functionalized aromatic molecules explored in this project*

1.2.5 Uptake of benzene derivatives on silica

Discussions of hydrogen bonding often exclusively focus on the lone pairs of electronegative atoms such as nitrogen and oxygen as potential hydrogen-bond acceptors.[51] However, numerous examples show that other electron-rich regions in molecules can be viable hydrogen-bond acceptors.[26] Specifically, benzene and other aromatic molecules have been shown to form strong hydrogen bonds with hydroxyl groups, which clearly contrasts with the traditional description of hydrogen bonding as a pure dipole-dipole interaction that forms between two atoms.[29–36] The hydrogen bonding ability of aromatic compounds arises from an elevated electron density in the ring, which can interact with hydrogen-bond donors through both charge transfer and electrostatic forces.[37]

The effects of substituents on the distribution of electrons within aromatic molecules have been studied extensively,[52] and those effects likely play a role in molecule-surface hydrogen

bonding interactions. Aliphatic hydrocarbon substituents such as methyl groups donate electron density through induction. Although halogens are often treated as purely electron withdrawing groups, they have a more nuanced role in how they affect electron density in aromatic molecules.[53] Halogens indeed draw electron density away from the aromatic rings through inductive effects due to their electronegativity. However, the halogen lone pairs simultaneously interact with the aromatic π system and add electron density through resonance effects. The inductive effects for halogens tend to dominate the resonance effects to result in a net electron deficiency in the aromatic ring.

Research has yet to investigate how the interplay among resonance effects, polarity, and electron density affect the nature of the surface-adsorbate π hydrogen bond for substituted aromatic molecules. Contributions to the total binding energy from substituent-surface interactions have also not been measured for this class of molecule. Larger, more polarizable atoms are expected to form stronger induced dipole-dipole interactions, and this is evident in **Table 4** where the vapor pressures of halobenzenes decrease and melting points increase as molecular weights of the substituents increase. As discussed previously, dispersion forces can have a measurable effect on the desorption energy irrespective of hydrogen bond strength. The work described in this thesis represents the first to use infrared spectroscopy and TPD measurements together to explore how these important factors affect uptake of simple substituted benzene derivatives on silica. All common halo-benzenes (astatobenzene is radioactive and not readily available) were tested here along with mono- and di- substituted methylbenzenes. Molecular structures are provided in **Figure 10**, and several chemical properties are listed in **Table 4**.

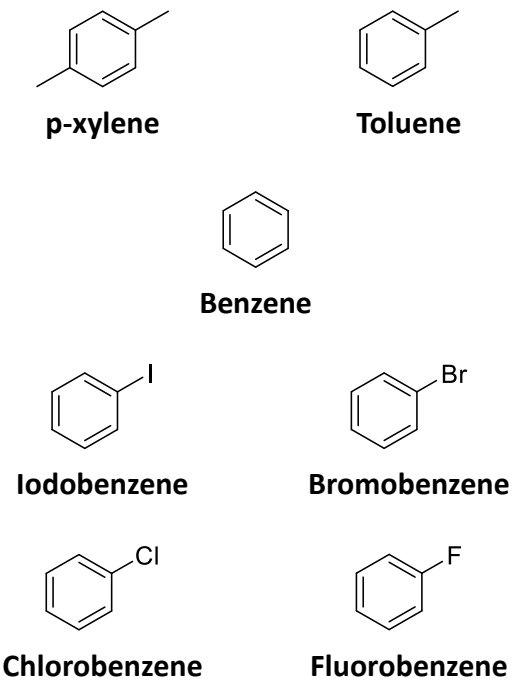

Figure 10. *Schematics for benzene and functionalized aromatic molecules explored in this work*

Table 4. *Physical and chemical properties for benzene and functionalized aromatic molecules explored in this work.*[48]

molecule	dipole (D)	volume (cubic angstroms)	polarizability (cm^3)	vapor pressure at 298 K (kPa)	density of neat liquid (g/mL)	mass (g/mol)	boiling point (K)	melting point (K)
Benzene	0.0	78	9.95	12.7	0.88	78	353	279
Fluorobenzene	1.7	89	10.2	10.7	1.03	96	358	229
Chlorobenzene	1.5	98		1.2	1.11	113	404	228
Bromobenzene	1.6	102		0.55	1.51	157	429	242
Iodobenzene	1.7	108		0.14	1.82	204	461	244
Toluene	0.3	101		0.373	0.87	92	384	178
p-Xylene	0.0	117		1.2	0.861	106	411	286

1.3 UiO-66

1.3.1 Structure and properties of UiO-66

Although uptake studies on SiO_2 provide important data about the fundamental nature of interfacial interactions, the surface chemistry of more complex materials cannot be well understood without experiments designed to directly characterize their behavior during uptake and

desorption. Metal-organic frameworks (MOFs) are a relatively new type of porous, high-surface area materials that have recently attracted much interest for research related to gas adsorption.[54,55] MOFs consist of inorganic nodes joined by organic linkers in a crystalline extended network that typically has sufficient space for molecules to pass through the pores in between the framework components.[55] MOF synthetic pathways often allow for the length of the linker to be changed within a limited range to increase or decrease the pore dimensions. The narrow distribution of pore sizes and highly-tunable nature of MOFs make them well-suited for wide variety of applications including selective adsorption based on molecular size,[56,57] gas storage,[58,59] and catalysis.[60–63] These materials have also attracted much interest in research related to defense against and decontamination of chemical warfare agents (CWAs) for their ability to adsorb large amounts of agent and catalyze decomposition of the adsorbed molecules.[55,64–66] However, the potential usefulness of many MOFs is compromised by their instability in conditions that exist in typical environmental, military, and industrial applications. For example, MOF-5 (a $Zn_4O(CO_2)_6$-based MOF)[67] and HKUST-1 ($Cu_2(OH)_2(CO_2)_4$-based MOF)[68] display excellent performance as sorbent materials for CWAs in a controlled laboratory environment, but decompose when exposed to atmospheric moisture.

Much recent work has investigated UiO-66 and similar Zr-based MOFs that exhibit excellent stability against high temperature, moisture, and mechanical stress.[69–71] Researchers have demonstrated that UiO-66 remains stable after exposure to a variety of solvents (e.g. benzene, HCl, and acetone), boiling water, dry air at 570 K, and 10,000 g/cm^2 of mechanical pressure.[72,73] Decomposition does not occur until over 770 K.[73] A schematic of the structure of UiO-66 is provided in **Figure 11**. The framework consists of octahedral $Zr_6O_4(OH)_4$ nodes connected by 1,4-benzenedicarboxylate (BDC) linkers to form a highly regular crystalline arrangement with 0.6 nm

openings.[72] The robustness of UiO-66 has been attributed to both the strong bonds that join the inorganic and organic components and the 12-fold connectivity between each inorganic node to neighboring nodes.[72] Note that although a perfect sample of UiO-66 would have 12 linkers per node, studies indicate that real UiO-66 samples often have 11 or fewer linkers per node.[54,73,74] These missing-linker defect sites have been shown to increase pore volume and surface area and, therefore, have a direct effect on gas adsorption as will be discussed below.[54] The Langmuir surface area of UiO-66 is reported as 1187 m^2/g,[72] nearly an order of magnitude higher than the surface area of fumed silica (200 m^2/g). When exposed to moisture, UiO-66 contains hydroxyl groups in the inorganic nodes as seen in **Figure 11**. These hydroxyl groups can be reversibly removed and replaced by exposure to high temperature and water respectively. The hydroxylated state is dominant in the environment due to atmospheric humidity and is therefore more relevant to practical applications.

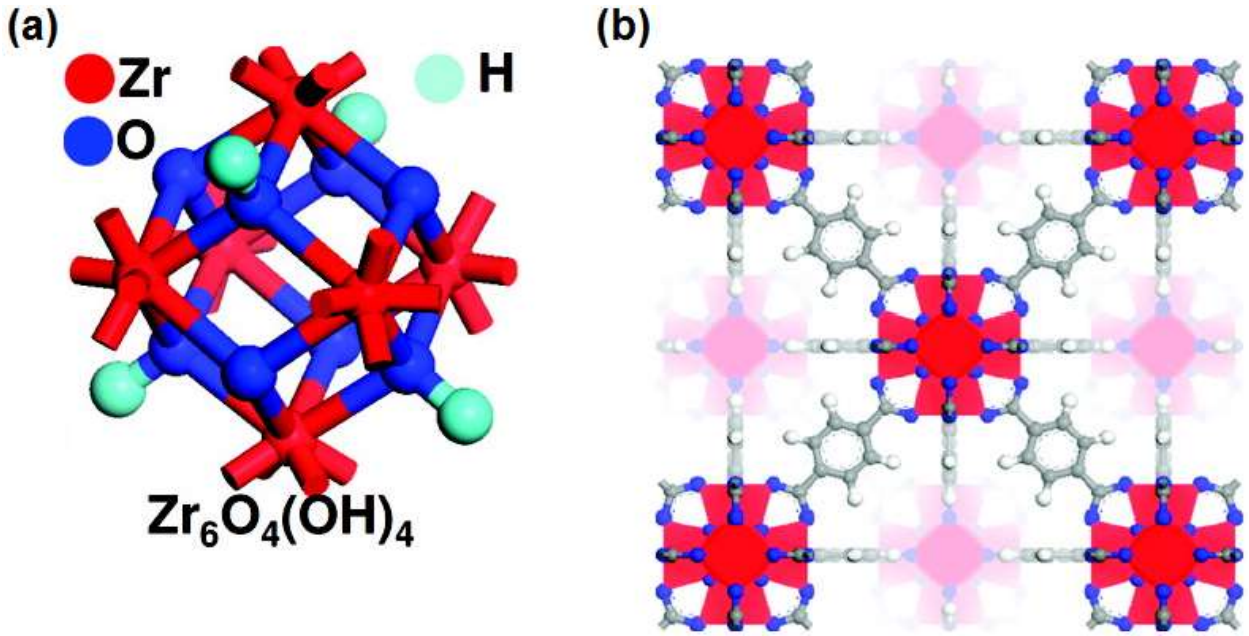

Figure 11. *Schematics of the 3D structure of UiO-66. Panel a on the left depicts the Zr6O4(OH)4 inorganic node. Panel b on the right depicts how the inorganic nodes and organic BDC linkers connect. Zirconium, oxygen, carbon, and hydrogen atoms are red, blue, gray, and white,*

respectively. Reprinted (adapted) with permission from Cavka et al.[72] *Copyright 2016 American Chemical Society.*

1.3.2 Gas adsorption on UiO-66

Previous research on UiO-66 has explored the uptake mechanisms of small gas molecules such as water, carbon dioxide, and methane.[74,75] Both hydroxylated and dehydroxylated forms can bind a large volume of gas, and the Zr metal centers in the nodes have been identified as the likely primary adsorption sites.[74,76] The hydroxylated form exhibits higher performance for uptake of CO_2 due to the formation of electrostatic interactions between the adsorbate's oxygen lone pairs and the hydroxyl group.[74] Similarly, hydrogen bonds may play an important role in uptake of CWAs on hydroxylated UiO-66 even if they are not the primary adsorption sites.

Access to the inorganic nodes inside pores is especially important when MOFs are used for applications related to CWA decomposition because the Zr metal center has been identified as the catalytically active site as well as an important adsorption site.[77] Pore dimensions therefore have a significant effect on uptake. Multiple studies demonstrate the benefits of larger pore sizes in MOFs. For example, uptake of small gas molecules has been shown to increase when the synthesis of UiO-66 is modified to increase the number of missing linker defects, which increases both pore volume and surface area.[54] In another study, a 30-fold improvement in decomposition rate was achieved by using dehydrated NU-1000 instead of UiO-66 for decomposition of the nerve agent simulant dimethyl 4-nitrophenyl phosphate (DMNP).[77] These MOFs are similar, but the framework of NU-1000 consists of eight inorganic nodes instead of twelve and has an extended structure with pores approximately three times larger than UiO-66.[78] The improved performance of NU-1000 was attributed to an increased ability for adsorbate molecules to fit inside of the pores and access the catalytic regions.

1.3.3 2-CEES uptake on UiO-66

As discussed above, previous work demonstrates that UiO-66 is a poor choice for decomposition of larger CWAs such as sarin due to an inability for the CWA molecules to diffuse throughout the entire framework and access all catalytically active Zr binding sites. However, a similar investigation into the uptake of HD has not yet been reported in the literature. The smaller size of HD molecules compared to sarin may allow them to completely permeate UiO-66 and access all available binding sites.

Here, we report the results of preliminary efforts to investigate the uptake mechanism of HD and assess the ability of linear substituted alkanes to diffuse through UiO-66. Diffusion was tested by measuring desorption rates for a series of linear chloroalkanes on dehydroxylated silica to observe if any trends are evident other than the expected increase in dispersion forces with greater alkyl chain length. The uptake mechanism on hydroxylated UiO-66 was evaluated with spectroscopic analysis of the hydrogen bonds to see if SiOH---Cl or SiOH---S interactions dominate. This was accomplished by spectroscopically comparing spectra of adsorbed diethyl sulfide, 1-chlorobutane, and 2-CEES. Also, the desorption energy for 2-CEES on hydroxylated UiO-66 was measured as a benchmark for comparison to future studies on other MOFs. Schematics and properties for all molecules tested in this portion of our work are presented above in **Figure 8** and **Table 2**.

1.4 Organization of thesis

Chapter 2 describes the equipment and methods used in this work along with a discussion of relevant physical principles. The main objective of our experiments was to study the interfacial interactions that affect the uptake of small molecules on silica and UiO-66. IR spectroscopy was

used to determine the molecular geometries of adsorbed species. Mass spectrometry was used to measure binding energies via temperature programmed desorption. A preexisting UHV chamber was modified to analyze well-characterized and contaminant-free particulate samples with both methods simultaneously. The techniques used and developed here are among the first to measure prefactors and activation energies for desorption of small molecules from complex particulate surfaces. Details about data analysis procedures are also described in Chapter 2.

Chapter 3 describes our investigation into the surface chemistry of HD, a vesicant chemical warfare agent, on silica. Several simulant molecules were carefully selected to evaluate the role each moiety in HD plays in uptake on a hydrogen-bonding surface. This work also explored the interplay among the different forces that contribute to overall hydrogen-bond strength (including dipole-dipole attractions and charge transfer between the hydrogen-bond donor-acceptor pair. The content of Chapter 3 is heavily based on a manuscript, co-authored by Amanda R. Wilmsmeyer, Angela C. Edwards, Wesley O. Gordon, Erin M. Durke, Christopher J. Karwacki, Diego Troya, and John R. Morris, that has been published in an ACS journal.[79]

Chapter 4 discusses the surface chemistry of benzene and substituted benzene derivatives on silica. All molecules tested in this chapter formed hydrogen bonds between the delocalized aromatic electrons and silanol groups. The selected substituents had varying degrees of electron donating or withdrawing nature in order to test their effect on the aromatic hydrogen-bond strength. The content of Chapter 4 is heavily based on a manuscript, co-authored by Amanda R. Wilmsmeyer, Angela C. Edwards, Wesley O. Gordon, Erin M. Durke, Christopher J. Karwacki, Diego Troya, and John R. Morris, that has been published in an ACS journal.[80]

Chapter 5 examines the surface chemistry of methyl salicylate, a common simulant for HD. Although HD and methyl salicylate have very different molecular structures, they have similar

physical and chemical properties, which is an important factor in the fate of chemicals in the environment. Our experiments tested several small aromatic molecules to provide a deeper understanding of the geometry of adsorbed methyl salicylate than was known previously and directly compare the activation energies for desorption of methyl salicylate and HD.

Chapter 6 returns to the topic of HD and 2-CEES surface chemistry. The above chapters all focus on silica, a well-characterized surface that has been studied extensively. An important goal and motivation for our research was to develop methods to characterize increasingly more complex materials. The first such surface studied was UiO-66, a high surface area, a catalytically active metal-organic framework with pore sizes of similar dimensions to CWA molecules. Previous work indicated that UiO-66 pores are too small for G-agent (sarin) molecules to pass through. However, HD is a smaller simulant. Our experiments investigated a variety of HD simulants to evaluate the ability of HD to enter UiO-66 pores. Our work is the first to measure desorption energies of HD simulants on both hydroxylated and dehydroxylated UiO-66.

Chapter 2: Instrument Design, Experimental Procedures, and Data Analysis

2.0 Introduction

A significant portion of the scientific investigations described in the following chapters required the development of new experimental and data analysis methods designed to determine the strength of surface-adsorbate interactions on porous and particulate materials. Analysis of the interfacial forces that control uptake on surfaces poses unique challenges. Methods such as BET and calorimetry can assess the surface area of a material and measure thermodynamic properties relevant to adsorption, but fail to provide information about the molecular-scale interactions that are responsible for binding. Investigations of these fundamental forces typically involves temperature programmed desorption (TPD) combined with other surface-sensitive techniques such as spectroscopy under ultra-high vacuum (UHV) conditions.

Our experiments employed TPD analysis in combination with infrared spectroscopy to simultaneously probe the strengths and types of surface interactions present in the systems studied. Our methods measured the activation energy of desorption. In the case of simple molecular adsorption and desorption, this value can be used as an approximation for the adsorption energy and the total strength of all surface-adsorbate interactions. Most TPD work reported in the literature was done on single-crystal samples and assumes a value of 10^{13} s^{-1} for the prefactor (attempt frequency, ν) for desorption based on transition state theory as described later in this chapter (Section 2.7.1) and the assumption that the entropy of molecules in the adsorbed and transition states are the same. In real systems, the entropy of a molecule adsorbed on a surface is generally lower than in the gas phase where the rotational and translational motions are no longer restricted. Therefore, the prefactor is expected to be higher than predicted by transition state theory.

In the case of porous and packed-particulate samples, the possibility of readsorption after a molecule leaves its initial site on the surface can also have an effect on the prefactor.

Methods that provide a way to determine the prefactor from experimental data are therefore desirable when using TPD to measure desorption energies from complex, porous materials. For example, Bruce Kay's group demonstrated how to determine the prefactor with a series of experiments, each with a different initial surface coverage.[47,81] These experiments were among the first to successfully extend TPD beyond single-crystal systems to characterize desorption of simple molecules such as linear alkanes from an amorphous material.

The work in this thesis further extends the method reported by Kay's group to a wider range of adsorbates (aromatics and substituted alkanes) and new materials (particulate silica and the metal-organic framework UiO-66). The experiments reported here are not only among the first to apply traditional UHV methods to the study of high surface area particulate materials, they are the first to apply these methods to characterize the intermolecular forces that drive hydrogen bonding at surfaces. Although the details of experimental procedures were varied for each specific project, the general process and equipment were the same for all projects. A thorough description of our methods for data collection and analysis of data is presented in this chapter along with the results of control experiments to validate our approach.

2.1 Vacuum Chambers and Equipment

The work described in this dissertation aimed to characterize the intermolecular forces responsible for the uptake of gas molecules on high surface area amorphous and crystalline materials. Surface cleanliness is always an important requirement during experiments to measure these interfacial forces. The primary goal in such experiments is to study interactions between

specific sites on the surface and adsorbed molecules. A majority of the work discussed in this thesis characterizes interfacial hydrogen bonding on hydroxylated surfaces. Hydrophilic contaminants such as water can occupy hydroxyl sites and render them unavailable. Contaminants may also promote unwanted side reactions.

$$t_{ML} = \frac{4}{n\bar{v}d^2} \quad \textbf{(2.1)}$$

$$\overline{v} = \sqrt{\frac{8kT}{\pi m}} \quad \textbf{(2.2)}$$

$$t_{ML} = \frac{1.86 \times 10^{-6}}{P} \quad \textbf{(2.3)}$$

t_{ML} = time to form a monolayer on a cm^2 area, in seconds
n = number of molecules per unit volume
$\overline{v}$ = average velocity of molecules
m = molecular weight
d = diameter of a molecule
P = pressure, in torr

The kinetic theory of gasses provides a way to calculate surface contamination rates and thus determine vacuum requirements for sample cleanliness. As shown in **eq 2.1**, the time needed for an initially clean surface to become contaminated is inversely proportional to the number of molecules present, which is in turn directly proportional to the pressure as expressed by the ideal gas law. **Eq 2.1** assumes the case of unit sticking probability. In the case of air (d = 3 × 10^{-8} cm and m = 30 amu), **eq 2.1** can be simplified to **eq 2.3**. A calculation with **eq 2.3** predicts that a surface with dimensions of 1 cm^2 at room temperature exposed to ambient pressure conditions (760 torr) will be fully covered in a few nanoseconds. At a pressure of 1 × 10^{-6} torr, which is considered high vacuum, the surface will become contaminated in approximately one second. The typical base pressure of our chamber, approximately 1 × 10^{-9} torr, extends the expected time to form a monolayer to more than 30 minutes on a 1-cm^2 surface. The surface areas of the sample

employed for the work described here are greater than 100 m^2/g, and would not accumulate a full monolayer of contamination for almost more than 7 months for 10 mg of sample (a typical amount used in this work) according to **eq 2.3**. Contamination during the typical timeframe of TPD experiments (2-5 hours) was virtually zero for the samples and experimental conditions used in this work. This was verified by blank runs where IR, XPS, and TPD measurements were performed following exposure to the ambient vacuum environment for extended period of time. These experiments showed that contamination from background species was below our detection limits (approximately 1% of saturation coverage) in every case.

Prevention of gas phase collisions, another experimental requirement, was also fulfilled by the use of a vacuum chamber. Gas-phase collisions with background gas molecules between the vapor source and the surface or between the surface and the mass spectrometer could obstruct direct detection of molecules that desorb. Because the TPD measurements rely on collision-free line-of-sight detection of molecules that desorb from the surface at a particular temperature, insufficient vacuum would directly interfere with accurate determinations of desorption energies. Collisions with background gasses could also cause reactions that would change the composition of molecules before they reached the surface or ionizer. Lower pressures shorten the mean free path of molecules (λ), which is the average distance between collisions.

$$\lambda = \frac{1}{\sqrt{2} n \pi d^2} \qquad \textbf{(2.4)}$$

The mean free path can be calculated with **eq 2.4**. At ambient pressure, λ is less than one micron. At 1×10^{-9} torr, the mean free path increases to several kilometers, which is more than sufficient to allow molecules to travel within the chamber with a negligibly low probably of encountering another molecule.

Finally, many analytical instruments require vacuum to operate. For example, the ionizing filament in a mass spectrometer would oxidize or vaporize at high pressure. Also, fragments from ionized molecules must not collide with background gasses as they travel through the ion lenses and quadrupole regions in a mass spectrometer. Although the infrared spectrometer does not require vacuum, it benefits from the CO_2- and H_2O-free environment within the chamber. Both molecules have many strong absorbance bands in the IR spectrum that would obscure the spectral signatures of the species under investigation.

The UHV chamber used in this work was initially designed by Joshua Uzarski to study the adsorption isotherms of CWA simulants on silica with RAIRS as the primary analytical tool. Details of the chamber design and construction can be found in his dissertation.[82] Amanda Wilmsmeyer made changes and improvements to the chamber for her studies; however, her approach could not be employed to explore weak hydrogen bonding energies where the rate of desorption is significant near room temperature.[83] Therefore, significant instrument modifications were required for the work presented here.

2.2 Chamber Design

The UHV chamber was designed to allow precise control over surface conditions, IR characterization of a surface before, during, and after exposure to a gas, and MS detection of gas-phase molecules after desorption from the surface. A schematic diagram of the instrument, from the top-down perspective, is provided in **Figure 12**. The main chamber was pumped by a 2000 L/s turbomolecular pump (Pfeiffer, HiMag® 2400) backed by an oil-free scroll pump (Ulvac, DIS-250). The scroll pump could be isolated from the turbo pump with a pneumatic right angle valve (Kurt J. Lesker, SA0100PVQF) mounted on the foreline. Pressure in the main chamber was

monitored by a full-range gauge (Pfeiffer, PKR 251). The mass spectrometer was housed in an adjacent chamber, which had a separate series of pumps and foreline valves. Further details about the mass spectrometer chamber design are provided in a later section of this chapter. A source and detector for IR spectroscopy were mounted outside of the chamber. The IR beam path passed through KBr windows on either side of the chamber. An X-ray photoelectron spectrometer (XPS) was mounted to the chamber, but was not used in the studies described below because elemental analysis was not required. Future work in the group will require this capability, which can be achieved by a simple redesign of the sample holder to allow for proper alignment with the x-ray source.

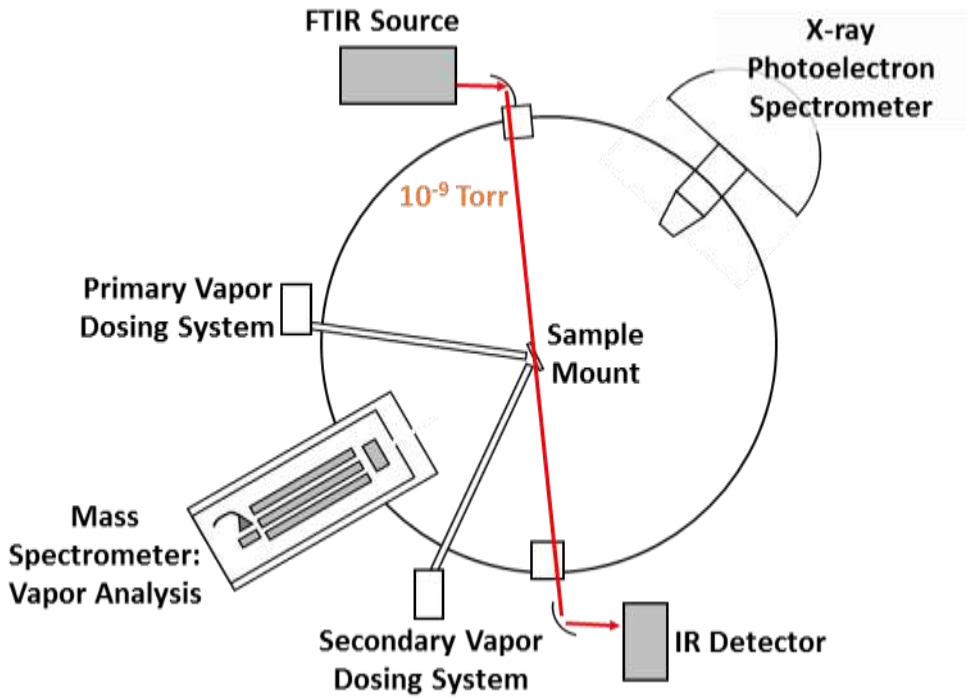

Figure 12. *Schematic of the UHV chamber from top-down perspective*

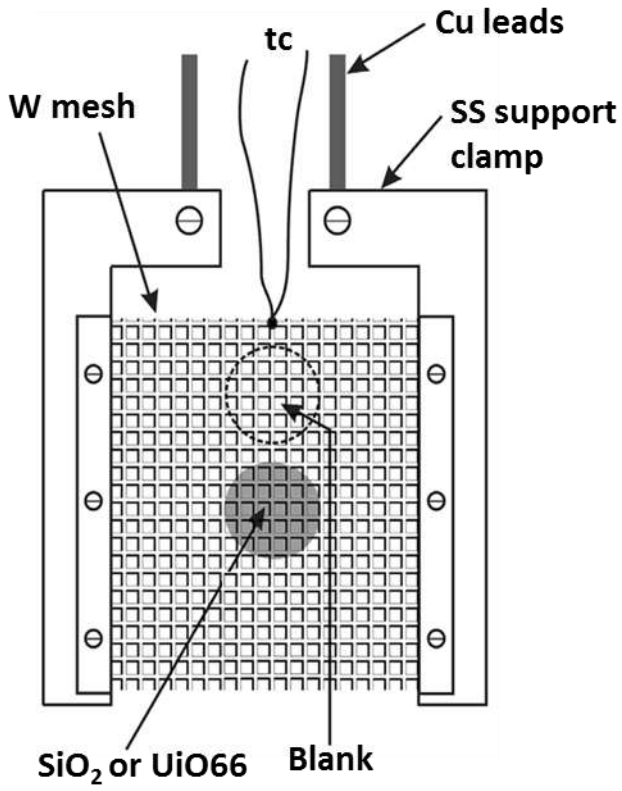

Figure 13. *Schematic of the sample holder*

A custom-built computer interface (interlock) was used to protect the pumps and analytical equipment from power outages, leaks, and pump failures. The interlock system connected the pumps, valves, gauges, and mass spectrometer to a LabVIEW program, which constantly monitored conditions in the chamber. If chamber pressures rose over a setpoint, usually 1×10^{-6} torr, LabVIEW was programmed to shut down the turbo pumps, close the foreline valves, and turn off the mass spectrometer. During experiments, the setpoint was temporarily raised to 1×10^{-4} torr to accommodate for the elevated chamber pressures that could potentially occur as simulant molecules were introduced to the chamber. LabVIEW also gave users direct control over the valves and pumps to shut down the chamber for planned vents and to restart the chamber after a vent for any reason.

2.3 Sample Preparation

Three important design consideration for our research goals were to allow IR light transmission through a high surface area sample and maintain excellent control over sample temperature and position. Previous work demonstrated that a particulate sample pressed into the holes of a conductive mesh support meets these goals.[40,41,79,84] A schematic diagram of the sample holder is provided in **Figure 13**. Approximately 10 mg of sample, either fumed silica nanoparticles (Spectrum) with a surface area of 200 m^2/g or UiO-66 (synthesized by Craig Hill's research group at Emory University[85]) was pressed into a tungsten mesh for 2 minutes at a pressure of 4.4×10^8 N/m^2 in a hydraulic press. The pressing pressure does not measurably affect the experimental results. The 0.0508 mm thick tungsten mesh had holes of 0.20 × 0.20 mm spaced 0.254 mm apart. These dimensions allowed up to 75% and 50% IR transmission through pressed silica and UiO-66 respectively based on comparisons of IR intensity at the detector with the mesh removed from the path of the IR beam versus with the mesh and sample in the IR beam path. The mesh was mounted with clamps to stainless steel brackets, which were in turn clamped to a copper lead and thermocouple (TC) ceramic feedthrough (Kurt J. Lesker, TFT1KY2C302). Chromel and alumel wires were spot welded near the upper edge of the mesh and to the TC leads on the feedthrough.

Outside of the chamber, the copper and TC leads were connected to a custom power supply and temperature controller. The copper leads were silver soldered to 0.09" diameter insulated copper wire extensions attached to a 50 A power supply, which controlled the surface temperature with a proportional-integral-derivative device (PID). The TC leads were spot welded to insulated chromel and alumel wires attached to the same PID. The PID used a control loop feedback system to continuously minimize the difference between the measured temperature and the setpoint temperature by adjusting current through the mesh. A custom nipple attached the feedthrough to

an X-Y-Z-rotation manipulator stage. The nipple and manipulator stage served as a liquid nitrogen reservoir to cool the mesh and sample. The reservoir was purged with dry air for several hours prior to cooling to keep moisture trapped in the ceramic seals from freezing and causing cracks.

Silica samples were heated to 700 K at a rate of 0.2 K/sec and left at this temperature for at least one hour prior to the first run on a new sample to dehydroxylate the silica. Published simulated spectra for amorphous silica surfaces showed the effect of extent of hydroxylation on the OH absorption bands.[15] At 7.2 OH/nm^2, the narrow bands for free and nearly free OH groups were visible around 3745 cm^{-1} and the broad band for hydrogen-bonded OH groups extended from 3700 cm^{-1} to below 3500 cm^{-1}. The band for hydrogen-bonded OH groups rapidly decreased in intensity for simulated spectra of 5.4 and 4.5 OH/nm^2 and left a spectrum increasingly dominated by a narrow band near 3745 cm^{-1}. Our spectra of partially dehydroxylated silica, for example the red (bottom) spectrum in **Figure 14,** looked remarkably similar to the published simulated spectrum for 2.4 OH/nm^2. Based on this and other work,[86–90] we estimated that our high-temperature pretreatment generated a surface with between 2 and 4 OH/nm^2. The same references, including experimental work that reported a plot of the type of OH groups on silica as a function of surface temperature,[90] suggested that the majority of remaining silanol groups after the 700 K pretreatment were likely isolated (evidenced by the sharp band at 3750 cm^{-1}). The remainder, which contributed to the shoulder below 3720 cm^{-1}, were geminal and vicinal groups.

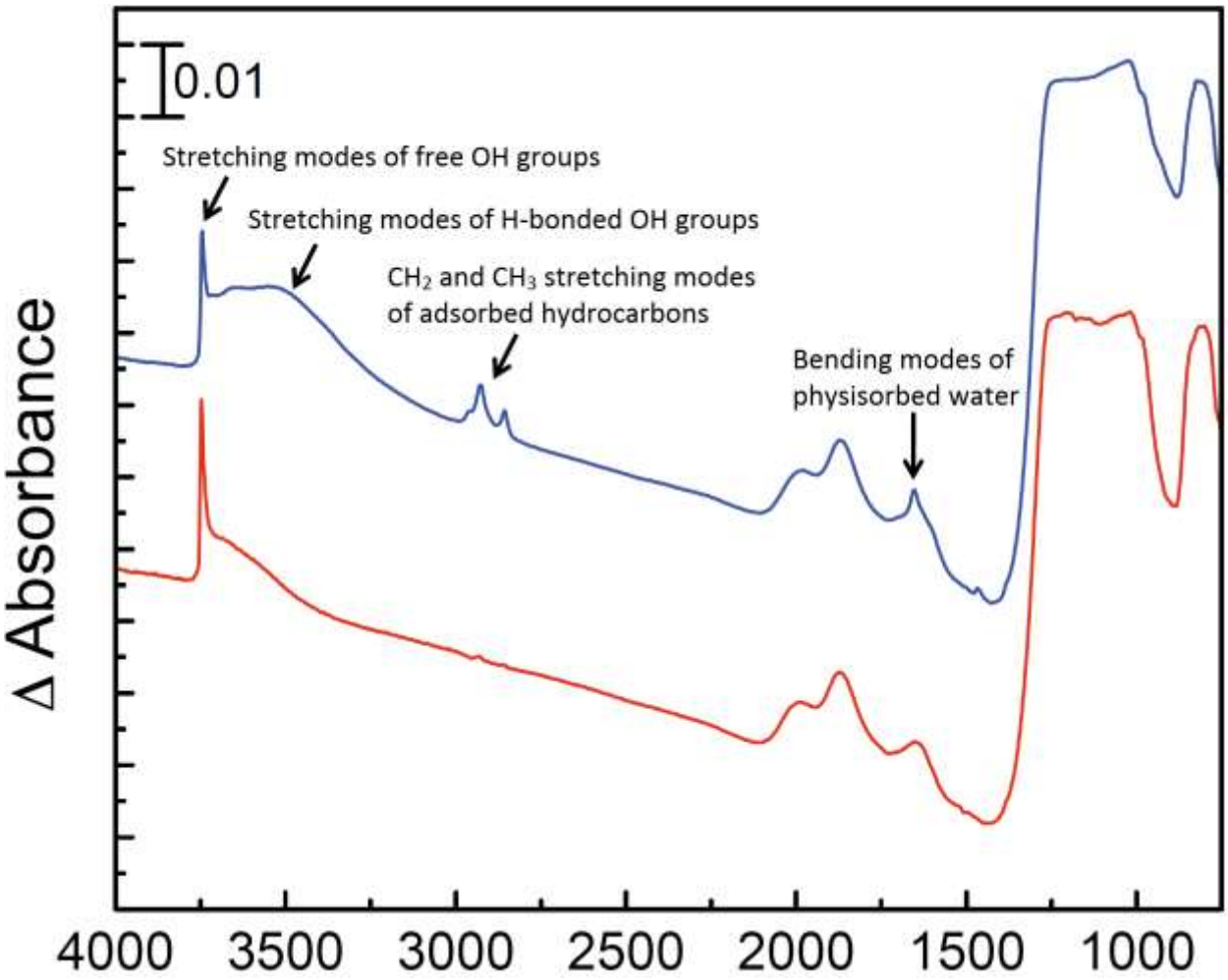

Figure 14. *IR spectra of silica before (blue, top) and after (red, bottom) the initial pretreatment. The bands at 1800 and 2000 cm^{-1} are associated with combinations of vibrations in the SiO_2 network. The bands below 1500 cm^{-1} are associated with Si–O–Si stretching vibrations.*

Another important purpose of the high-temperature pretreatment procedure was to drive off adsorbed water and hydrocarbons to leave a clean surface for adsorption studies. **Figure 14** shows a silica sample before and after the initial pretreatment. Adsorbed water and hydrocarbons have distinctive IR absorption bands, which are evident before pretreatment and absent afterwards. In a similar manner, IR spectra were recorded and analyzed to check if the sample was contaminated or degraded prior to each experiment. If contamination was observed, the pretreatment step was repeated to clean the sample. Degradation of the silica from prolonged

exposure to vacuum, repeated exposure to chemicals, and thermal cycles did not occur to a significant extent. **Figure 15** shows two spectra of the same silica sample recorded one year apart (February 2013 and February 2014) after exposure to a variety of sulfur mustard simulants. Other than a slight reduction in the percentage of vicinal and geminal silanol groups, likely due to dihydroxylation from repeated exposure to high temperature, the spectra are nearly identical.

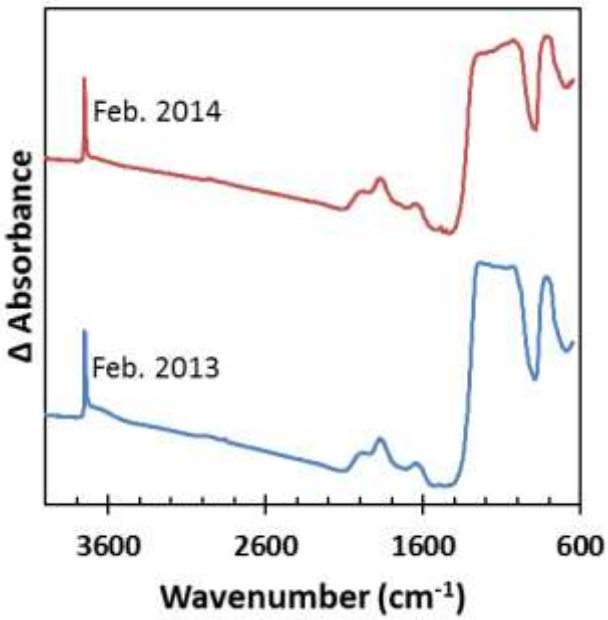

Figure 15. *IR spectra of the same silica sample taken approximately 1 year apart. Each scan was recorded in the morning immediately before beginning experiments for the day.*

UiO-66 was also heated at a rate of 0.2 K/sec prior to the first run on a new sample, but only to 600 K. Higher temperatures would risk permanently damaging the molecular framework. Previous work has shown that the crystal structure of UiO-66 begins to degrade at 650 K.[73] Heating UiO-66 served two purposes as depicted in **Figure 16**. Initially, the sample contained both trapped solvent, likely DMF from synthesis (broad band below 3600 cm^{-1}), and free hydroxyl groups (3670 cm^{-1}). The trapped solvent was removed during a 0.2 K/s temperature ramp to 575 K, but the

sample remained nearly fully hydroxylated immediately after the ramp ended. Then, as the sample's temperature was maintained at 575 K for an extended period, usually overnight, the hydroxyl groups were gradually driven off until the sample was fully dehydroxylated. Exposure to water and a variety of common organic solvents had minimal permanent effects on the UiO-66, within the sensitivity of our IR spectrometer. Both hydroxylated and dehydroxylated UiO-66 samples were tested in this work. Further discussion about the properties of these two states of UiO-66 is presented in a later chapter.

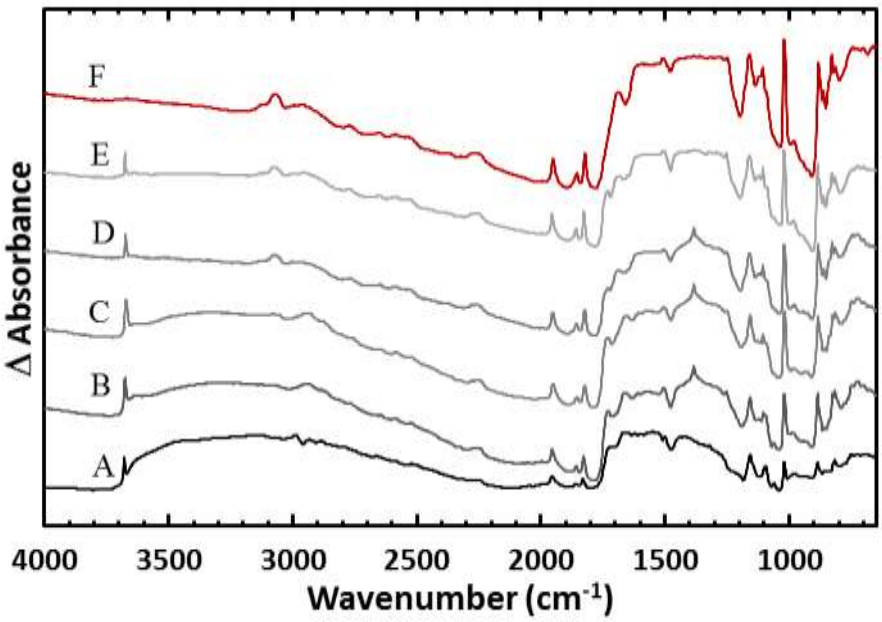

Figure 16. *The effects of vacuum and heat on UiO-66. A) Ambient conditions. B) Immediately after exposure to vacuum. C) After 0.2 K/s temperature ramp to 440 K. D) After 0.2 K/s temperature ramp to 575 K. E) After exposure to several solvents including water and acetone. F) After overnight heating at 575 K.*

2.4 Gas dosing

Gas-phase simulant molecules were introduced to the surface through a custom doser and manifold, which allowed a controllable flux of gas at the surface while maintaining high vacuum in the chamber. A schematic of the doser is provided in **Figure 17**. The core design of the doser

was a custom gas feedthrough (Lesker) with ¼" male VCR connections on both ends. On the vacuum side, a machined hollow stainless steel cylinder and cover plate contained a glass capillary array (GCA, Photonis with 10-micron pores and 12-micron center-to-center spacing between pores). The cylinder was attached to the feedthrough with a VCR connection. A ¼" stainless steel tube, which increased the directionality of the doser, was press fit into a hole in the center of the cover plate. The entire doser assembly was mounted on a z translation stage (McAllister, BLT27C-4), which allowed the end of the stainless steel tube to be positioned within 1 mm of the surface during dosing.

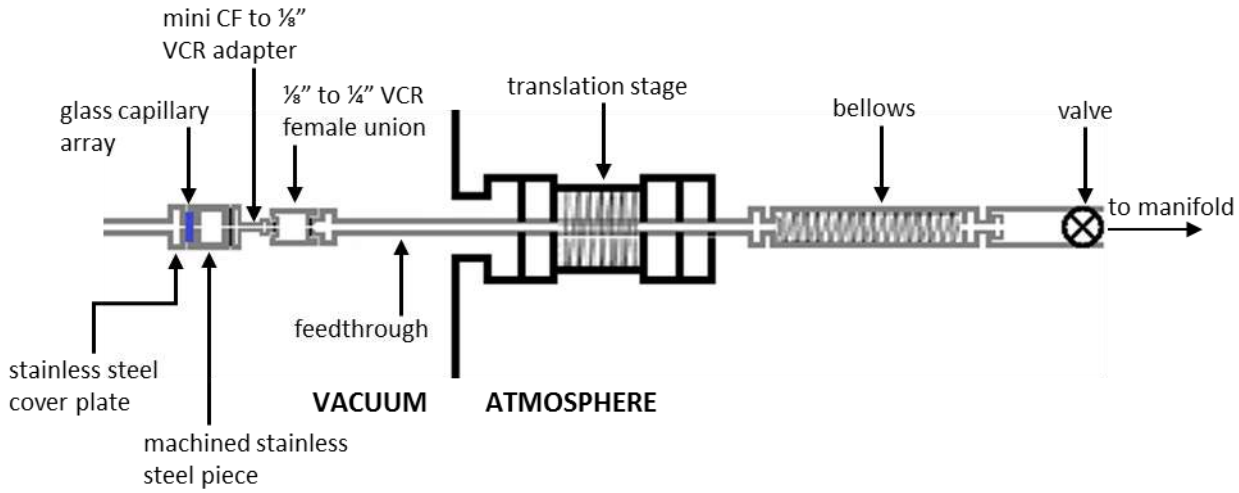

Figure 17. *Schematic of the primary gas doser*

The atmosphere side of the doser was connected to a custom gas manifold (**Figure 18**) constructed of stainless steel tubing and bellows sealed valves (Dibert Valve, SS-4BG-V51). The manifold was maintained under high vacuum (~1×10^{-5} torr) when not in use to keep the tubing clean. A sorption pump (MDC Vacuum, SP-150) was used for initial pumping, followed by a 60 L/s ion pump (Duniway Stockroom, rebuilt Varian 911-5034) to attain high vacuum.

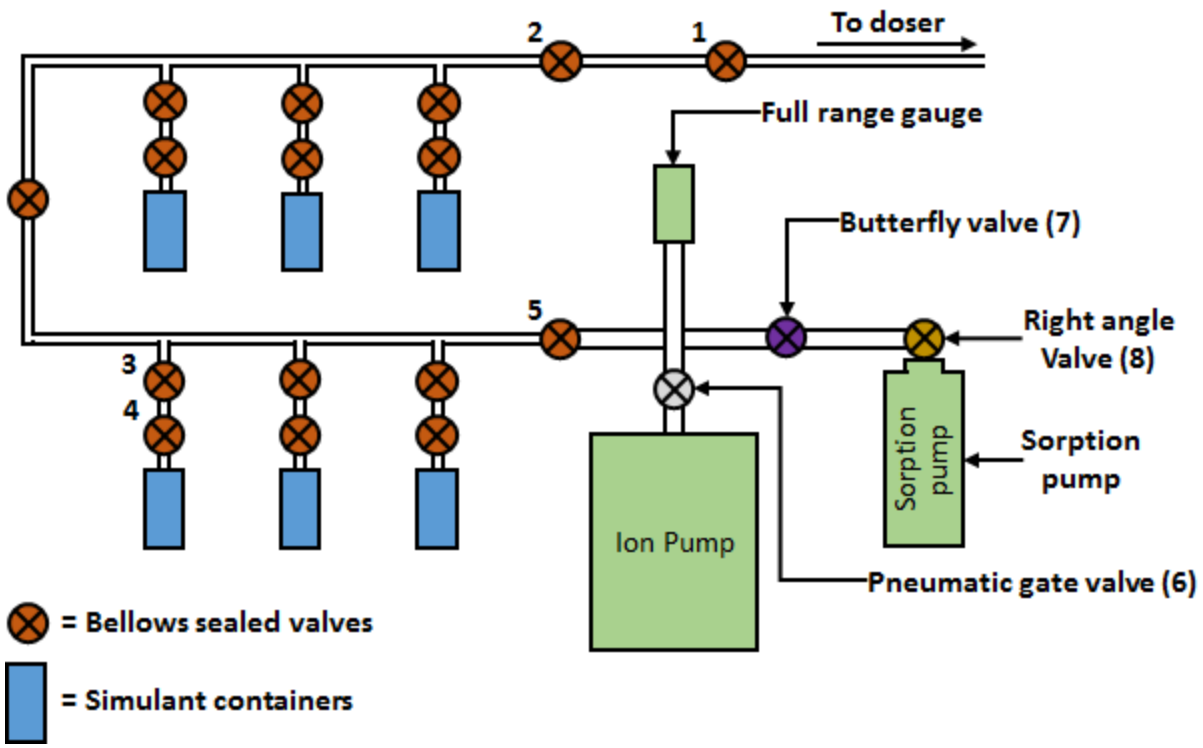

Figure 18. *Schematic of the primary gas manifold*

Neat liquid of simulants was contained in stainless steel dosing cylinders with male VCR connections. The cylinders were filled in a fume hood and capped with a bellows-sealed valve prior to transport to the chamber to protect lab personnel from exposure to potentially dangerous chemical vapors. After mounting to the manifold, the liquid was purified with a series of freeze-pump-thaw cycles. For all simulants studied here, the vapor pressure of the neat liquid at room temperature was sufficient to deliver an appropriate flux of molecules to the surface. Before starting experiments with a new simulant, the manifold was heated with heater tape powered by variable power supplies for several hours to avoid contamination from the previous simulant.

A typical dosing procedure was as follows. Initially, valves 1, 3, 7, and 8 were closed. All other valves were open. The volume to the right of valve 1 in the schematic was open to the main chamber and was under UHV. The volume between valve 1 and the ion pump was unobstructed

by valves and was also under HV. The first step was to open valve one while the entire manifold was still at HV. Then, valves 2 and 5 were closed to isolate the ion pump and the main chamber from the section of the manifold that held the simulant containers. Next, valve 3 was opened to fill the volume between valves 2 and 5 with vapors of the simulant. At this point, valve 2 was the only obstruction between simulant at its vapor pressure and the main chamber. Valve 2 was used to control the flux of simulant molecules that entered the chamber during dosing. Extreme caution was taken not to open the valve too quickly and flood the chamber with an excessive flux of simulant, which would negatively affect the main chamber turbo pump. The interlock system was unable to shut down the pumps quickly enough to protect them from a mistake during dosing. Typical main chamber pressures during dosing were in the 1-5 $\times 10^{-6}$ torr range. Any sustained pressure over 1×10^{-4} torr would have put the main turbo pump at risk of failure due to the large gas load.

When dosing was complete, valves 2, 1, and 3 were closed in that order. The entire manifold was evacuated to HV prior to the next experiment. First, the sorption pump was cooled with LN_2. Then, valve 6 was closed to isolate the ion pump. Valves 2, 5, and 8 were opened in that order. There was a risk that the volume between valves 5 and 8 could become contaminated with molecules from the sorption pump if valve 8 was opened before valve 5. When the pressure in the manifold dropped below 5×10^{-3} torr and stabilized, valve 8 was closed, and valve 6 was opened immediately afterwards.

Valve 7 was present to facilitate sorption pump service. Sorption pumps operate by trapping molecules on a high surface area sorbent material inside the pump. Many of the simulants used in this work were toxic. When the sorption pump was removed for any reason, it had to remain sealed until it was placed in a fume hood. Therefore, valve 8 was removed along with the sorption

pump. In this case, valve 7 could be closed to keep atmospheric contaminants, especially water, out of the manifold. The other pumps on the chamber did not need a dedicated valve for removal. Ion pumps break down simulant molecules and embed the ionized fragments in a cathode. These fragments do not pose a significant safety hazard. Exhaust from the turbo pumps was continually directed into tubing that led to the fume hood ventilation system.

A secondary dosing system and manifold was designed during this work to investigate cases in which a surface is exposed to two different species during the same experiment. The secondary doser was identical in design and operation to the primary doser (**Figure 17**), except a custom stainless steel pinhole aperture (**Figure 19**) was used in place of the GCA. The aperture controlled flux and provided a degree of directionality to the gas flow, at a reduced cost compared to the GCA.

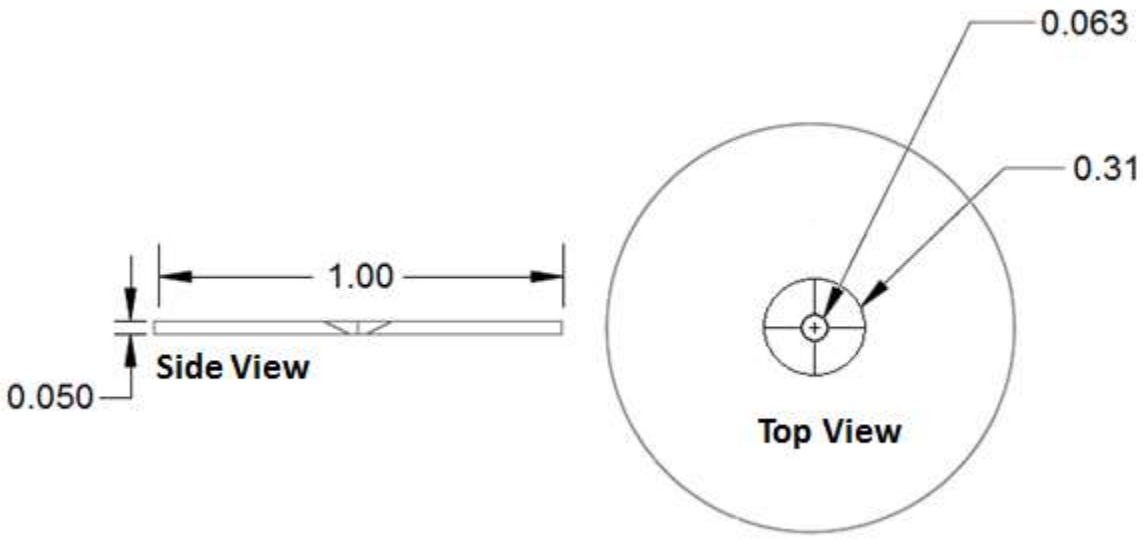

Figure 19. *CAD schematic of the pinhole aperture inside the secondary gas doser*

The secondary manifold was a simplified version of the primary manifold with improvements designed to increase ease-of-use and reduce the time needed to evacuate the manifold. A schematic is provided in **Figure 20**. Pressures during dosing were controlled with a

leak valve instead of a bellows sealed valve, which significantly improved control over the pressure and reduced the likelihood of accidentally damaging the main chamber turbo pump. A 1.5" inner diameter bellows was used instead of ¼ tubing between valve 5 and the turbo pump, and the volume exposed to simulant at its full vapor pressure during dosing (between valves 5 and 2) was small. Although the volume inside the bellows somewhat increased the initial pump down time (i.e. after venting the entire manifold), the increased throughput and small volume filled with simulant vapor significantly decreased pump down times after dosing compared to the original manifold. Finally, the combination of a turbo pump (Pfeiffer HiPace 80) and scroll pump (Edwards XDS10) was better able to handle the gas load (~5×10^{-3} torr) when transitioning from the sorption pump after dosing

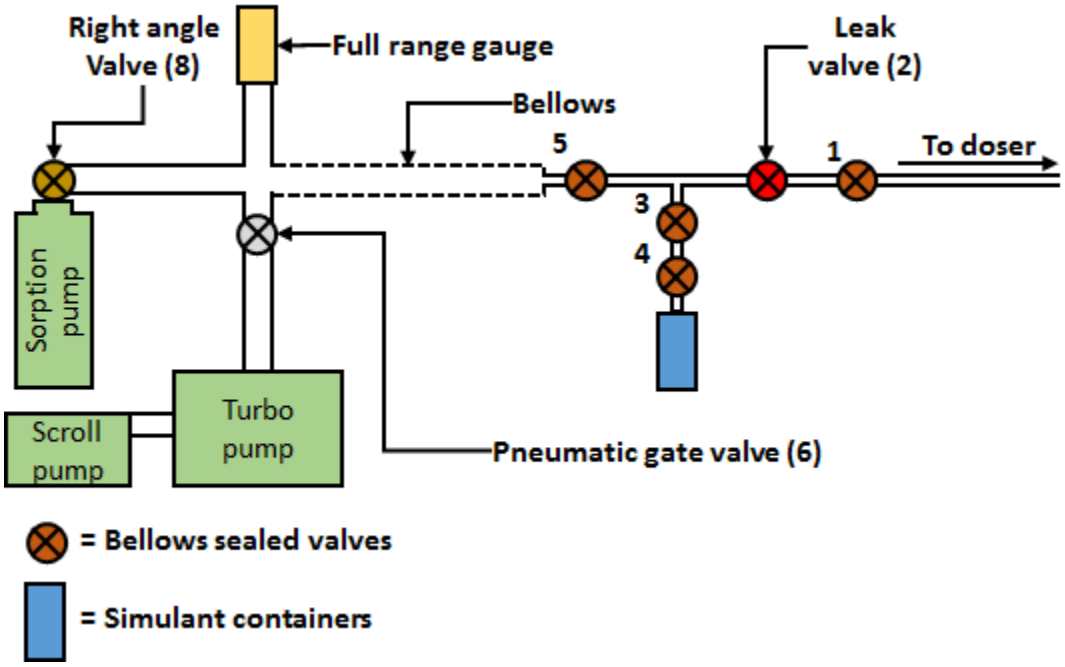

Figure 20. *Schematic of the secondary gas manifold*

2.5 Infrared Spectroscopy

We characterized the materials before, during, and after dosing with transmission IR. IR spectroscopy provides information about the vibrational energies of chemical bonds. Functional groups have absorption bands at characteristic frequencies, which serve as fingerprints to identify molecules on the surface and characterize changes in the surface caused by adsorption. In many cases, the concentration of molecules on the surface is proportional to infrared absorbance. This proportionality has been verified in our work by comparison to the integrated mass spectrometer signal from TPD measurements as discussed in **Section 2.7.1** below. The quantity of simulant on the surface can therefore be inferred from spectra. Thus, the data provided by IR spectroscopy is both selective and quantitative.

All UHV spectroscopic data in this work was recorded with a Nicolet Nexus 670 spectrometer purged with dry air. The layout of all relevant components is shown in **Figure 21**. A SiC mid-IR source, aperture wheel, and Michelson interferometer with a KBr beam splitter resided within the spectrometer. An adjacent dry-air-purged optics box contained a flat mirror (Bruker Optics IM190-GH) and a parabolic mirror (Bruker Optics IM137-GH; f=250mm) to focus the IR beam on the silica or UiO-66 sample near the center of the chamber. Wedged KBr viewports on either side of the chamber allowed the beam to pass through. After exiting the chamber, the IR beam entered a second dry-air-purged box and was collimated by a parabolic mirror, reflected off a flat mirror, and focused by a final parabolic mirror into a LN_2-cooled mercury-cadmium-telluride (MCT-A) detector with 750-4000 cm^{-1} range. The majority of IR scans reported in this thesis used the following spectrometer settings: 1.89 cm/s scanner velocity, 32 mm aperture, and 4 cm^{-1} resolution. The number of scans per spectrum was varied among 16, 64, and 128 scans as appropriate to balance between time resolution and signal-to-noise ratio.

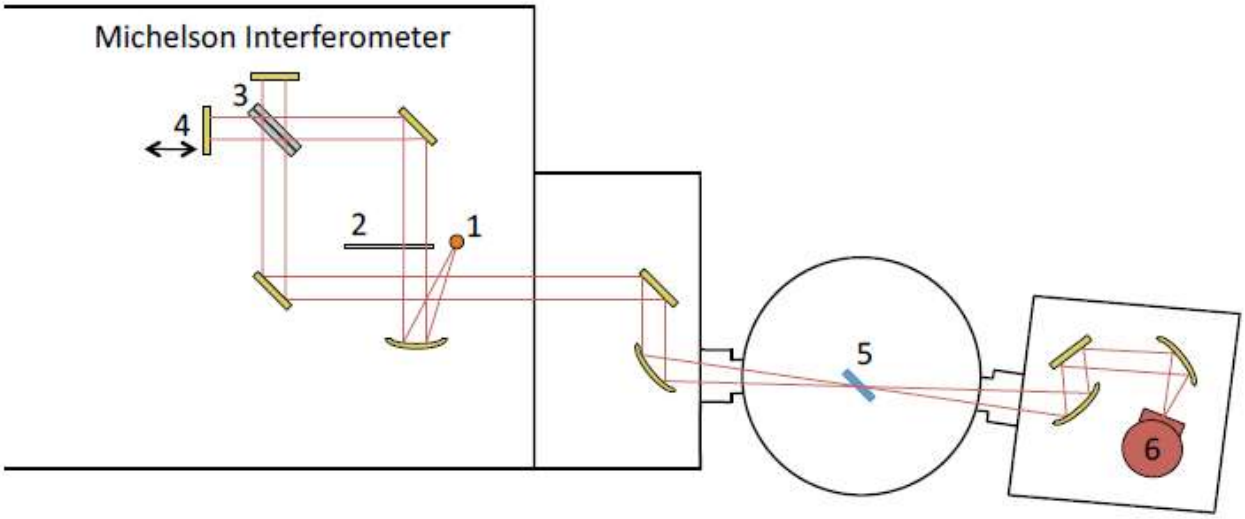

Figure 21. *Schematic of the IR optics path. The components are labelled in the following manner: 1) SiC IR source, 2) aperture wheel, 3) KBr beamsplitter, 4) moving mirror, 5) sample surface, 6) MCT detector.*

2.6 Mass Spectrometry

A quadrupole mass spectrometer (Extrel, MAX1000880APP3/4P8) with a 2-1000 amu range and 1 amu resolution was used to detect gas-phase molecules after they desorbed from the surface. Gas phase molecules were broken up into fragments in the axial ionizer. The fragments were separated by their mass-to-charge ratio by the 19 mm quadrupole diameter rods and detected with a channel electron multiplier. The mass spectrometer was positioned in direct line-of-sight of the surface behind two apertures and two stages of differential pumping. The mass spectrometer signal was proportional to the number of molecules in the area of the ionizer. Molecules that were not ionized on the first pass through the ionizer were likely to exit the chamber through a pump (the base pressure of the MS during experimental measurements was below 8×10^{-8} torr). Therefore, the mass spectrometer behaved as a number density detector, and the signal was inversely proportional to the rate at which molecules entered the ionizer (which, in turn, was related to the rate of desorption from the surface).

Ion optics must be properly tuned for a mass spectrometer to perform optimally. Improperly tuned ion optics cause mass fragments to have flight paths that do not allow them to reach the detector. **Figure 22** shows a schematic of the ion optics configuration used in this work. Ions were formed as molecules interacted with high-energy electrons (10-1000 eV). Next, a series of lenses guided the ions into the quadrupole mass filter. The extractor lens, set at a small negative voltage, pulled ions from the ion region. The ions were then focused by three Einzel lenses. The first and third slowed ions with a gentle negative voltage before they reached the quadrupole rods. The second Einzel lens used a stronger negative voltage to accelerate the ions. Entrance and Exit lenses placed immediately before and after the quadrupole rods focused and drew ions through the rods. Tune parameters were varied slightly throughout the studies presented in this thesis to accommodate a variety of factors including gradual deterioration of the electron multiplier and replacement of several components inside the mass spectrometer. **Table 5** shows the parameters used for one portion of our work, and **Figure 23** shows a mass spectrum between 10 and 60 amu recorded with these tune parameters. The expected background gasses for a UHV chamber are present (water at 18 amu, nitrogen at 28 amu, and carbon dioxide at 44 amu).

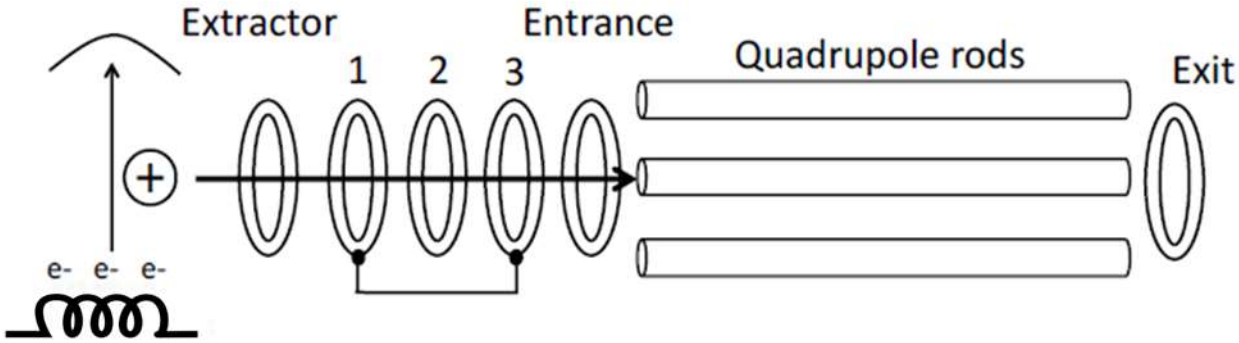

Figure 22. *Schematic of the mass spectrometer ion optics*

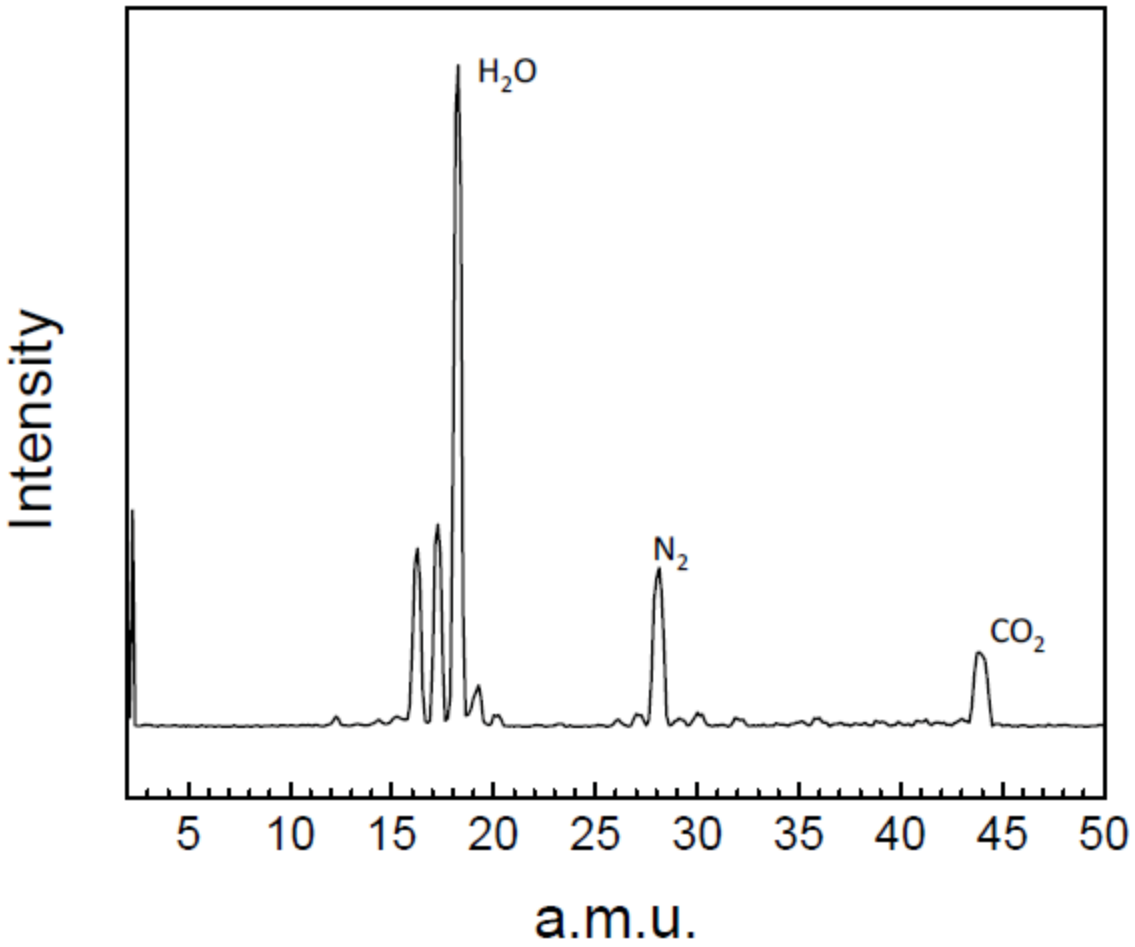

Figure 23. *Sample mass spectrum of background gasses present in chamber under UHV conditions*

Table 5. *Sample tune file settings used for a portion of work presented in this thesis*

Optics	Setting
Electron Energy	-70 V
Electron Emission	2.00 mA
Ion Region	10 V
Extractor Lens	-7 V
Lens 1 & 3	-5 V
Lens 2	-140 V
Quadrupole Entrance Lens Min/Max	-16 V / -13 V
Quadrupole Exit Lens	-260 V
Dynode Voltage	5000 V
Multiplier Voltage	1900 V

The pressure in the main chamber during dosing and heating stages of experiments often rose over the maximum operational pressure range for the mass spectrometer. Also, the mass spectrometer was intended to detect only molecules that had just desorbed from the surface of the sample. These challenges were addressed by housing the mass spectrometer in a doubly differential pumped chamber (see **Figure 24**). With this design, the main chamber pressure could rise to over 1×10^{-5} torr for brief periods while the mass spectrometer chamber remained near or even below 1×10^{-9} torr. The principle of differential pumping involves pressure reduction in stages with the use of small apertures. The first stage was a custom cross attached to a 200 L/S turbo pump (Edwards) backed by a scroll pump (Ulvac, DIS 250). The second stage, which housed the mass spectrometer, had a 400 L/s turbo pump (Pfeiffer) backed by the same scroll pump as the first stage turbo pump. A full range gauge (Pfeiffer) monitored pressure in the mass spectrometer chamber, and LabVIEW was programmed to disable the mass spectrometer any time the gauge read more than 1×10^{-7} torr.

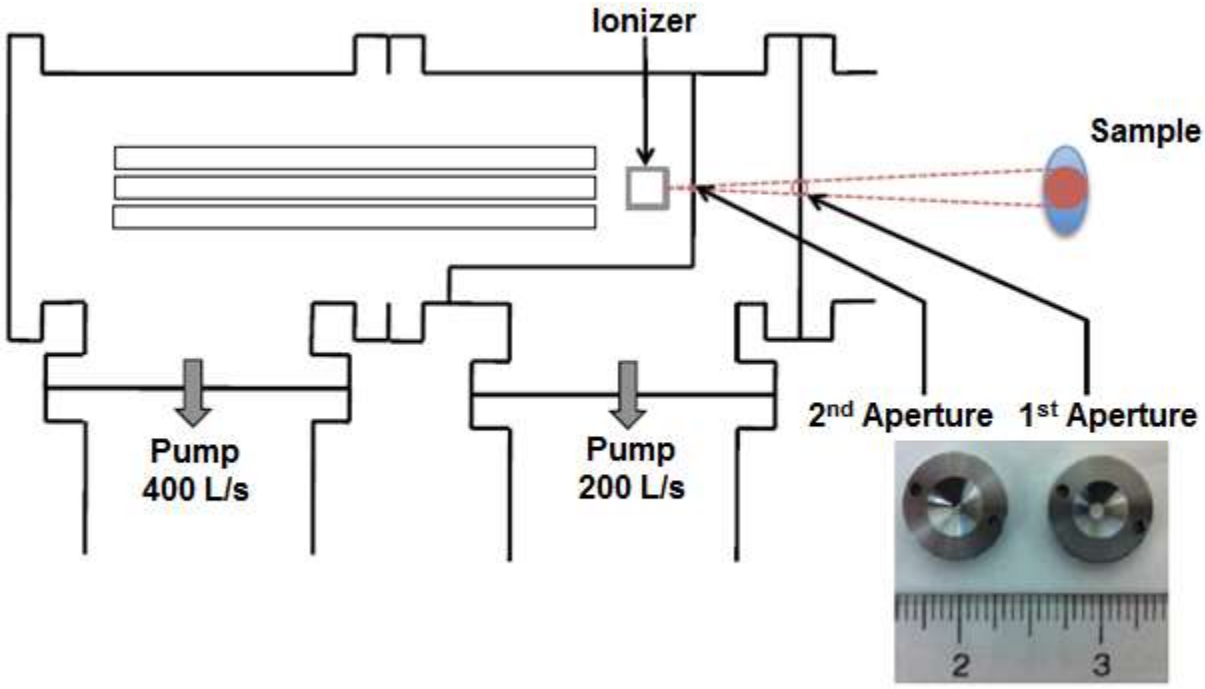

Figure 24. *Schematic of the mass spectrometer and double differentially pumped chambers*

The apertures also physically blocked molecules that desorbed from the mesh adjacent to the sample from reaching the mass spectrometer. **Figure 25** shows the geometry of the apertures. Metric dimensions are listed in **Table 6**. Any molecules from outside of the area defined by the red lines on the sample hit the chamber walls surrounding one of the two apertures. These aperture dimensions were chosen based on simple trigonometric calculations.

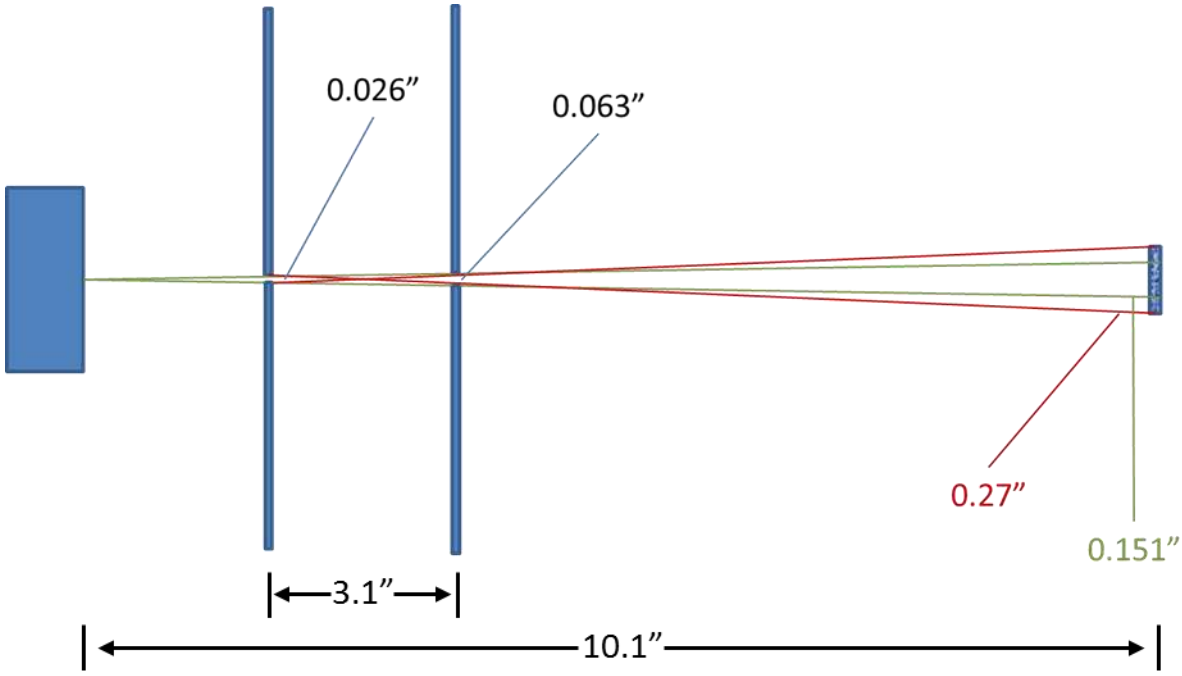

Figure 25. *Schematic of the line-of-sight path defined by the mass spectrometer chamber apertures*

Table 6. *Metric dimension of mass spectrometer apertures and positions of components*

Dimension	Distance (m)
ionizer to sample	3.05×10^{0}
2nd aperture to sample	2.57×10^{0}
1st aperture to sample	1.78×10^{0}
2nd aperature diameter	6.60×10^{-3}
1st aperature diameter	1.60×10^{-2}
spot in MS line-of-sight	6.86×10^{-2}

2.7 Temperature Programed Desorption

2.7.1 Inversion Analysis

Analysis of TPD data by inversion of the Polanyi Wigner equation was the primary tool in this work to determine activation energies for desorption. The experimental details for TPD data acquisition will be described in later chapters as they had to be varied for each molecule, and the process of determining optimal conditions often led to scientifically interesting discoveries. However, the general process of data acquisition and analysis were the same for all molecules. A visualization of this process is provided in **Figure 26** and described in the following paragraphs. A series of Microsoft Excel spreadsheets and macros were developed to automate the analysis process, and can be considered part of the standard operating procedure for the instrument. Further information about the Excel files is provided in the Morris group data analysis archive.

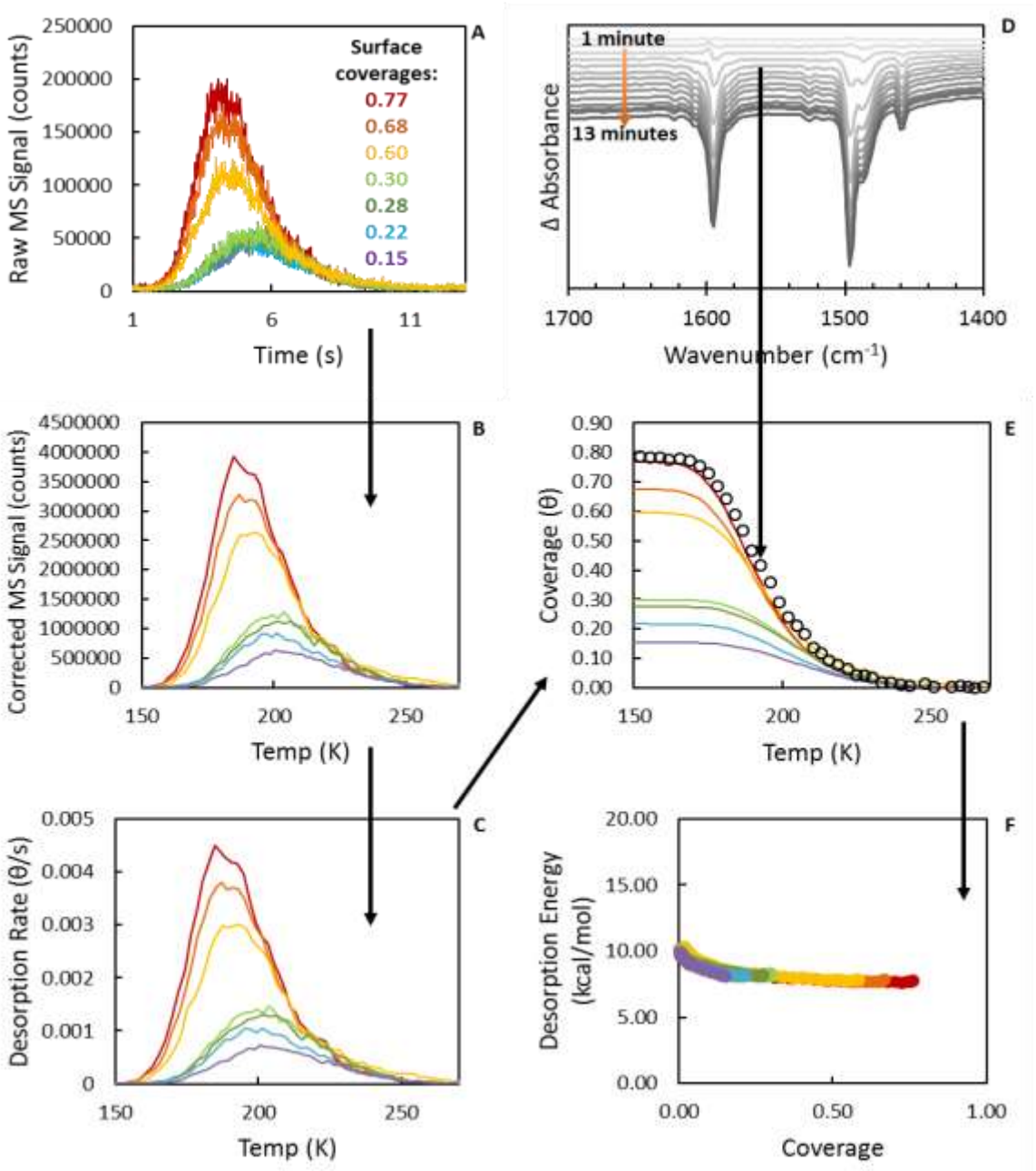

Figure 26. *Data analysis for fluorobenzene on silica. A) Raw mass spectrometer signal versus time. B) Mass spectrometer signal versus temperature after signal averaging and corrections for baseline, 1/v factor, and sensitivity factors (see text). C) Desorption rate versus temperature. D) IR spectra that show the disappearance of fluorobenzene from the surface (reference scan was the surface at time = 0). E) Coverage versus temperature. Circles were calculated from the spectroscopic data in panel D by integrating from 1560 to 1631 cm^{-1} F) Desorption energy versus coverage.*

The general approach for TPD experiments is to increase the temperature of a sample at a steady rate and measure the rate of desorption from the surface as a function of time. In a typical experiment to measure surface-adsorbate interactions, the sample's surface is covered with between 0.1 and 1.0 monolayers of adsorbate and kept at a temperature low enough to reduce the desorption rate to nearly zero. Surface coverages at the beginning of each TPD experiment were determined spectroscopically by comparing the intensity of the free SiOH band prior to gas dosing the same band immediately before starting the TPD procedure. As Arrhenius inferred from empirical observations, the rate constant for a simple process (e.g. desorption) increases exponentially with temperature. However, as the amount of molecules on the surface is finite, the overall desorption rate will eventually fall back to zero. These two processes are described mathematically by the Polanyi Wigner equation (**eq 2.5**). An algebraic rearrangement of **eq 2.5** to **eq 2.6** provides an equation for the activation energy of desorption as a function of constants and parameters that can be measured experimentally. Several steps were needed to obtain the necessary parameters in **eq 2.6** from experimental data.

$$-\frac{d\Theta}{dt}(\Theta, T_S) = \upsilon(\Theta, T_S) e^{-E_d(\Theta)/k_B T_S} \Theta^n \quad \textbf{(2.5)}$$

$$E_d(\Theta) = -k_B T_S ln\left(-\frac{d\Theta/dt}{\upsilon\Theta}\right) \quad \textbf{(2.6)}$$

Θ = fraction of total adsorption sites that are occupied
t = time
T_s = temperature
υ = prefactor
E_d = activation energy of desorption
k_B = Boltzmann constant
n = order or desorption (0,1,2, etc)

Raw TPD data was in the form of mass spectrometer signal intensity (counts per second) for selected molecular fragments as a function of time (see **Figure 26A**). In some cases, the signal

from multiple molecular fragments was summed in order to improve the signal-to-noise ratio. The temperature controller lacked the capability to output data in a digital form that could be saved directly to a computer and automatically synced with the mass spectrometer's timer. Therefore, the first step in analysis was to determine the temperature at each mass spectrometer data point. The temperature controller measured sample temperature with a type K thermocouple in units of mV. Thermocouple voltage was recorded in a notebook at 15-second intervals during the experiment, and the mass spectrometer data acquisition software was set up to save data points at approximately 1-second intervals. Given the slow rate of temperature change (0.2 K/s), the error associated with manually recording data is less than 0.1 K and therefore insignificant in comparison to other sources of experimental error in this work. As a consequence of the manual data acquisition, extrapolation was necessary to determine the thermocouple voltage at each mass spectrometer data point. A linear regression of voltage vs time for the entire experiment was not appropriate for this extrapolation because the temperature ramp was not linear especially at the beginning of experiments. Instead, a linear regression was calculated for the gap in between each time and voltage data point recorded in the notebook, and this equation was then used to calculate the voltage associated with each mass spectrometer timestamp. Further details and samples of the Excel spreadsheets used in this work are available in the Morris group data analysis archive.

Next, the thermocouple voltage was converted to temperature in units of K. The relationship between voltage and temperature is not linear for type K thermocouples especially at cryogenic temperatures. One method to convert voltage to temperature is to consult tables available from the online NIST ITS-90 Thermocouple Database.[91] Such tables require extrapolation for temperatures in between the measured data points. A 10^{th} order polynomial function is provided by NIST for this purpose. Alternately, Mosaic Industries[92] provides a rational

polynomial function that has been shown through statistical analysis[92] to have less error between calculated values and tabulated values than the NIST polynomial function[91]. Our work used the equation from Mosaic Industries to maximize the accuracy of the analysis.

The next goal in analysis was to correct the baseline of the mass spectrometer signal versus temperature plot and adjust for instrumental drift that may occur between experiments. Due to electronic noise and the presence of background gasses, the mass spectrometer signal was greater than zero even when the desorption rate from the surface was zero. Experiments were deliberately designed so the desorption rate was zero for at least the initial 60 seconds. The signal throughout these first 60 seconds was averaged, and this value was subtracted from all data points to correct for the non-zero background of the MS. The signal at the beginning and end of the experiment was zero after the correction. The signal was multiplied by sqrt(T) at this point of the analysis to account for the 1/velocity relationship between the number of desorbed molecules and the number of molecules ionized in the mass spectrometer. Specifically, ionization is more probable for molecules that travel through the ionizer at slower velocities. The average velocity of gas phase molecules is described by the equation $\bar{\upsilon} = \sqrt{8RT/\pi M}$ where $\bar{\upsilon}$ is the average molecular speed, R is the ideal gas constant, T is the temperature of the surface, and M is the mass of the molecule. Several measurements in this study were recorded while the electron multiplier was near the end of its life, which caused a steady decline in signal intensity each day. Over the duration of a series of experiments, which could take more than a week, MS signal could decrease by nearly 50%. However, the base pressure in the mass spectrometer chamber changed by less than 1×10^{-11} torr once the chamber had been evacuated for more than two weeks. Therefore, to correct for the drift in mass spectrometer signal, we assumed that the partial pressure of CO_2 inside the chamber remained nearly constant from day to day and used the CO_2 signal as a normalization factor.

Temperature conversion, baseline correction, and normalization were done in one Excel spreadsheet. The results of these corrections are shown in **Figure 26**B. Although every step of the analysis used all available data points, the data in this and subsequent plots have been signal averaged to improve visual clarity.

The next goal in analysis was to determine the preexponential factor and the desorption energy. TPD experiments often assume a value of 10^{13} s^{-1} for ν. This value can be derived from transition state theory, which provides the equation $\nu_{TST} = (k_B T/h)*(q^{\ddagger}/q_{ads})$ where $q^{\ddagger}$ and q_{ads} represent the single-particle partition functions for the transition and adsorbed states respectively.[93] If the entropy of molecules in the adsorbed and transition states is assumed to be the same, the ratio of transition state and adsorbed partition functions is one and $\nu \approx 10^{13}$ s^{-1} at room temperature. However, the entropy of adsorbed molecules in real systems should be lower than in the gas phase especially for larger molecules because of the restriction in translation and vibrational motions. Also, the possibility of readsorption after a molecule leaves its initial site on the surface of a porous or particulate sample may have an effect on the preexponential factor, which is often described as an attempt frequency for desorption. Both of these reasons provided us with compelling motivation to avoid assumptions and determine the prefactor experimentally for each adsorbate.

Work by Kay and coauthors[47,81,94,95] provided an approach to determine the prefactor from a series of TPD experiments. We based our data analysis procedures on Kay's work with the assistance of Excel macros to automate repetitive calculations. First, the mass spectrometer signal was converted to desorption rate. IR spectroscopy was used at the beginning of the experiment to determine the fraction of occupied adsorption sites (which is proportional to the number of molecules on the surface for the systems investigated in this work if the fraction is less than one), and again at the end to verify that the fraction of occupied adsorption sites was zero. Since mass

spectrometer signal is directly proportional to coverage, the area under the entire plot could be correlated to the total number of molecules on the surface, and, therefore, the area under two adjacent data points could be correlated to the change in surface coverage between those points. The data at this stage in the analysis was in the form of desorption rate as a function of temperature (**Figure 26C**). Coverage at any given temperature was equivalent to the integrated area under the TPD curve up to that temperature. IR spectra were collected during desorption (**Figure 26D**). The change in IR intensity of a fluorobenzene IR absorption band (1560-1631 cm^{-1}) for the maximum (0.77 ML) initial coverage experiment was normalized to surface coverage and plotted on top of coverages calculated from the mass spectrometer data (**Figure 26E**). The excellent agreement between IR and mass spectrometer data show that the IR signal is in the Beer's Law regime and supports our use of intensity as an indicator of coverage. All variables and constants needed to calculate desorption energies with the inverted Polanyi Wigner equation (**eq 2.6**) were available at this point, except for the preexponential factor.

A minimum of three TPD experiments, each with a different initial surface coverage, were used to determine the prefactor. We assumed that the prefactor was independent of coverage or temperature and used it as a fitting parameter to maximize agreement between simulated and experimental desorption rate curves. A macro was used to test a range of values for the prefactor and find the optimal value. Simulated desorption rate cures were generated for each prefactor by the following procedure. The desorption rate was determined as a function of coverage for the TPD experiment with the highest initial coverage (**Figure 26F**). Through numerical integration, simulated plots of desorption rate as a function of temperature were generated from this highest coverage run for all experiments with a lower initial coverage. The details of Excel functions and commands used to generate the simulated plots are available in the Morris group data analysis

archive. The sum of the squared residuals (SSR) was calculated for each pair of simulated and experimental desorption rates. **Figure 27** shows visual representations of good and poor agreement between simulated and experimental desorption rates. A plot of SSR versus the log of the prefactor was generated and fit to a 6^{th}-order polynomial function (see **Figure 28**) Solver was used to find the minimum of the polynomial, which was then output as the value for the optimized prefactor and used to calculate the final reported desorption energy for that molecule.

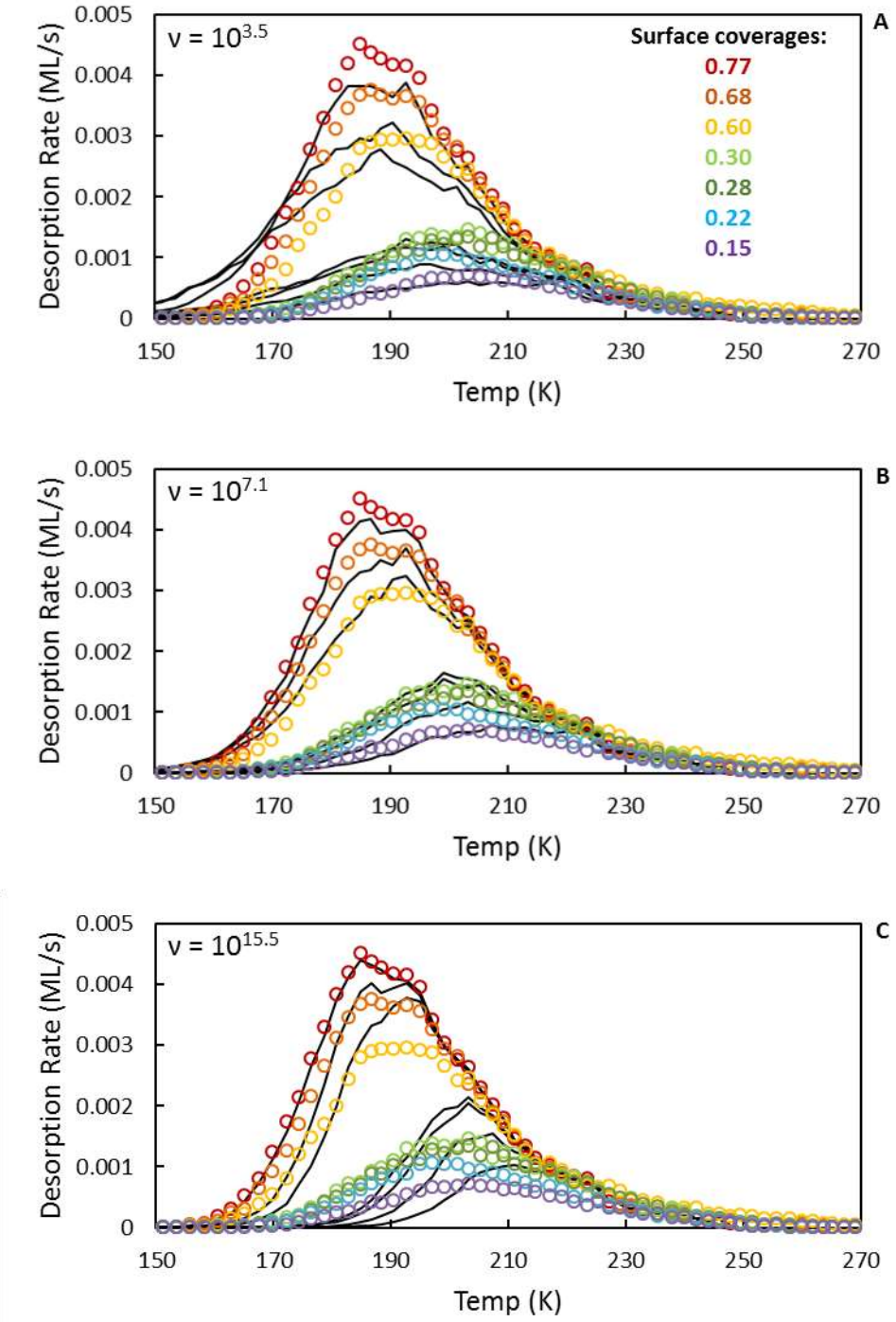

Figure 27. *Simulated (black lines) and experimental (colored circles) desorption rate plots for prefactor values that are too high (A), optimized (B), and too low (C). 1 ML/s = 1 θ/s*

B

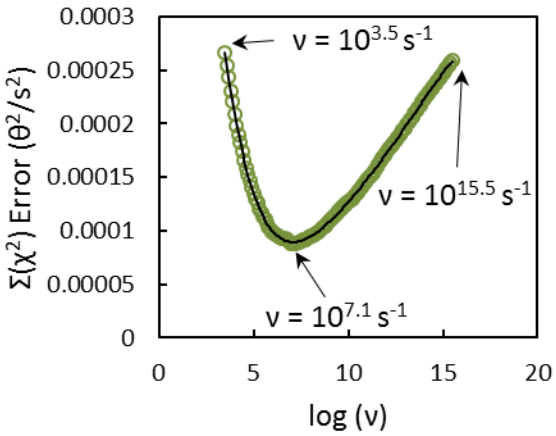

C

Figure 28. *The sum of the squared residuals for experimental versus simulated desorption rates for a range of prefactor values (open circles) and the polynomial function used to find the optimal prefactor value. The labelled prefactor values refer to the three panels in* ***Figure 27****.*

2.8 Method Validation

Our experimental approach and data analysis were validated with multiple methods. Although the experimental equipment used for this work was based on other instruments reported in peer-reviewed literature, the highly custom nature of such equipment required careful evaluation of data reproducibility and sources of systematic experimental errors. Additionally, although the method of our TPD data analysis was also based on peer-reviewed literature, a plug-and-play program was not available to process our raw data. Custom Excel macros and spreadsheets were written to handle all calculations related to TPD data analysis.

2.8.1 Validation of instrumental accuracy

The activation energies for desorption from silica and UiO-66 measured in this thesis and previous work using the same equipment are novel work and therefore cannot be directly compared to literature values for validation. However, values for heats of sublimation for various molecules are readily available. For the simple case of molecular desorption from multilayers, the desorption energy measured by TPD should be similar to the sublimation energy.[47] Thus, we can approximate sublimation energies experimentally with TPD from silica if the surface is exposed to the molecule under investigation for a sufficiently long period to occupy all available silanol sites and form a multilayer. Desorption from multilayers is mainly affected by molecule-molecule interactions rather than molecule-surface interactions, and can be modeled with zero-order kinetics.[47] Specifically, the surface coverage dependence is eliminated from the Polanyi Wigner equation (**eq 2.7**), which leaves the expression shown in **eq 2.8**. Thus a plot of the natural logarithm of desorption rate (measured by the mass spec) versus 1/*T* yields a line with slope equal to the heat of sublimation. For analysis, the data is truncated to exclude the low temperature limit where desorption rate is low and the high temperature limit where the assumption about coverage independence becomes invalid.

$$\frac{-d\theta}{dt} = (\theta)^n \nu(\theta, T) e^{-E_a(\theta,T)/RT} \quad \textbf{(2.7)}$$

$$\ln(-d\theta/dt) = \ln \nu - E_a/RT \quad \textbf{(2.8)}$$

A plot of desorption rate versus temperature for four multilayer bromobenzene on silica TPD experiments is presented in **Figure 29A**. Data below 180 K and above 205 K are excluded from the analysis. Plots of -1/*RT* versus ln(-*dθ*/*dt*) for all remaining data points are shown in **Figure 29B**. We performed linear regression analysis on each data set. The average of the slopes is

reported in **Table 7** as E_d for multilayers along with the standard deviation of the slopes. E_d values for multilayers of p-xylene, iodobenzene, and chlorobenzene on silica calculated via the same method are also reported in **Table 7**. The experimental values for p-xylene, bromobenzene, and chlorobenzene are within one standard deviation of the cited literature results.[96] Only one multilayer experiment was performed for iodobenzene, therefore no standard deviation is reported.

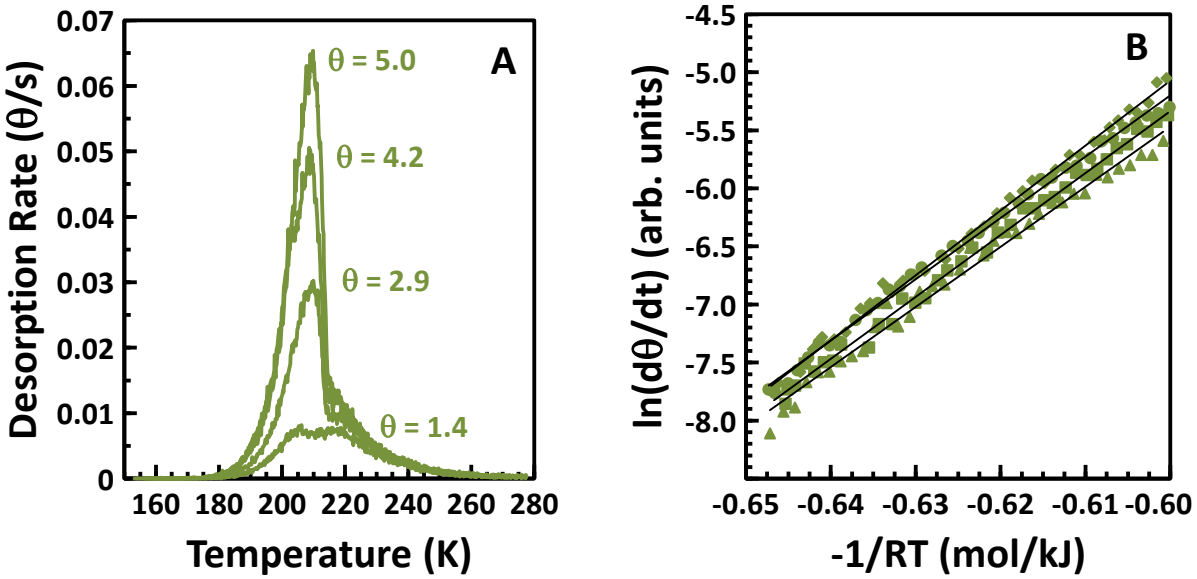

Figure 29. *Example of data used to calculated heats of sublimation in this work. A) Plot of desorption rate as a function of temperature. B) Plot of the natural log of the desorption rate versus 1/T. Trendlines from the linear regression analysis are shown as black lines.*

Table 7. *Comparison of sublimation enthalpies measured in this work to values obtained from NIST. All units are kJ/mol.*

molecule	measured E_d (multilayers)	literature ΔH_{sub}
p-xylene	53.6 ± 1.7	53
Iodobenzene	53.8	53
Bromobenzene	52.6 ± 2.5	53
Chlorobenzene	48.5 ± 2.8	47

2.8.2 Validation of inversion analysis calculations

The Excel spreadsheets and macros used to calculate prefactors and desorption energies from TDP data in this work were applied to data from the literature to verify that our results agreed the other authors' results and thus check for bugs or coding errors in our approach. Zubkov et al. plotted N_2 desorption rates from amorphous solid water versus temperature for ten different initial coverages of N_2 from 0.09 ML to saturation at 1 ML. Data analysis in the paper used the inverted Polanyi Wigner equation and determined the prefactor from experimental data in the same way that we do here. This experiment was similar to ours in that it involves first order kinetics and adsorption is mainly driven by surface-adsorbate interactions. Data points for five of the experiments (approximately 200 points for each) were manually selected from the published TPD plot on a computer with the aid of Engauge Digitizer Version 8.2 for Windows[97] and then processed with our Excel files. The literature-reported values were $\nu = 10^{13.8}$ s^{-1} and E_a = ~11 kJ/mol at 0.1 ML coverage. Our results were $\nu = 10^{13.1}$ s^{-1} and E_a = 10.4 kJ/mol at 0.1 ML coverage. This difference is low (one order of magnitude difference in the prefactor typically changes E_a by 1-2 kJ/mol) and may have been lower if our analysis was based the original data collected by the authors instead of manually selected points from a published plot. **Figure 30** shows the experimental data points and the simulated TPD plots.

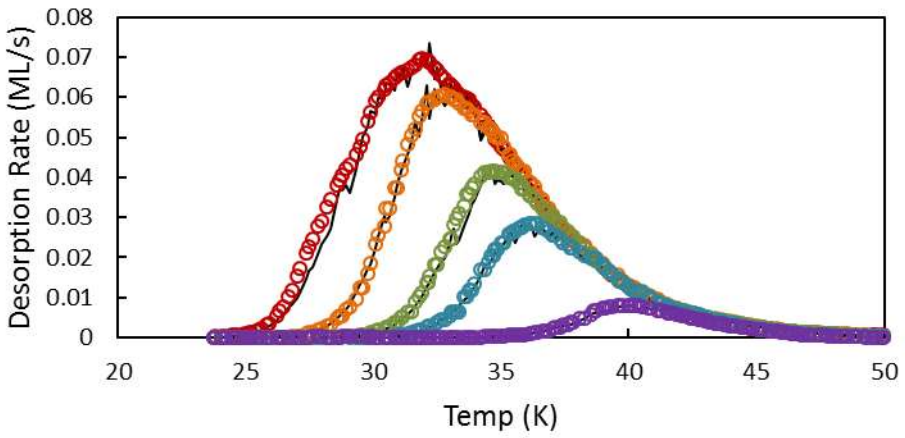

Figure 30. *Simulated (black lines) and experimental (colored circles) desorption rate plots based on data from Zubkov et al.*[94] *The experimental data plots were generated by digitizing data from FIG. 1 in the published paper. The simulated data plots were generated by the Excel spreadsheets and macros used to analyze all TPD data in this thesis.*

2.8.3 Evaluation of correct experimental procedure.

In order to effectively interpret TPD data, it is important to understand whether surface-adsorbate or adsorbate-adsorbate interactions are dominant. Desorption from coverages of multiple layers is largely controlled by adsorbate-adsorbate interactions and the desorption energy should be the same as the sublimation energy. Although sublimation energies are interesting and provide a convenient way to calibrate the instrument as described above, they are not the main focus of this thesis. In a typical TPD experiment, desorption should be largely controlled by adsorbate-surface interactions. Therefore, experiments were carefully performed to ensure surface binding sites were not saturated.

Multiple methods exist to determine saturation, or $\theta = 1$ of surface binding sites. For silica, $\theta = 1$ is defined as full occupation of the free silanol sites. This state can readily be observed spectroscopically when the intensity of the free OH IR absorption band decreases to zero. The same method works for hydroxylated UiO-66, where $\theta = 1$ is again defined as full occupation of the hydroxyl sites. Dehydroxylated UiO-66 lacks a convenient spectroscopic signature to probe

surface coverage or occupation of binding sites. However, the shape of the TPD curve allows identification of the point at which the strongest binding sites become saturated. For example, **Figure 31** shows TPD plots for desorption of 1-chlorobutane from dehydroxylated UiO-66. The six plots with the lowest initial coverages have a single peak and align on the trailing (high temperature) sides of the distributions. These data are representative of strong adsorbate-MOF interactions and indicate that adsorbed molecules have sufficient mobility to find the strongest available binding sites before desorbing. The higher coverages have additional low-temperature features. The shape of these features suggests a different, lower-energy binding mechanism as will be discussed further in Chapter 6. Thus the highest TPD plot with a single peak was used to define $\theta = 1$. Inversion analysis was only performed on data with initial coverages below saturation to determine desorption energies representative of adsorbate-MOF interactions. Leading edge analysis was used on the low-temperature features to calculate the desorption energy for these more weakly bound molecules.

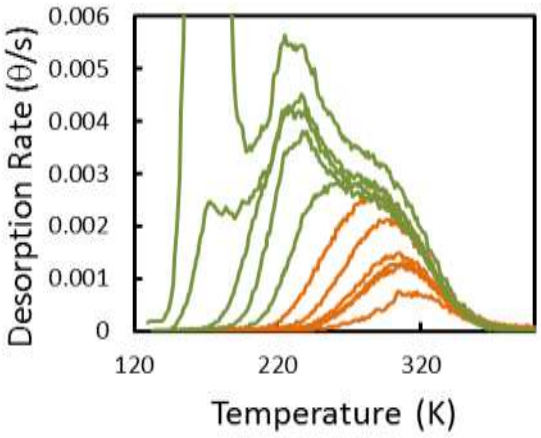

Figure 31. *Desorption rate vs temperature plots for several multilayer (green) and sub-monolayer (orange) initial coverages of 1-chlorobutane from dehydroxylated UiO-66.*

TPD experiments must provide data representative of the whole sample. It is important to ensure the temperature ramp rate is not too fast relative to the rate of diffusion of molecules through

the surface. Molecules must have time to diffuse through the particulate sample before desorption. The alignment of multiple TPD plots with different initial coverages provides easy verification that heating rate is not higher than diffusion rate. For example, desorption of 1-chlorobutane from UiO-66, shown in **Figure 31** above, is expected to be limited by molecule-surface interactions rather than molecule-molecule interactions. Therefore, the desorption rate in later stages of a temperature ramp should be independent of initial coverage and distribution if molecules are able to relocate to the strongest available sites during the ramp. As shown in **Figure 31**, all of the TPD plots align at the high-temperature trailing edges, which shows desorption rate is the same in this region regardless of initial coverage.

Prior to starting a TPD experiment, the adsorbed molecules must be uniformly distributed throughout the packed bed of particles. A controlled temperature ramp was used prior to nearly all TPD experiments (exceptions are described in later chapters) to give adsorbed molecules sufficient energy to diffuse throughout the particles. Uniform distribution of the adsorbates after the pre-TPD treatment was confirmed experimentally by comparing plots of desorption rate versus temperature. Non-uniform surface coverage was evidenced by broadening at the leading, high temperature edges of the TPD distributions for experiments with similar initial coverages but different pre-TPD temperature treatments.[95]

For example, **Figure 32** shows plots of mass spectrometer signal (which is directly proportional to desorption rate) versus temperature for three diethyl sulfide desorption experiments on silica. A 0.2 K/s temperature ramp from 150 K to 198 K (red lines) and 208 K (blue line) was performed for three of these experiments immediately after dosing, and the resulting TPD distributions had good alignment with each other. For a fourth experiment (black line), TPD was performed immediately after dosing, resulting in a TPD distribution with higher desorption rates

on the low-temperature edge. This can be attributed to a preference for diethyl sulfide to adsorb to the upper layers of the bed of silica particles during initial uptake.[98] The disproportionate concentration of molecules initially at the outer edge of the bed of particles increased low-temperature desorption, which changed the prefactor determined by inversion analysis (as described above) and therefore also directly affected the calculated desorption energy. A temperature ramp to 198 K prior to TPD allowed the adsorbed molecules to diffuse further into the sample and reduced low-temperature desorption. Increasing the temperature to 208 K did not cause an additional change in the low temperature edge, which is evidence that both pre-treatment conditions caused a similarly uniform distribution of adsorbates throughout the silica particles prior to TPD. Based on these and similar series of experiments on other molecules, the procedure for determining appropriate anneal conditions specified that TPD investigations should include experiments with different pre-treatment temperatures and that all should line up with each other.

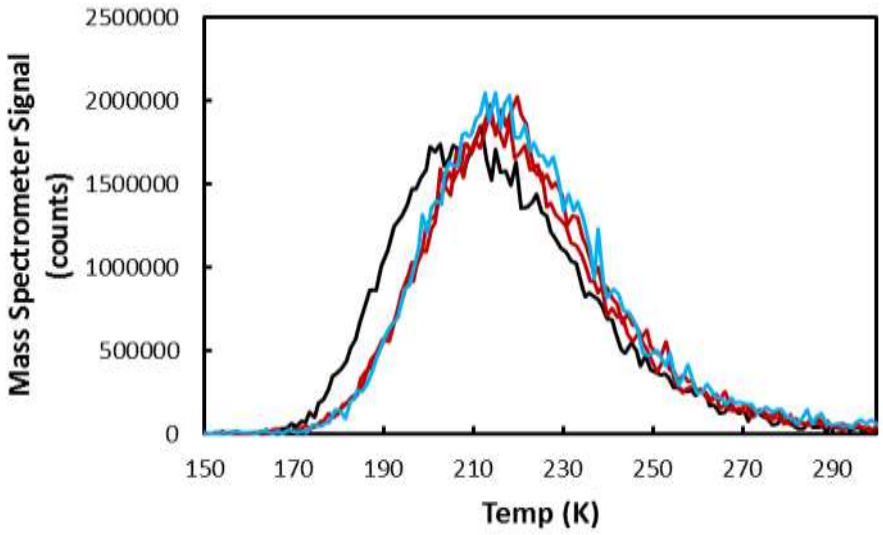

Figure 32. *Plots of mass spectrometer signal intensity for the largest fragment (75 amu) of diethyl sulfide versus temperature for a series of experiments with different anneal conditions. The black line represents an experiment with no heating between dosing and TPD. The red lines represent*

experiments with a pre-TPD temperature ramp to 198 K. The blue line represents an experiment with a pre-TPD ramp to 208 K.

2.9 Summary

A significant portion of the research presented in this thesis focused on the development of instrumentation, experimental methods, and data analysis procedures to measure and probe surface-adsorbate interactions. Specifically, a custom UHV chamber equipped with a variety of analytical tools was used to maintain a clean, well-characterized environment during experiments and allow in-situ analysis with multiple techniques. A high-surface area sample was mounted on a tungsten grid in a way that allowed fine control of temperature and position. IR analysis provided information about changes in molecular vibrational modes to identify molecules on the surface and to probe the formation and breaking of bonds. The mass spectrometer was operated in a way that allowed selective detection of desorbed molecules to determine the desorption energy. These techniques were combined to give a richer understanding of the adsorption mechanism than would be possible with either method by itself. Multiple benchmark experiments were performed to establish a reasonable degree of confidence in the validity and accuracy of the methods used to collect and analyze data. The subsequent samples demonstrate how the methods described in Chapter 2 were employed to characterize the adsorption and desorption of a variety of functionalized alkanes and aromatic molecules on silica and UiO-66 in order to establish structure-function relationships and explore the interplay among the different forces that drive uptake.

Chapter 3: Adsorption of Sulfur Mustard and Sulfur Mustard Simulants on Silica

3.0 Introduction

Sulfur mustard [bis(2-chloroethyl) sulfide, HD] is an extremely toxic compound that saw widespread use in the First World War as a vesicant chemical warfare agent (CWA).[1] Although the Chemical Weapons Convention (CWC) in 1997 mandated the destruction of mustard stockpiles worldwide, HD can be readily synthesized by terrorists or militaries who choose to ignore the CWC policies.[4] Furthermore, HD is known to be persistent in the environment and can remain at sufficiently high concentrations to pose serious health risks several years after initial deployment.[5] Motivated by this threat, researchers have directed significant effort toward the design of effective protection strategies including sorbent materials, decontamination procedures, and sensors. These technologies often rely on molecule–surface interactions or reactions that are tailored to achieve a particular outcome. However, surprisingly little is known about the fundamental nature of the surface chemistry of sulfur mustard.

As HD, a moderate vapor pressure liquid at room temperature, interacts with the surface of a material, it may accommodate to the surface prior to desorption, diffuse into the bulk of a porous material, or undergo a chemical transformation. The pathways that govern a particular HD–surface interaction are governed largely by the initial binding energy of the molecule, which controls the molecular residence time on the surface. For molecules like HD that have multiple functional groups with available lone pairs of electrons, one of the most likely initial binding pathways is through the formation of hydrogen bonds with surface hydroxyl groups. For example, interfacial hydrogen bonding has been shown to be the critical first step in the decomposition of 2-chloroethyl ethyl sulfide (2-CEES or "half-mustard") on the surface of a hydroxylated SiO_2–TiO_2 composite

nanomaterial.[14,44] Furthermore, surface hydroxyl groups are ubiquitous in nearly any environment, as they decorate the surface of metals, metal oxides, and organic materials. Therefore, the primary focus of the work described below is to provide fundamental insight into the strength and structure of HD–surface hydrogen-bonding interactions through the systematic study of key mimics of the actual chemical warfare agent.

Research on CWAs typically employs simulants, which are intended to mimic the chemical properties of the live agent without the risk of exposing laboratory personnel to extremely toxic compounds. The most common simulant for HD is the commercially available compound 2-CEES. HD and 2-CEES are structurally nearly identical and differ only by an additional terminal chloro functional group in HD.

Hydrogen-bonding interactions between 2-CEES and the free hydroxyl groups on the surface of a mixed TiO_2–SiO_2 composite material were previously explored with infrared spectroscopy.[14,44–46] In those studies, the IR absorptivity of isolated SiO–H stretches on the surface was monitored during 2-CEES adsorption. The data revealed that the SiO–H infrared band underwent extensive changes, indicative of hydrogen-bond formation with both the Cl and S moieties of the adsorbate. The three key changes in the SiO–H band included a shift to lower frequencies, a broadening of the band, and an increase in the absorptivity of the band. Interestingly, the previous work demonstrated that the magnitude of each effect was significantly different for hydrogen bonding through the Cl or the S groups. This effect was ascribed to differences in the electronic structure of the moieties, the result of differing degrees of hybridization in the lone-pair electrons of the hydrogen-bond acceptor. One might then speculate that these differences also affect the strength of the hydrogen bonds.

Although the hydrogen-bonding energy between a 2-CEES or HD molecule and hydroxyl-containing compounds on surfaces has not yet been (to the best of our knowledge) reported in the literature, several recent studies focused on the energetic and mechanistic details of hydrogen bonding for similar compounds in the gas phase.[25,43] The understanding that emerged from those studies is that the character of a hydrogen bond, including its strength, bond length, and spectroscopic signatures, is highly dependent on both electrostatic interactions and the extent of charge transfer between a nonbonding orbital of the acceptor and an antibonding orbital of the hydride donor.[25] For example, a comprehensive computational study[43] of hydrogen-bonding interactions at the ωB97X-D/aug-cc-pVTZ level of theory showed that the OH stretching frequency for the hydrogen-bond donor in H_2O shifted by 88 cm^{-1} when it formed a bond with the chloro group of methyl chloride. However, the OH stretching frequency shifted by more than 200 cm^{-1} when water formed a hydrogen bond with the S moiety of dimethyl sulfide. Despite the large differences in the OH stretching frequency for these two hydrogen bonds, the calculated energies of the bonds differed by only 2 kcal/mol.[43] These computational investigations suggest that hydrogen-bond formation through both the Cl and S groups of 2-CEES (and HD) may contribute significantly to the energetics of adsorption on hydroxyl-containing surfaces.

The work presented here investigated the energy and mechanism of hydrogen-bond formation between 2-CEES, as well as a series of key probe molecules, and the surface of silica. Silica was chosen for this work not only because it is one of the most abundant materials found in environmental and industrial settings but also because it can serve as an effective model substrate with well-characterized interfacial hydroxyl groups that can be prepared in a highly reproducible manner. In these studies, transmission infrared spectroscopic measurements were used to probe changes to the vibrational frequency of SiO–H stretches during gas uptake and hydrogen bond

formation. Shifts in this band provide insight into the extent of charge transfer into the antibonding orbital of the hydroxyl group upon the formation of the hydrogen bond. However, binding energy depends on a complex interplay between charge transfer, electrostatic forces, and other intermolecular forces that cannot be predicted from spectroscopic measurements alone. Therefore, we employed temperature-programmed desorption (TPD) methods to interrogate the activation energy for bond breaking and desorption and thus gain insight into the strength of the hydrogen bond. Performing these studies under ultrahigh vacuum (UHV) conditions ensured that the silica surface remained free from contamination throughout the experiment (see Section 2.1). The results provide fundamental insight into hydrogen bonding and the interactions at the gas–surface interface that play a role in HD uptake, residence time, and, ultimately, surface reactivity.

3.1 Experimental

3.1.1 Instrumentation

The instrumentation and general procedures used for this project were based on work previously reported by Wilmsmeyer et al.[40,41] Experiments were performed in an UHV chamber with a base pressure of 10^{-9} Torr. These low pressures were necessary to minimize the possibility of surface contamination on silica, which is a highly effective sorbent especially at cryogenic temperatures. Control experiments were performed to ensure that background water and other common UHV contaminants did not adsorb to the surface over the duration of a typical experiment. Specifically, infrared spectroscopic measurements showed no sign of changes to the silica sample (either in spectral regions assigned to OH or CH stretches) over several hours in a vacuum with the surface at a temperature of 130 K. The total coverage of contaminants in this work remained

low due to the very high vacuum and high surface area of the sample, which prevented detectable levels of contamination even after long durations.

Silica samples were prepared in a hydraulic press by packing approximately 5 mg of Aerosil (200 m^2/g surface area, 12 nm mean particle diameter) into a 50-μm thick tungsten mesh grid (Tech Etch). The pressing pressure, which was 4.4×10^8 Pa (64,000 psi) for this work, does not have a measurable effect on the experimental results. The mesh was mounted to a McAllister X-Y-Z manipulator via nickel clamps and 5 mm thick copper leads connected to an external power supply to achieve precise control of sample position and temperature. Sample temperature was monitored with a type-K thermocouple spot-welded to the mesh immediately adjacent to the silica sample. The mesh was heated resistively using a custom external power supply. The power leads and thermocouple wire passed through a tube in the manipulator, which could be filled with liquid nitrogen to cool the silica sample to cryogenic temperatures. Prior to each experiment, the silica sample was pretreated by heating to 700 K for 5 min, which removed possible trace surface contamination. Pretreatment also significantly dehydroxylated the surface such that it was dominated by isolated OH groups at an approximate density of ∼2 OH/nm^2.[86–90] After heating, the sample was cooled to cryogenic temperatures to maximize uptake during dosing.

3.1.2 Dosing

2-CEES, diethyl sulfide, 1-chloropropane, 1-chlorobutane, and 1-chloropentane (molecular structures are provided in **Figure 33**) were purchased from Sigma-Aldrich and transferred to stainless steel cylinders mounted on a gas-handling manifold configured with VCR seals and fittings. Each chemical was purified with two or more freeze–pump–thaw cycles immediately prior to use. These compounds are liquids at room temperature but have sufficiently

high vapor pressures to deliver gas-phase molecules to the UHV chamber through a directional capillary array doser positioned approximately 5 mm from the silica surface. Chloroethane is a gas at room temperature. A 500-gram cylinder was purchased from Sigma-Aldrich and mounted to the manifold by a regulator with a VCR fitting. The doser was mounted on a translation stage and retracted when not in use. The manifold was kept under vacuum at all times except during dosing to minimize contamination and was vacuum-heated for 12 h at over 500 K to clean the system between experiments. The temperature of the silica sample during dosing was adjusted for each molecule to attain high (at least 75%) coverage of surface hydroxyl groups within 3–7 min.

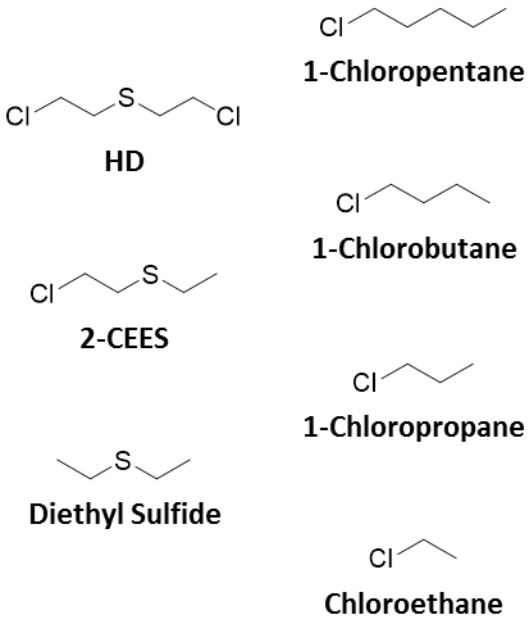

Figure 33. *Schematics for molecules tested in this study*

3.1.3 Infrared Spectroscopy

The silica sample was monitored with transmission Fourier-transform infrared spectroscopy (FTIR) before, during, and after dosing to identify adsorbed molecules and changes in surface vibrational modes. The IR spectra were recorded using a Nicolet Nexus 670 FTIR spectrometer integrated with the UHV chamber. All IR spectra consisted of 128 scans recorded at

4 cm^{-1} resolution. IR spectra of clean silica employed an empty spot on the mesh as the reference background. Spectra of species adsorbed on the silica sample employed a spectrum of the clean silica as a reference.

3.1.4 Post-dosing Heating

Previous work indicated that effective TPD measurements require a homogeneous distribution of adsorbed molecules throughout the particulate sample.[95] We achieved this goal with a controlled increase of sample temperature from the dosing temperature at 0.2 K/s to a target temperature high enough for the adsorbed molecules to diffuse and become homogenously distributed throughout the packed bed of particles. The temperature ramp also reduced the surface concentration of adsorbates to submonolayer coverages. Each molecule required a different temperature (219 K for 2-CEES, 198 K for diethyl sulfide, 163 K for 1-chloropropane, 181 K for 1-chlorobutane, and 193 K for 1-chloropentane) to achieve adequate diffusion without excessive desorption. Surface coverage for these molecules was controlled by varying the annealing duration and target temperature. After heating, the samples were rapidly cooled to or below the temperature used during dosing temperatures. In some cases, the sample was cooled immediately after reaching the target temperature, in others, the sample was held at the target temperature for up to several minutes. Chloroethane did not require heating to remove multilayers and achieve a uniform distribution on the surface, thus surface coverage was adjusted by varying dosing duration. Uniform distribution was verified by the alignment of the trailing edges of TPD plots as described in Chapter 2.

3.1.5 Temperature-Programmed Desorption

TPD experiments were performed by heating the sample and detecting desorbed species with a doubly differentially pumped, axially mounted quadrupole mass spectrometer (Extrel) tuned to the most abundant mass fragments for each molecule. The mass spectrometer provided line-of-sight detection and viewed a 0.35 cm^2 spot on the sample with an acceptance angle of ±0.4° such that the signal from molecules that desorbed from the sample holder was minimized. The heating rate for the TPD measurements was maintained at 0.2 K/s with a proportional-integral-derivative controller (Honeywell) and custom power supply. Further details about the TPD procedure are in Chapter 2.

3.2 Results

3.2.1 Infrared Spectroscopic Studies of Adsorption

Previous studies of 2-CEES and other polar compounds demonstrated the use of infrared spectroscopy in the characterization of interactions between silica and adsorbed molecules.[14,44] **Figure 34** shows a spectrum of clean silica immediately before exposure to the adsorbate. The sharp absorption feature at 3750 cm^{-1} is characteristic of free surface silanol groups.[99] The shoulder at 3700 cm^{-1} is indicative of geminal silanols, but the small size of this band relative to the main peak indicates that isolated silanols dominated the surface.[86–89,100] This is consistent with a previous study that measured the distributions of free, geminal, and hydrogen-bonded OH surface groups per unit area as a function of temperature from 473 to 1473 K.[90] The wavenumber region from 1400 to 650 cm^{-1} is dominated by bulk infrared modes of silica that obscure several adsorbate bands (see below), including those associated with the scissor mode for

CH_2 adjacent to Cl (1215 cm^{-1}) and the C–Cl stretch (600–800 cm^{-1}) for some of the molecules used in this work.

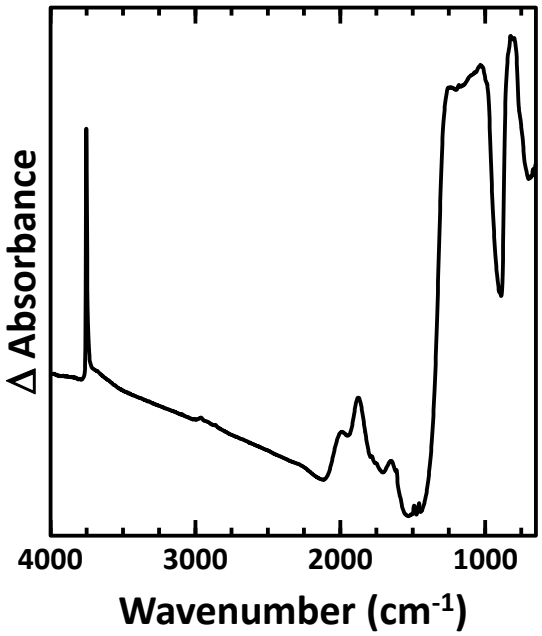

Figure 34. *Infrared spectrum of a clean silica sample following pretreatment at 700 K for 5 minutes (see text).*

IR difference spectra following uptake of 1-chlorobutane, diethyl sulfide, and 2-CEES on silica are presented in **Figure 35**. IR difference spectra for the silica particles following uptake of the aliphatic chloroalkanes are shown in **Figure 36**. The inverted feature at 3750 cm^{-1} is the result of a shift in that band as the surface silanol groups transformed from free SiOH to hydrogen-bonded groups. With the assumption that the absorbance intensity of the free OH band is directly proportional to the surface concentration of free OH, the decrease in intensity of the feature at 3750 cm^{-1} following exposure to the gas of interest can be used to determine the fraction of silanol groups involved in hydrogen bonding. In this study, surface coverage, θ, is reported in terms of the fraction of silanol groups bound to an adsorbate; for example, $\theta = 1$ represents occupation of all hydrogen-bonding sites. The monotonic profile and excellent alignment of the TPD curves

shown in **Figure 37** are evidence for the absence of multilayers. Furthermore, the decrease in IR signal from hydrogen-bonded silanol groups during desorption directly correlates with a decrease in adsorbate IR bands and a rise in mass spectrometer (MS) signal at the parent molecular mass. This correlation is evident in a plot of coverage versus temperature (**Figure 38**, where the $\theta = 0.9$ initial coverage plots have been calculated independently from mass spectrometer and IR data) and is evidence that the adsorbed molecules were bound through the SiOH groups.

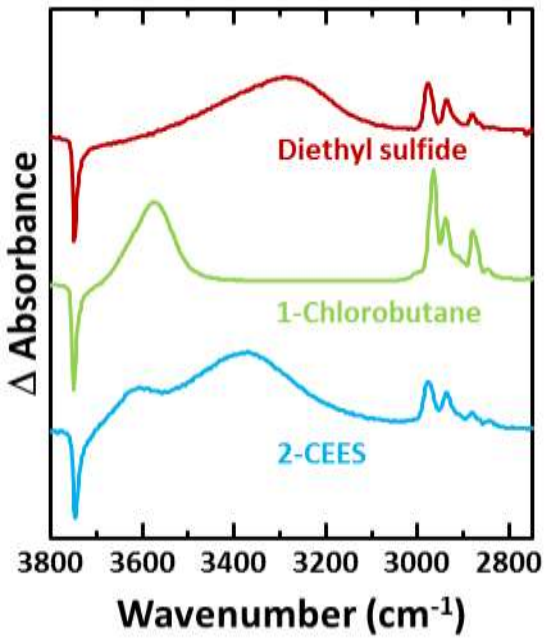

Figure 35. *Infrared spectra of adsorbed diethyl sulfide (top, red), 1-chlorobutane (middle, green), and 2-CEES (bottom, blue) on silica. The spectra are normalized to the integrated area of the free OH band such that the spectra represent equivalent effective SiOH occupation fractions, θ (see text).*

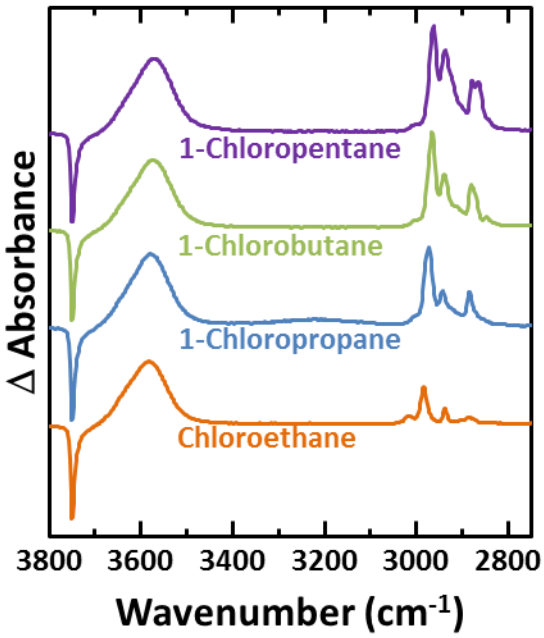

Figure 36. *Infrared spectra of adsorbed chloroalkanes.*

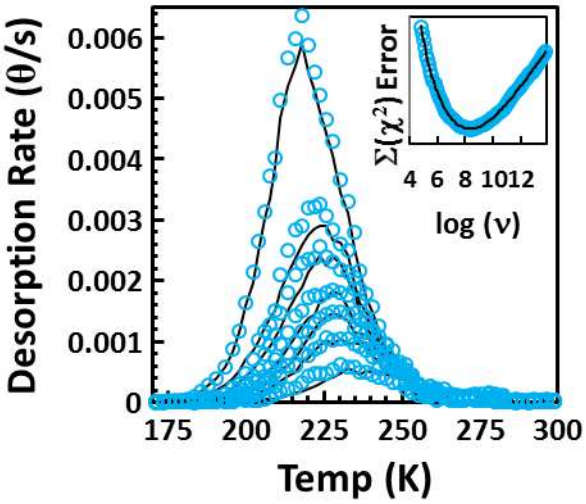

Figure 37. *Experimental (blue triangles) and simulated (black lines) TPD curves for 2-CEES at different coverages. From top to bottom: θ = 0.79, 0.46, 0.32, 0.21, 0.17. Inset shows a 6th order*

polynomial fit to χ^2 error values between simulated and experimental data used to determine the best prefactor value. $\Sigma(\chi^2)$ error has units of θ^2/s^2.

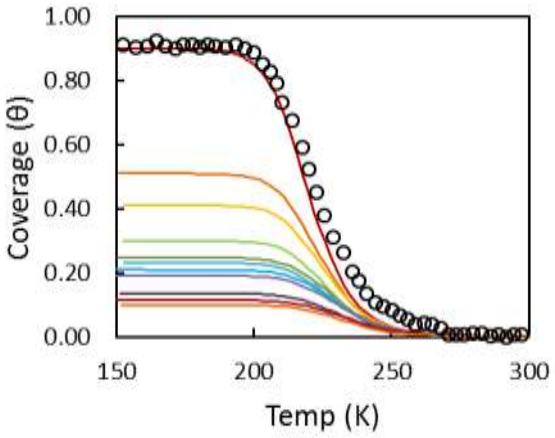

Figure 38. *Plot of coverage versus temperature for different initial coverages. Lines were calculated from mass spectrometer data. Black open circles were calculated from IR data, specifically the integrated area of the re-emerging free OH band from 3694 to 3787 cm^{-1}.*

The large shift in the silanol absorption band, clearly evident in **Figure 35** and **Figure 39**, indicate that hydrogen bonds responsible for the uptake of these molecules. Three key characteristics of the IR band for the SiO–H stretch stand out in the spectra for adsorbed molecules: (1) the SiO–H stretch band shifts to lower wavenumber (red-shift), (2) the hydrogen-bonded OH band has a much larger integrated intensity than the free OH band, and (3) this band broadens significantly upon adsorption. The red shift is due to charge transfer as the hydrogen-bond acceptor donated electron density to SiOH. Upon hydrogen-bond formation, π electrons from hydrogen-bond acceptors populate the σ^* antibonding orbital on the silanol, thereby weakening the O–H bond and adding significant anharmonicity to the stretching mode.[17,18] The increase in peak intensity is due to the greater oscillator strength of hydrogen-bonded donor stretches.[19] Finally, the band broadening occurs because of the inhomogeneity in the configuration of the hydrogen-bonded molecules, which affects the strength and anharmonicity of each bond in different ways.

Furthermore, coupling to other modes may have reduced the lifetime of the O–H vibration and increased the homogeneous band broadening.[20–23]

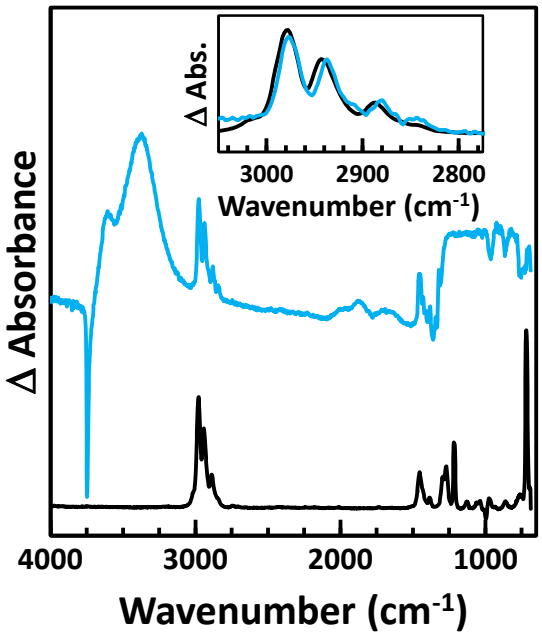

Figure 39. *The infrared spectra of gas-phase 2-CEES (black) and adsorbed 2-CEES on silica (blue). The inset contains a zoomed-in view of IR bands corresponding to methyl and methylene stretching modes.*

The bands near 3000 cm^{-1} are assigned to symmetric and asymmetric alkane stretching modes corresponding to molecules on the surface. A comparison of methylene stretching modes for each adsorbed molecule to corresponding gas-phase modes for the same molecule provides insight into the adsorption mechanism. **Figure 39** shows spectra of 2-CEES adsorbed on silica and in the gas phase. The relative integrated areas of each band are similar, which indicates molecular adsorption without subsequent decomposition or reaction. However, the bands assigned to $\nu_a(CH_2)$ and $\nu_s(CH_3)$ shift upon adsorption by 5 and 10 cm^{-1}, respectively, compared to the same modes in the gas phase. Similar shifts were observed in all molecules investigated. They are likely due to dispersion interactions with the surface, restricted molecular degrees of freedom for the adsorbates, and changes in the CH_2 bending modes (the first overtone is in Fermi resonance with the

CH_2 stretches). Unfortunately, the CH_2 bending modes could not be detected in the present work due to obstruction by the high absorbance of silica below 1500 cm^{-1}.

3.2.2 Temperature-Programmed Desorption

The desorption energies were determined with TPD. After dosing and annealing, the silica sample was heated at a constant rate of 0.2 K/s. This rate was chosen to allow adsorbed molecules sufficient time to diffuse throughout the pressed sample before desorbing. In this way, the molecules sample the strongest unoccupied surface sites, and the rate-limiting step for desorption is the rupture of those bonds. The mass spectrometer, tuned to mass fragments unique to the desorbing molecule, tracked changes in the gas-phase number density of the analytes as a function of surface temperature. The raw signal was then multiplied by $T^{1/2}$ to account for the 1/velocity dependence to ionization (hence detection) probability that affects line-of-sight, differentially pumped, mass spectrometric TPD measurements.[101] The resulting distribution was directly proportional to desorption rate. Molecular desorption, as opposed to decomposition on the surface and subsequent desorption of products, was confirmed by comparing the fragmentation pattern for the pure gases to that recorded during desorption. The desorption rates for 2-CEES at different initial coverages are shown in **Figure 37**.

The variation of the desorption rate with the initial coverage (see **Figure 37**) provides an understanding of bonding. The alignment of the trailing edges indicates that adsorbed molecules had sufficient mobility to diffuse to the strongest available adsorption sites during the temperature ramp prior to desorption.[95] The maximum in the desorption rate shifts to higher temperatures with lower coverage. This is evidence that the residence time and binding energy are governed by molecule–surface, rather than molecule–molecule forces. If molecule-molecule forces were

dominant, the maximum in the desorption rate would be expected to shift to lower temperatures with lower coverage as fewer molecule-molecule interactions would be able to form.

Quantitative interpretation of TPD spectra was based on the Polanyi–Wigner relationship (eq 3.1), which can be rewritten as eq 3.2 to express desorption energy as a function of coverage. The experimental TPD data were analyzed by using the inverted Polanyi–Wigner equation to determine the desorption energy at each temperature and corresponding coverage according to the methods outlined by others[95] and recently used to study the desorption energetics of molecules from particulate silica.[40,41] The desorption energies were then plotted as a function of coverage and modeled with first-order kinetics. Numerical integration of the desorption energy (E_a) versus coverage (θ) curve obtained from the highest experimental coverage gave simulated TPD curves for any desired initial coverage lower than that highest experimental coverage. The prefactor (ν in eq 3.1) was assumed to be independent of coverage and temperature for this type of analysis and was used as a fitting parameter to maximize agreement between simulated and experimental desorption rate curves. Specifically, the prefactor was adjusted to minimize the sum of the squared residuals between experimental data and simulated data at each coverage. **Figure 37** shows simulated data (black lines) obtained with an optimized prefactor plotted over the experimental E_a versus temperature data for five initial coverages. The inset shows the SSR plot used to optimize the prefactor.

$$-\frac{d\Theta}{dt}(\Theta, T_S) = \upsilon(\Theta, T_S) e^{-E_a(\Theta)/k_B T_S} \Theta^n \quad \textbf{(3.1)}$$

$$E_a(\Theta) = -k_B T_S ln\left(-\frac{d\Theta/dt}{\upsilon\Theta}\right) \quad \textbf{(3.2)}$$

After optimizing the Polanyi–Wigner prefactor, the reported desorption energy was determined from the plot of desorption energy versus coverage (**Figure 40** and **Figure 41**). The

curvature in this plot is likely due to a non-uniformity of the silica surface. Some silanol sites, defect sites in particular, likely provided unusually high binding energy sites on the surface. Furthermore, hydrogen bonding, though the most significant force in the uptake of these molecules, is not the only type of interaction that determines the overall binding energy. Other surface–adsorbate interactions, including dispersion forces, can significantly affect the activation energy for desorption. Thus, the local variations in silanol density likely affected the desorption energy for individual molecules. In this study, our focus was on the desorption energy of a single adsorbate on a defect-free region of the silica surface; therefore, the linear portion of the E_a curve was extrapolated to zero coverage by fitting each E_a curve to the function expressed in **eq 3.3** where A_0, λ, and m are fitting parameters. The intercept of the linear component of **eq 3.3** represents the activation energy for desorption at zero coverage (E_a). Desorption energy distributions for 2-CEES, diethyl sulfide, and 1-chlorobutane are presented in **Figure 40**. **Figure 41** contains desorption energy distributions for the chloroalkanes. The extrapolated, zero-coverage limit desorption energies for each of the molecules studied are presented in **Table 8**.

$$E_{fit}(\theta) = A_0 e^{-\theta\lambda} + m\theta + E_a \qquad \textbf{(3.3)}$$

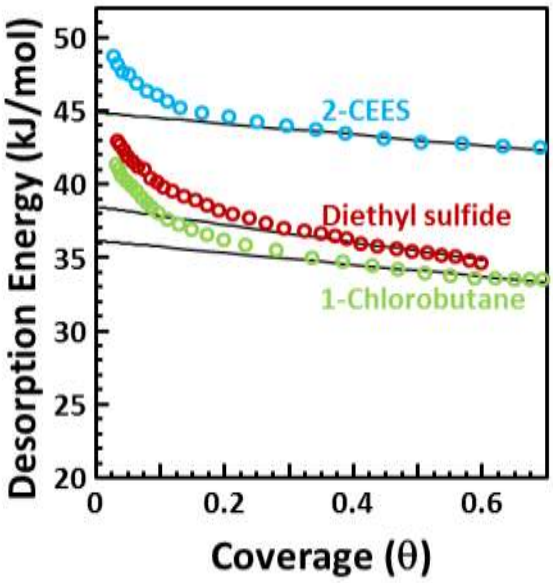

Figure 40. *$E_a(\theta)$ curves for the desorption of 2-CEES, diethyl sulfide, and 1-chlorobutane from partially hydroxylated silica.*

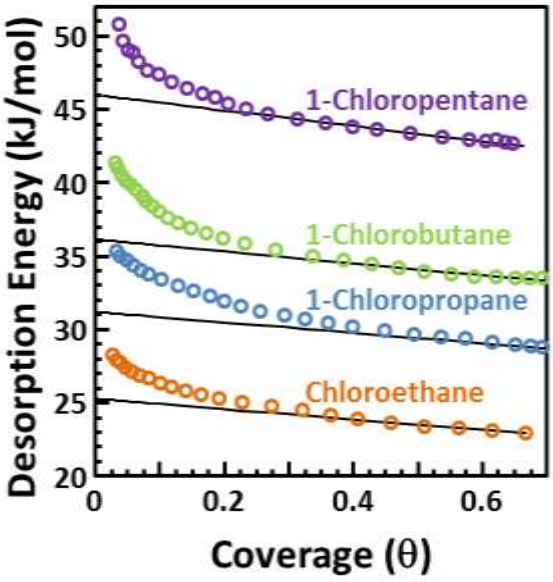

Figure 41. *$E_a(\theta)$ curves for the desorption of four chloroalkanes from partially hydroxylated silica.*

Table 8. *Desorption energies and pre exponential factors for all molecules tested in this study. Error values are ± one standard deviation calculated from three separate TPD experiments.*

molecule	E_a (± 2.3 kJ/mol)	log(ν) (± 0.6)
2-CEES	44.9	8.4
Diethyl sulfide	38.5	6.9
1-Chloropentane	46.0	9.7
1-Chlorobutane	36.1	7.8
1-Chlopropane	31.2	7.3
1-Chloroethane	25.2	6.3

3.3 Discussion

We explored the fundamental nature of gas–surface hydrogen-bond formation between simulant molecules (2-CEES, diethyl sulfide, and 1-chlorobutane) and partially hydroxylated silica to help construct an understanding of how the chemical warfare agent sulfur mustard gas bonds to hydroxyl-containing surfaces. In this study, infrared spectroscopy was employed to probe the extent of charge transfer, a key mechanistic step in hydrogen-bond formation, from the adsorbate to the hydroxyl group of a well-characterized silica surface. The overall strengths of the hydrogen bonds were gauged by performing TPD measurements to determine the activation energy for desorption. Together, these techniques provide insight into the roles that dipole–dipole interactions, charge transfer, and dispersion forces play in the uptake of mustard on polar surfaces.

3.3.1 2-CEES–Silica Hydrogen-Bond Formation

2-CEES uptake on silica is primarily driven by the formation of hydrogen bonds with surface hydroxyl groups. These hydrogen-bonding interactions are evidenced in the IR spectra of adsorbed 2-CEES (**Figure 39**), which clearly show the reduction of the band associated with free surface hydroxyl groups (reduced absorbance at 3750 cm^{-1}) as two new broad IR features, signatures of hydrogen bonding, emerge. The two broad but distinct IR absorbance features at

3598 and 3359 cm^{-1} are in the infrared spectral range associated with surface SiO–H stretches but are red-shifted significantly from the free silanol band. This red-shift reflects a decrease in the SiO–H vibrational energy caused by charge transfer from the hydrogen-bond acceptor to the antibonding orbital of the SiO–H bond.[43,102] In this way, infrared spectroscopic measurement of the SiO–H vibrational frequency serves as a probe of the extent of charge transfer in gas–surface hydrogen-bond formation and reveals two distinct types of charge donors (lone-pair hydrogen-bond acceptors) within 2-CEES.

The chlorine and sulfur moieties within the 2-CEES molecule are both potential hydrogen-bond acceptor sites. Therefore, we studied the uptake of 1-chlorobutane and diethyl sulfide to help identify the contributions from each acceptor. Spectra for adsorbed 1-chlorobutane show a strong absorbance feature at 3571 cm^{-1}, which is due to excitation of the SiO–H stretch associated with the Cl···H–OSi hydrogen bond. Diethyl sulfide also forms hydrogen bonds with the surface, but the band associated with the SiO–H stretch is much further red-shifted in the IR spectra. This band appears at 3280 cm^{-1}. Thus, we assign the 3598 and 3359 cm^{-1} absorption features in the IR spectra of adsorbed 2-CEES to Cl···H–OSi and S···H–OSi hydrogen bonds, respectively, in agreement with a previous study.[44]

The infrared spectral assignments reveal that the extent of charge transfer during uptake and hydrogen bond formation is greater for molecules that bind through the sulfur than through the chlorine constituents of the molecule and that both types of interactions occur for 2-CEES. However, the extent of charge transfer does not always correlate with the strength of the hydrogen bond. Electrostatic interactions can also play a major role in hydrogen-bond formation, and further measurements were necessary to assess the relative contribution of each type of hydrogen bond to

the overall adsorption process. Therefore, we performed a series of TPD studies to help determine the overall energy required to rupture the hydrogen bonds and drive the molecules from the surface.

3.3.2 Charge Transfer and Electrostatic Interactions

Previous studies in solution, in the gas phase, and at the gas–surface interface revealed a positive, linear correlation between $\Delta\nu$ (the shift in the frequency for the O–H stretch of a hydrogen bond) and intermolecular hydrogen-bond strength for electronically similar moieties.[39–42,103–105] Based on this previous work alone, one may infer that the larger $\Delta\nu$ in spectra of adsorbed diethyl sulfide ($\Delta\nu$ = 485 cm^{-1}) compared to 1-chlorobutane ($\Delta\nu$ = 190 cm^{-1}) is indicative of a stronger hydrogen bond. However, as described above, electrostatic (in this case, dipole–dipole) interactions also play a role in hydrogen-bond forces. Calculations indicate that the molecular dipole moments for 1-chlorobutane and diethyl sulfide are 2.47 and 1.68 D, respectively.[106] Thus, based on the magnitude of the dipoles, one might predict that 1-chlorobutane would form a stronger hydrogen bond with silanol than diethyl sulfide. This is contrary to the conclusion based solely on the extent of the red shift in the SiO–H vibrational frequency in the hydrogen-bonded complexes.

The interplay between dipole–dipole interactions and charge transfer was explored in a recent computational study on hydrogen bonding of dimethyl sulfide and chloromethane to gas-phase water (among a variety of other species).[43] In that study, $\Delta\nu$ for the O–H stretch was 125 cm^{-1} larger for water bound to dimethyl sulfide than for water bound to chloromethane. However, the calculated hydrogen-bond strengths for both molecules were similar relative to other molecules studied in that work. Analysis of our TPD measurements for diethyl sulfide and 1-chlorobutane (See **Figure 40** and **Table 8**) is consistent with these calculations. That is, the activation energies for desorption for diethyl sulfide and 1-chlorobutane from silica are found to be indistinguishable

within the error bars for these measurements (38.5 ± 2.3 and 36.1 ± 2.3 kJ/mol). Thus, we conclude that differences in the charge transfer contribution are balanced by other intermolecular forces, such as dipole–dipole interactions, to yield similar activation energies for desorption. Therefore, in the case of 2-CEES adsorption, hydrogen-bond formation through the sulfur or the chlorine component likely leads to very similar binding strengths (similar to those of diethyl sulfide and 1-chlorobutane) for isolated 1:1 type interactions. However, if 2-CEES were to interact simultaneously with an SiOH group through the chlorine and another SiOH group through the sulfur, then the activation energy for desorption may be much higher, a topic discussed further in the following section.

3.3.3 2-CEES Adsorption Mechanism

We investigated whether each adsorbed 2-CEES molecule interacts with a single silanol group (1:1 adsorbate:silanol ratio) or two adjacent silanol groups (1:2 ratio). As described above, the surface hydroxyl density on silica pretreated to 700 K is estimated to be greater than 2 OH/nm^2, which is equivalent to an approximate spacing of 0.7 nm between silanols.[5,16,90] This spacing is likely sufficient to allow the two polar functional groups in 2-CEES, separated by an ethyl chain, to simultaneously bind to adjacent hydroxyls. However, analysis of the relative surface coverages for 2-CEES and diethyl sulfide at identical SiOH occupation densities suggests that 2-CEES adsorbs in a similar manner as diethyl sulfide; that is, there is only one molecule–surface hydrogen bond per adsorbed molecule. More specifically, the spectra presented in **Figure 35** have been normalized such that they represent the same number of occupied SiOH surface sites. At this coverage, the integrated areas under the bands for the CH_2 asymmetric stretching mode of each molecule differ by less than 20%, strongly suggesting that the adsorbate-to-SiOH ratios

(necessarily 1:1 for diethyl sulfide) are the same. This conclusion is supported by the TPD data, which indicates that the desorption energy for 2-CEES is only 15% greater than that of diethyl sulfide, as opposed to the much larger energy increase one might expect if two hydrogen bonds are formed per molecule. In fact, Bermudez et al. showed that bidentate hydrogen bonds can be as much as a factor of two great than the monodentate bonds.[107]

3.3.4 Stabilization from Secondary Interactions

The slightly higher desorption energy for 2-CEES compared to the energies for 1-chlorobutane or diethyl sulfide is likely due to surface–adsorbate interactions other than the hydrogen bonds. Weaker secondary interactions likely play a role in controlling the activation energy for desorption. Previous work reported a binding energy increase of 7 kJ/mol per additional methylene for a series of linear hydrocarbons on MgO(100).[108] We observed a similar trend on amorphous silica. **Figure 41** shows the coverage-dependent desorption energies for a series of linear chloroalkanes that differ only by alkane chain length. As with 2-CEES, diethyl sulfide, and 1-chlorobutane, the desorption energy is largely invariant with coverage, except for the lowest coverages due to a small concentration of sites that lead to unusually high binding energies. The linear portions of the $E_a(\theta)$ distributions are extrapolated to the zero coverage limit and the values are provided in Table 1. The chloroalkane desorption energies range from 25 kJ/mol for the shortest chain molecule to 46 kJ/mol for the longest chain molecule. Each methylene group contributes 4–10 kJ/mol to the overall desorption energy. It is unlikely that this energy difference is caused by changes to the SiO–H···Cl hydrogen-bond strength, because the fundamental nature of the hydrogen bonds, as gauged by the SiO–H stretching frequency ($\Delta\nu$ = 180 cm^{-1} for all four molecules), appears to be identical (see **Figure 36**). Furthermore, calculations indicate that the

magnitudes of the dipoles for the chloroalkanes are not strongly dependent on chain length. The permanent dipole moments range from 2.3 D for chloroethane to 2.5 D for 1-chloropentane.[106] Thus, the measured increase in desorption energy as a function of chain length likely arises from surface–adsorbate dispersion interactions. Based on these results, we reason that similar dispersion interactions for the larger 2-CEES molecule, relative to diethyl sulfide and 1-chlorobutane, account for the differences in the desorption energies for these molecules. Finally, we note that, in addition to the desorption energy, the Polanyi–Wigner pre-exponential factors (ν) for this series of chloroalkanes depend on chain length. This phenomenon is well-known from other work[108] and is likely due to the increased entropic penalty of constraining larger molecules to a surface as well as differences in the diffusivity of the molecules through the silica particles.[108]

3.3.5 Comparison to HD

A major motivation of this work was to develop insight into the desorption energetics and binding mechanisms for the chemical warfare agent HD on the surface of an environmentally relevant hydroxylated material. HD has the same molecular structure as 2-CEES except for the addition of a terminal chlorine atom; therefore, HD and 2-CEES are expected to have similar binding mechanisms and desorption energies. The extra heteroatom may increase desorption energy somewhat due to added surface–adsorbate dispersion interactions, but this will be highly dependent on the geometry of the adsorbed molecules and degree of silica hydroxylation. Notwithstanding, the overall desorption energy for HD from silica is expected to be the same within the limits of experimental accuracy and precision.

Collaborators at ECBC provided data from HD uptake and desorption experiments to allow a more rigorous comparison between HD and 2-CEES. Their results support the hypothesis that

HD and 2-CEES behave similarly on silica. The data from ECBC was obtained with a UHV instrument very similar in design to the chamber described in the experimental section above, but with additional safety measures to work with CWAs.

An IR spectrum of HD after uptake on silica is shown in **Figure 42**. Similar to 2-CEES, HD on silica exhibits two distinct bands in the hydrogen-bonded OH region. The higher-wavenumber band (3620 cm^{-1}) is assigned to the chlorine hydrogen bond and the lower-wavenumber band (3300 cm^{-1}) to the sulfur hydrogen bond. Compared to 2-CEES, the S---HO band is more redshifted (by 70 cm^{-1}) and is broader. Part of this difference may be related to differences in sample preparation. The shoulder in the inverted band for free hydroxyls in the spectrum for adsorbed HD has a significant shoulder, which is evidence that the surface before HD uptake likely had a greater extent of hydroxylation than the surface used for 2-CEES. The Cl---HO bands for adsorbed HD and 2-CEES are centered at the same wavenumber and have similar shapes. Overall, the similarities in these spectra provide evidence that the binding mechanisms for HD and 2-CEES are likely analogous.

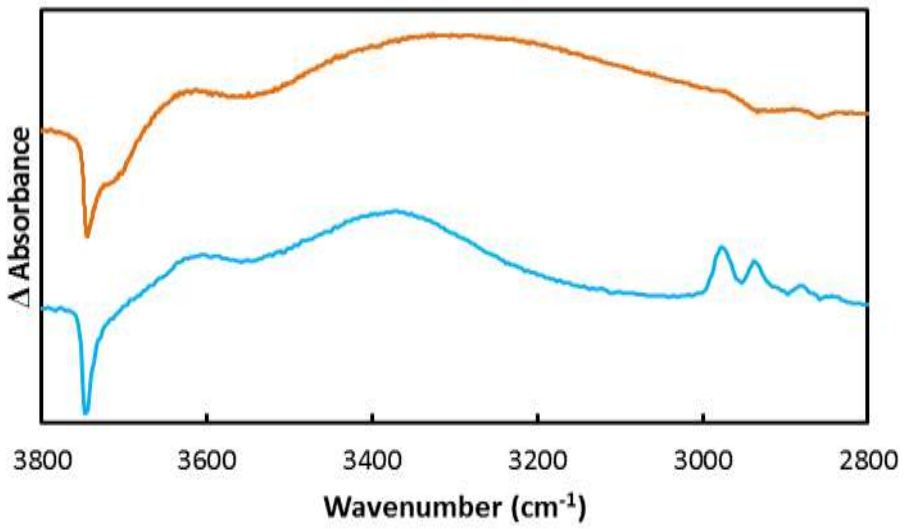

Figure 42. *Infrared spectra of HD on silica collected at ECBC (top, orange) and 2-CEES (bottom, blue) on silica collected at VT*

The TPD results provide further evidence that HD and 2-CEES have similar uptake behaviors on silica. Plots of desorption energy versus coverage for HD measured by collaborators at ECBC, 2-CEES measured at ECBC, and 2-CEES measured at Virginia Tech are shown in **Figure 43**. Two important assumptions were made during the data analysis for this figure. The raw mass spectrometer data from ECBC was not sufficient to determine a prefactor with the inversion analysis method for either 2-CEES or HD. Specifically, only data from two experiments for 2-CEES and two for HD were provided, and a minimum of three experiments is necessary for inversion analysis. Furthermore, the signal-to-noise ratio was poor. Therefore, two assumptions were made during the analysis of the data from ECBC. First, a molecule should have the same desorption energy from silica on any instrument even if the prefactor varies due to differences in the silica sample preparation. Therefore, a prefactor was chosen for the 2-CEES data from data such that it yielded the same desorption energy as the data from VT. Second, the plots of change in mass spectrometer signal as a function of temperature during TPD were similar for HD and 2-CEES. Therefore, the prefactor chosen for the ECBC 2-CEES data was also used to analyze the HD data and produce the values in **Table 9**. With these assumptions, the desorption energies for HD and 2-CEES are indistinguishable.

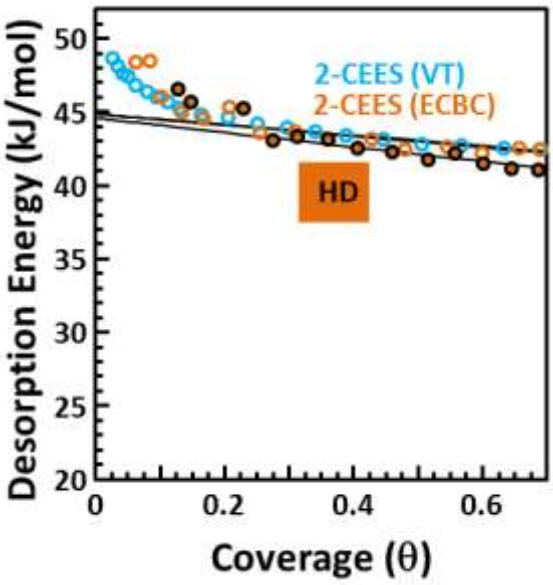

Figure 43. *Activation Energies of desorption for 2-CEES and HD. Blue open circles represents 2-CEES results collected at VT. Orange open circles represent data collected by collaborators at ECBC. Orange and black circles represent HD data collected at ECBC.*

Table 9. *Activation energies of desorption for HD and 2-CEES. Data was collected by researchers at ECBC*

molecule	E_a (± 2.3 kJ/mol)	log(ν) (± 0.6)
2-CEES (VT)	44.9	8.4
2-CEES (ECBC)	44.9	7.3
HD (ECBC)	44.6	7.3

3.4 Summary

We have found that the uptake of 2-CEES on silica is driven primarily by the formation of hydrogen bonds to the thioether and chloro moieties. Although both types of hydrogen bonds have similar overall strength, the contributions to bond strength from other forces, including charge transfer, are apparently different. The S···H–OSi bond has a larger charge transfer contribution, whereas the Cl···H–OSi bond has a larger contribution from other intermolecular forces. Dispersion forces between the hydrocarbon segments of the adsorbed molecules and surface atoms

provide additional stabilization. Each adsorbed 2-CEES molecule occupies a single silanol group, even though the sulfur and chlorine atoms have sufficient spacing to span adjacent silanol groups. The 1:1 bonding motif may be a result of a significant entropic penalty that would be required for dual hydrogen-bond formation. Based on our results and the emerging structure-function relationships that emerged from the above studies, we predict that mustard gas binds to silica through hydrogen bonds and other weak surface-adsorbate interactions that may be as strong as 45 kJ/mol. This result is significant because hydrogen bonding is critical to the environment transport of this highly toxic CWA as it strongly influences uptake prior to subsequent diffusion into the bulk of materials or reaction on the surface of catalytic materials. Our results on silica are particularly relevant because sand is ubiquitous in the environment, and silica is a common component of many artificial materials including polymeric coatings.

3.5 Acknowledgements

We are grateful to the Army Research Office (W911NF-09-1-0150) and the Defense Threat Reduction Agency (W911NF-06-1-0111) for providing support. We thank Advanced Research Computing at Virginia Tech for providing computational resources and technical support that have aided in the research reported in this chapter. We also thank Dr. Frank A. Weinhold for helpful discussions about hydrogen bonding on silica.

Chapter 4: Adsorption of Substituted Benzene Derivatives on Silica: The Effects of Electron Withdrawing and Donating Groups

4.0 Abstract

A fundamental understanding of the forces that drive uptake and binding of aromatic molecules on well-characterized surfaces such as silica is important for predicting the fate of toxic industrial compounds in the environment. Therefore, the adsorption of simple substituted benzene derivatives has been investigated on a hydroxyl-functionalized surface to probe the effects of electron withdrawing and donating functional groups on gas-surface binding. Specifically, this work probes how methyl and halide functional groups affect the properties of the OH--- π hydrogen bond and other surface-adsorbate interactions that play an important role in the uptake of aromatic molecules. Our approach utilizes infrared spectroscopy to study hydrogen-bond formation and temperature–programmed desorption to measure activation energies of desorption. Results from this work indicate that substituted benzene derivatives adsorb to silica via a cooperative effect involving the SiOH---π hydrogen bond and additional substituent-surface interactions that result in unusually high desorption energies.

4.1 Introduction

Hydrogen bonds play a critical role in shaping the natural world. These interactions, though weak compared to typical covalent and ionic bonds, are essential for phenomena such as ligand-receptor binding and protein folding. Hydrogen bonds are also highly relevant to catalysis and other interfacial reactions. In fact, they are often responsible for the initial interaction that binds adsorbate molecules to surfaces before subsequent chemisorption or reaction.[14,44] Thus,

characterization of the factors that influence interfacial hydrogen bond formation is an important step toward understanding general chemistry at the gas-surface interface.

Traditional descriptions of hydrogen bonding often limit hydrogen-bond acceptors to lone pairs on electronegative atoms such as oxygen.[51] However, numerous examples show that any electron-rich region in a molecule may behave as a hydrogen-bond acceptor.[26] Specifically, benzene and other aromatic molecules have been shown to form strong hydrogen bonds with hydroxyl groups, which clearly contrasts with the description of hydrogen bonding as a dipole-dipole interaction.[29–36] The hydrogen bonding character of aromatic-containing compounds arises from an elevated electron density towards the center of the ring, which can interact with hydrogen-bond donors through both charge transfer and electrostatic forces.[37]

The effects of substituents on the distribution of electrons within aromatic molecules have been studied extensively,[52] and those effects likely play a role in molecule-surface hydrogen bonding interactions. Aliphatic hydrocarbon substituents such as methyl groups donate electrons through induction. Although halogens are often treated as purely electron withdrawing groups, they have a more nuanced role in how they affect electron density in aromatic molecules.[53] Halogens indeed draw electron density away from the aromatic rings through inductive effects due to their electronegativity, but, simultaneously, the halogen lone pairs interact with the aromatic π system and add electron density through resonance effects. The inductive effects for halogens tend to dominate the resonance effects to result in a net electron deficiency in the aromatic ring. Research has yet to investigate how the interplay among resonance effects, polarity, and electron density affect aromatic molecule-surface hydrogen bond formation. The work described in this chapter represents the first to use infrared spectroscopy and TPD measurements together to explore how these important factors affect uptake of simple substituted benzene derivatives on silica.

The IR absorption band caused by excitation of the O–H stretching vibration is highly sensitive to hydrogen bonding and is commonly used as a probe of hydrogen-bond properties.[107,109–117] Thus, several studies have used spectroscopic techniques to investigate how substituent-driven changes to the electronic nature of aromatic systems affect the properties of π-hydrogen bonds.[32,34,35,52,118] Beyond simple electrostatics, hydrogen bonds involve partial chemical bonding between a Lewis acid-base pair of the general form X–H---Y that includes a degree of charge transfer from Y to X–H.[25] When the transferred charge populates the antibonding orbital of the donor (as is the case for hydroxyl groups), hydrogen bonding weakens the X–H bond, which produces a characteristic redshift in vibrational frequency. Because the extent of charge transfer depends on the electron density and orbital energy of the hydrogen bond acceptor, Y, the magnitude of the X–H band red-shift depends on the electronic structure of Y and, therefore, substituent effects. Computational and experimental studies of the X–H---π bond for isolated gas-phase compounds demonstrated that electron withdrawing or donating substituents shift the X–H IR band to higher or lower wavenumbers, respectively, relative to the analogous X–H---π bond for benzene.[34,35,119] Previous work on hydroxylated silica surfaces has further explored this relationship by establishing a correlation between the sigma Hammett parameter of substituents (for a variety of small aliphatic molecules) and the vibrational frequency of the SiO–H bond.[33]

Many attempts have been made to indirectly assess the strength of hydrogen bonds, a value that cannot easily be measured directly in many experiments, with spectroscopic measurements of the extent of charge transfer.[39–42] These studies are generally consistent with the so-called "Badger Bauer relationship", which predicts a linear correlation between the shift of the X–H IR band and the strength of the hydrogen bond for similar acceptor-donor pairs (see chapter 1 for a more detailed discussion).[39,42] This correlation has been verified for several systems. For example,

previous work in the Morris group tested the adsorption of a series of organophosphates on partially hydroxylated silica and demonstrated that the activation energies of desorption, which vary from 43 to 58 kJ/mol, correlate linearly with the vibrational energy of the silanol O–H group.[40,41]

Despite demonstrations of a strong correlation between OH vibrational frequency and Y---H–O bond energy, charge transfer is only one of many components of the hydrogen-bond interaction and, therefore, spectroscopic measurements should not always correlate with hydrogen-bond strength. Electrostatics and dispersion forces also contribute significantly to hydrogen bonds.[25,26,34,35,51] In some cases that are consistent with the Badger Bauer relationship, all three components of hydrogen-bond energy likely correlate well with each other as overall hydrogen bond strength changes across a series of molecules. For example, a recent study compared experimental IR spectra to calculations of the electric field along the O–H bond (indicative of the electrostatic contribution to the hydrogen bond) for a series of hydrogen-bonded complexes between benzene derivatives and phenol.[35] That work revealed a linear correlation between the shift of the O–H band and the strength of the electric field. However, other work provides examples where the components of hydrogen bond energy are uncorrelated. For example, as shown in Chapter 3, while two simple molecules like 1-chlorobutane and diethyl sulfide have similar hydrogen-bonding strengths to a hydroxylated silica surface, charge transfer in the Cl---H–O hydrogen bond is significantly smaller than in the S---H–O hydrogen bond.[79]

For systems where the hydrogen bond donor is part of an extended surface, contributions to the desorption energy from dispersion interactions between the adsorbate and surrounding substrate also play a role in the overall interaction. These interactions have been examined in experiments (described in Chapter 3) that compared the desorption energies and IR spectra of a

series of linear chloroalkanes from amorphous silica. In that work, the activation energy of desorption was found to increase with chain length, but the redshift of the O–H stretch involved in the $CH_3(CH_2)_nCl$---H–OSi hydrogen bonds was shown to be nearly independent of chain length. Therefore, the observed increase in the desorption energy with chain length was attributed to dispersion interactions with hydrophobic regions of the silica surface. In fact, the experiments determined that each methylene unit provided an additional ~ 5 kJ/mol to the overall interaction.

The magnitude of dispersion forces is likely different for substituted benzene derivatives at surfaces than for chloroalkanes, but they may also contribute significantly to the activation energy of desorption (E_a). Previous studies into the adsorption of substituted benzene derivatives on titania probed the influence of substituent-surface interactions.[32] Although binding energies were not directly measured in that work, the surface residence time was significantly higher for aryl halides than for benzene, even though the OH---π interaction for benzene was reported to be stronger.[32]

Quantitative measurements of how substituents affect the π-hydrogen bonds that drive surface adsorption of aromatic molecules have not been reported in the literature. The work presented here explores how functional groups on a substituted benzene molecule affect not only the SiO–H---π hydrogen bond strength, but also the overall desorption energy. We have used IR spectroscopy to analyze changes in surface vibrational motions in silica caused by adsorbed molecules and thus probe the extent of charge transfer between the hydrogen bond donor and acceptor. We have also performed a series of temperature programmed desorption (TPD) studies to determine the activation energy required to overcome the surface-adsorbate interactions and drive the adsorbed molecules from the surface. These two techniques have provided insight into

the relative importance of the forces that lead to the uptake of simple substituted benzene derivatives onto a hydrogen-bonding surface.

4.2 Experimental

4.2.1 Preparation of silica

Details about the instruments and experimental procedures used for this project are described in Chapter 2. All experiments were conducted in an ultra-high vacuum (UHV) chamber at a base pressure of 10^{-9} Torr to minimize contamination on the silica surface and to reduce interference from atmospheric gasses on IR and mass spectrometer measurements. To prepare the sample, particulate silica (Aerosil) was pressed into a Tungsten mesh, which was subsequently mounted on an X–Y–Z manipulator to allow precise and reproducible adjustments of sample position in the chamber. The sample was resistively heated with a custom-built power supply and cooled with liquid nitrogen in direct thermal contact with the sample mount. Copper leads from the external power supply and type-K thermocouple wires to monitor sample temperature were attached to the mesh via a UHV-rated ceramic feedthrough. The surface was heated to 700 K immediately before each experiment to drive off any residual contamination from prior experiments. This pretreatment step also removed a large fraction of the silanol groups normally present on silica under ambient conditions. As described in Chapter 2, Uglienko et al. used B3LYP computations to simulate IR spectra of silica at different degrees of hydroxylation. Our IR spectra obtained after heating, in comparison to these theoretical spectra and other work, indicated that the surface was dominated by isolated silanol groups at a density of 2 OH/nm^2.[15,86–89,95] Ugilengo

4.2.2 Dosing

All chemicals used (IUPAC names and molecular structures are listed in **Figure 44**) were purchased from Sigma Aldrich and purified with three freeze-pump-thaw cycles immediately before use. The silica sample was cooled to below 190 K before dosing to maximize uptake during a short (3-7 minute) period of exposure to the molecule under investigation. A custom manifold and capillary array doser, both of which have been previously described in detail,[40,41,79] were used to expose the silica sample to vapors of each adsorbate under UHV conditions. Changes in the surface vibrational modes of silica before, during, and after dosing were monitored with a Nicolet Nexus 670 infrared spectrometer set to record 128 scans at 4 cm^{-1} resolution. IR spectra were also used to identify and characterize molecules adsorbed to the surface.

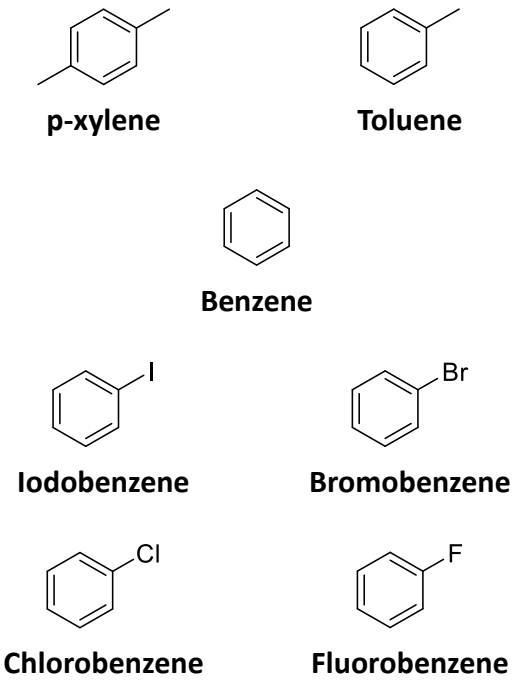

Figure 44. *Schematics for benzene and functionalized aromatic molecules explored in this work*

4.2.3 Annealing

The sample was heated to 10-20 K above the dosing temperature for 2-3 minutes immediately after the dosing procedure to achieve an even distribution of molecules throughout the bed of pressed silica particles. This is a necessary requirement for TPD measurements from highly porous materials.[95] The maximum temperature and duration of the heating process were varied as a convenient and reproducible method to adjust the amount of adsorbate on the surface. Sufficient heating was verified by observing the trailing edges of TPD curves at different surface coverages. Good alignment indicated that the adsorbed molecules were well-distributed throughout the sample.[95] The sample was cooled to at least 10 K below the dosing temperature before the start of the TPD experiment to ensure that the desorption rate was near zero at the beginning of the experiment.

4.2.4 TPD

TPD data were obtained by heating the sample at a linear rate of 0.2 K/s with a proportional-integral-derivative controller and detecting desorbed species in an axially mounted, doubly differentially pumped mass spectrometer (Extrel) tuned to the most abundant mass fragments for that molecule. Apertures restricted the view from the mass spectrometer to a 0.35-cm^2 spot on the surface and ±0.4° acceptance angle to minimize signal caused by molecules that desorbed from the sample holder. Our procedure for TPD data analysis with the inverted Polanyi Wigner equation (**eq 4.1**) and an experimentally determined preexponential factor (ν) are described in Chapter 2. In brief, data from the mass spectrometer were used to determine desorption rate as a function of temperature for several experiments with varying initial fractions of occupied silanol adsorption sites (θ). **Figure 45** shows plots of the desorption rate of benzene

versus temperature for three initial coverages. An initial guess for ν was used to calculate desorption energy as a function of θ for the run with the highest initial θ. These data were then used to simulate the temperature-dependent desorption rate for all of the measurements conducted with lower initial values of θ. The same process was repeated for a range of preexponential factors to minimize the difference between experimental and simulated data. The reported results are activation energies of desorption as a function of θ.

$$E_a(\Theta) = -k_B T_S ln\left(-\frac{d\Theta/dt}{\upsilon\Theta}\right) \quad \textbf{(4.1)}$$

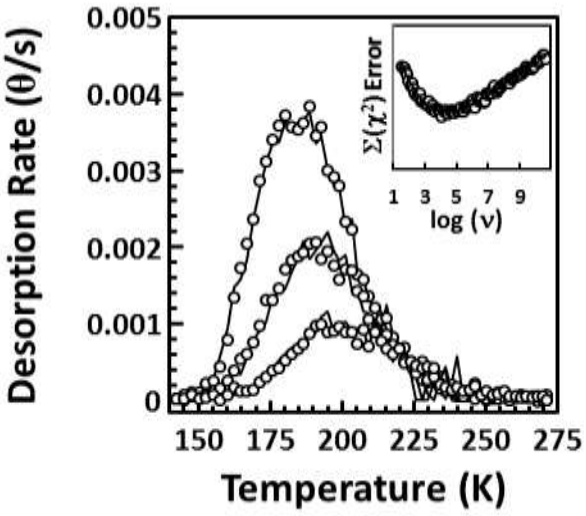

Figure 45. *Experimental (circles) and simulated (lines) TPD curves for benzene at different coverages. From top to bottom: θ = 0.80, 0.55, 0.30. The inset shows a 6th-order polynomial fit to χ2 error values (in units of θ^2/s^2) between simulated and experimental data used to determine the best prefactor value.*

4.3 Results

4.3.1 IR characterization of adsorption

Evidence that benzene uptake is driven by the formation of SiO–H---π hydrogen bonds on silica is provided in **Figure 46.**, which shows the infrared spectrum of a silica surface following

exposure to benzene along with a spectrum of gas-phase benzene. The IR bands assigned to the C–H and C–C vibrations are similar in relative intensities for the gas-phase and adsorbed spectra, which indicates molecular adsorption of benzene. The narrow C–C and C–H bandwidths in the spectrum of adsorbed benzene compared to the spectrum of gas-phase benzene are due primarily to the absence of rotational transitions for adsorbed species. Although the spectra are similar, adsorption does cause a slight red shift in the C–H and C–C vibrational energies, as is expected for a hydrogen-bonded aromatic ring.[30] The narrow IR band at 3748 cm^{-1}, assigned to the SiO–H stretch in free surface silanol groups, decreases with benzene uptake as a broad IR feature emerges at 3605 cm^{-1}, which is the expected region for the SiO–H stretch associated with the SiO–H---π hydrogen bond.[36] Previous work has indicated that charge transfer is likely a dominant factor responsible for the vibrational energy change of hydrogen-bonded silanol groups.[17,18,25] The antibonding orbital of the SiO–H bond receives electron density from the hydrogen bond acceptor (π electrons in this case), which causes the vibrational energy of the bond to decrease.

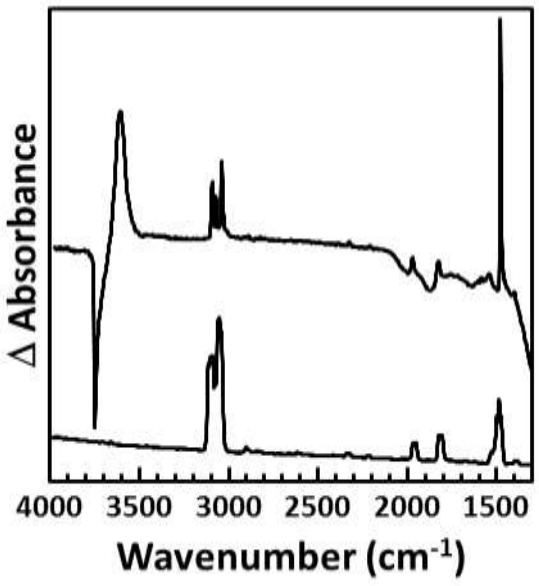

Figure 46. *Infrared spectra of gas-phase benzene (lower spectrum) and adsorbed benzene on silica (upper spectrum).*

The effect of substituents on the IR spectra for a series of adsorbed benzene derivatives is evident by the data shown in **Figure 47**. As is the case for benzene, the integrated areas of C–C and C–H spectral bands for these surface-bound molecules red-shift slightly upon adsorption compared to the same bands in gas-phase spectra..[120] The silanol region shows evidence of SiO–H---π hydrogen bonding similar to benzene. However, the extent of redshift caused by hydrogen bonding is different for each molecule. The wavenumbers of the $\nu(OH)_{adsorbed}$ vibrations are provided in **Table 10**. In agreement with other published work[34,35] the shift is greater than benzene for the methyl-substituted aromatics and less than benzene for the halogenated aromatics.

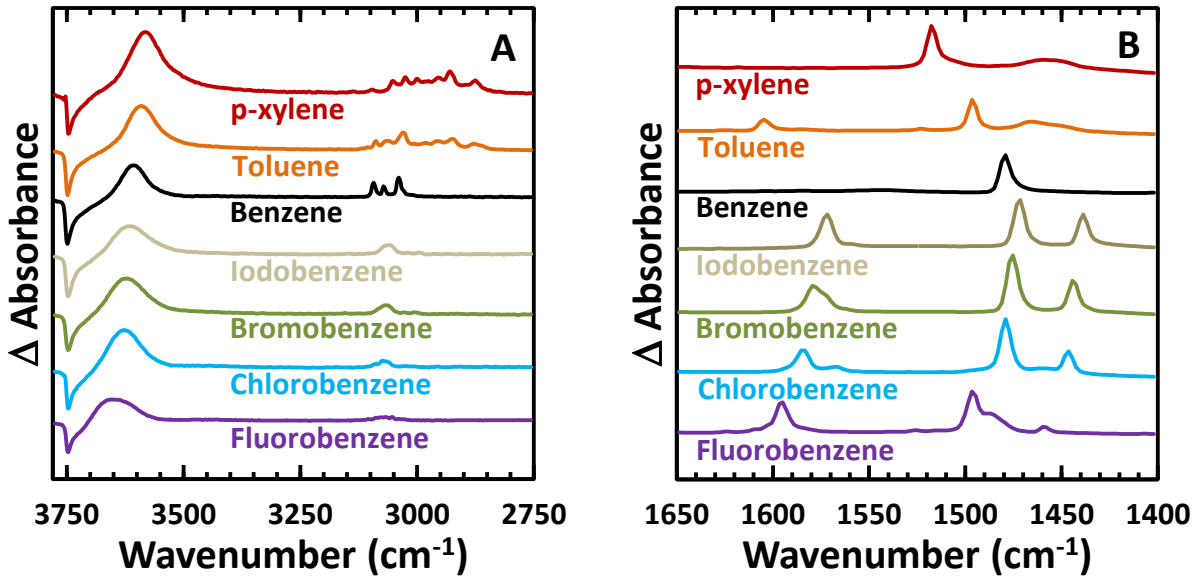

Figure 47. *Infrared spectra of adsorbed benzene and benzene derivatives on silica. The spectra are normalized to the integrated area of the free OH band such that they represent equivalent*

effective SiOH occupation fractions, θ (see text). (A) shows the SiO–H and C–H stretching bands. (B) shows the aromatic C–C bands.

Table 10. *Desorption energies, pre exponential factors, and ν(OH) values for all molecules tested in this study. Error values are ± one standard deviation calculated from three separate TPD experiments.*

molecule	E_a (± 2.3 kJ/mol)	log(ν) (± 0.6)	ν(OH) (± 2 cm^{-1})
p-xylene	44.9	8.4	3581
Toluene	41.8	8.6	3590
Benzene	31.0	6.0	3604
Iodobenzene	47.2	8.4	3615
Bromobenzene	45.8	8.3	3619
Chlorobenzene	42.5	8.5	3627
Fluorobenzene	33.6	7.1	3654

4.3.2 Activation energy for desorption

The experimentally determined activation energy for desorption, E_a, reveals a strong substituent effect on the overall binding energy (see **Figure 48**). The upward curvature of the data in **Figure 48** at lower coverages is largely due to the inhomogeneous nature of the silica surface.[40,41,79] For the current study, we report E_a in the limit of zero coverage for each adsorbate. To obtain these values, each E_a curve was fitted to the function expressed in **eq 4.4** where A_0, λ, and m are fitting parameters. The intercept of the linear component of **eq 4.4** represents the activation energy for desorption at zero coverage (E_a).

$$E_{fit}(\theta) = A_0 e^{-\theta\lambda} + m\theta + E_a \qquad \textbf{(4.4)}$$

4.4 Discussion

We have explored the forces that drive hydrogen-bond formation at the gas-surface interface between partially hydroxylated silica and a series of functionalized aromatic molecules to better understand how substituent effects influence uptake on hydroxyl-containing surfaces. As

described in Chapter 2, IR spectroscopy was used to probe the extent of charge transfer in SiO–H---π hydrogen bonds. The activation energies for desorption were determined via TPD measurements, which provide insight into the overall strength of the interactions between adsorbed aromatic molecules and silica. Together, these techniques reveal how the uptake of aromatic molecules on polar surfaces is affected by the electron withdrawing or donating nature of substituents and how substituent-surface interactions affect adsorption.

4.4.1 Substituent effects on the SiO–H---π bond

Although benzene is a non-polar molecule with a high degree of molecular symmetry and low miscibility with water, the molecule behaves as a hydrogen bond acceptor when paired with hydroxyl groups.[37] In contrast to common descriptions of hydrogen bonding, which depict an electrostatic attraction between a hydroxyl group and a relatively electronegative acceptor atom such as oxygen or nitrogen,[51] the O–H---benzene bond is an interaction between the hydroxyl proton and the delocalized aromatic π electrons. Many research groups have explored how substituents affect the distribution of electron density in benzene derivatives, and several have specifically investigated how substituent effects enhance or weaken hydrogen-bond strength.[32,34,35,119] It is well established that substituents attached to an aromatic ring change the electron density within the conjugated π system through resonance and induction.[52,53] For example, halogen substituents increase electron density through resonance as the lone pairs conjugate with the aromatic ring; however, they also have the effect of removing electron density through induction due to their electronegativity. The inductive effect tends to be stronger than the resonance effect, and therefore halogens are typically treated as electron-withdrawing substituents.[53] In contrast to halogens, methyl groups and other aliphatic substituents tend to

increase electron density within the aromatic ring to which they are bound. Previous condensed- and gas-phase studies have provided important insight into how these substituent-driven electron density effects influence hydrogen-bonding behavior when an aromatic ring acts as a hydrogen-bond acceptor.[29,34,35,118,119]

At the gas-surface interface, others in the Morris group have shown a correlation between the sigma Hammett parameter of substituents (values that relate the electronic nature of substituents on benzoic acid derivatives to equilibrium and rate constants) and the vibrational frequency of the SiO–H bond for a variety of small aromatic molecules.[83] For the substituted aromatic molecules reported here, we have observed a similar trend for the adsorption of benzene derivatives on silica with electron withdrawing substituents (fluorobenzene, chlorobenzene, dichlorobenzene, bromobenzene, and iodobenzene) and electron donating substituents (toluene and p-xylene). Specifically, the presence of methyl substituents increases the electron density within the aromatic ring (relative to benzene), which provides additional charge for transfer to the surface OH groups. The more prominent charge transfer component to the SiO–H---π hydrogen bond is reflected in a greater red-shift of the surface OH vibrational mode as the charge populates the OH σ^* orbital, thereby weakening this bond (see **Figure 47** and **Table 10**). Conversely, the presence of increasingly electronegative halogen substituents decreases the charge transfer component of hydrogen bonding, which results in a progressively smaller redshift of the OH band as the electronegativity of the substituents increases.

4.4.2 Correlation between desorption energy and charge transfer

Discussions about spectroscopic analysis of hydrogen-bond strength often reference the Badger-Bauer relationship, described in Chapter 1, which predicts a linear correlation between

wavenumber shift of the O–H band due to hydrogen bonding (i.e. the extent of charge transfer that takes place between hydrogen bond acceptor and donor) and the strength of the hydrogen bond for a series of similar molecules. Previous work has shown that this relationship can be applied to a wide variety of systems, including the O–H---π hydrogen bond.[39–42,103] However, as shown by our results, spectroscopic data alone is not an appropriate predictor of the overall binding energy between substances that form a hydrogen bond, particularly in systems that include extended surfaces where dispersion forces play a significant role in the total interaction energy.[79,121]

Deviations from the Badger-Bauer correlation are expected when charge transfer, which is responsible for the redshift in the OH hydrogen–bond acceptor, is only a small component of the bond energy.[29,79] As emphasized in a recently proposed revision to the IUPAC definition for the hydrogen bond,[26] electrostatics, specifically attractive Coulombic forces between dipoles, and dispersion forces are two critically important interactions that can contribute significantly to the O–H---π hydrogen bond energy.[29,35] Such effects appear to play a major role in gas-surface hydrogen bond formation. For example, the study described in Chapter 3 compared the behavior of linear thioethers and chloroalkanes on surfaces to discover that the extent of charge transfer was significantly larger for diethyl sulfide than for 1-chlorobutane, even though the activation energies for desorption of both molecules were nearly identical. The key results from that study demonstrated that the weaker charge transfer component observed for 1-chlorobutane binding was balanced by stronger electrostatic and dispersion components compared to diethyl sulfide binding.

The interplay between electrostatics, dispersion, and charge transfer is affected by the distance between the donor hydrogen atom and the moiety that accepts the hydrogen-bond.[25,34,35] Specifically, the extent of charge transfer within a hydrogen bond decreases quickly with the distance between the hydrogen bond donor and acceptor; therefore charge transfer is expected to

play a small role in relatively long hydrogen bonds. The SiO–H---π hydrogen bond investigated in this work is such an example of a relatively long hydrogen bond.

The length and charge transfer characteristics of the hydrogen bonds involved in this work have been investigated computationally. Specifically, geometry optimizations were performed at the MP2/cc-pVTZ level of theory with the Gaussian09 suite of programs[122] for a gas-phase silanol–benzene hydrogen bond (H_3SiO–H---benzene). The calculated hydrogen bond distance is 2.39 Å (2.48 Å when the calculations are corrected by the basis-set superposition error, BSSE) between the H atom of the silanol and the closest atom of the benzene molecule.[123] In contrast, a similar interaction complex between gas-phase silanol and the archetypical hydrogen bond acceptor, NH_3, (optimized at the same level of theory) exhibits a distance of 1.85 Å (1.90 Å with BSSE correction).[123] These results strongly suggest that the amount of charge transfer, and hence the red shift of the SiO–H stretch, in the hydrogen bond between silanol and benzene is significantly smaller than the prototypical hydrogen bond between silanol and NH_3. In agreement with this expectation, the calculated O–H red shift for the silanol---NH_3 complex is 240 cm^{-1}, but that between silanol and benzene is only 100 cm^{-1}.

To further solidify the connection between the charge-transfer component of the hydrogen bond and the red-shift of the O−H stretch, natural bond order analysis[124] was employed to compute the electronic density in the antibonding orbital of the O–H bond for both the silanol---NH_3 and silanol---benzene dimers. At the MP2/cc-pVTZ level, the population of the OH σ* orbital is only 0.0095 e in the silanol---benzene pair, compared to 0.0344 e for silanol---NH_3. The large computed differences in the OH σ* orbital populations for the two electron donors corroborates the direct relationship between charge transfer and the red shift of the vibration frequency of the donor O−H bond. Moreover, the smaller charge transfer component in the silanol---benzene system also helps

account for the relatively small red-shift observed for the SiO−H vibrational frequency for all of the aromatic compounds studied here relative to red-shifts reported in other work.[40,41,79,107]

Despite the small charge transfer component to the adsorption energy, the aromatic compounds exhibit significant desorption energies, reaching over 45 kJ/mol for iodobenzene. The high energies for desorption likely have a large contribution from dispersion forces, which we find play a significant role in the adsorption of polarizable substituents on extended molecular surfaces. For instance, in a recent study of hydrogen bonding between linear chloroalkanes and hydroxyl groups at the surface of silica, the activation energy of desorption was found to increase almost linearly with chain length.[79] However, the redshift of the O–H stretch involved in the $CH_3(CH_2)_nCl$---H–OSi hydrogen bonds was nearly unaffected by chain length. Therefore, the observed increase in the desorption energy with chain length was attributed to dispersion interactions (totaling about 5 kJ/mol per methylene unit) with the silica surface.[79]

Deviations from the Badger Bauer correlation can therefore generally be explained by the fact that the hydrogen bond may be influenced by factors such as distance that affect the extent of charge transfer independently from dispersion or electrostatic forces. For surfaces, we further note that dispersion forces between the surface and non-hydrogen-bonding moieties in adsorbed molecules also influence the overall adsorption energy independently of hydrogen bond energy. The latter effect is of particular importance in the present work because of the differences in polarizability between methyl and halogen substituents. As described in the Results section of this chapter, we have performed TPD experiments to determine activation energies for desorption of the aromatic molecules from silica and thus examine how substituents affect the total interaction energy.

The TPD measurements shown in **Figure 48** provide an indication of the total molecule-surface binding strength and, along with the infrared spectra of **Figure 47**, yield direct insight into the relationship between the extent of charge transfer and overall adsorption energy. Previous studies that show excellent agreement between computationally determined bond energies and experimentally measured desorption energies (via TPD) show that the measured E_a for desorption (for the systems presented here) is strongly correlated to the molecule-surface bond energy.[40,41,79] The activation energies for desorption, as determined from the TPD data, are plotted against the O–H vibrational wavenumber in **Figure 49**.

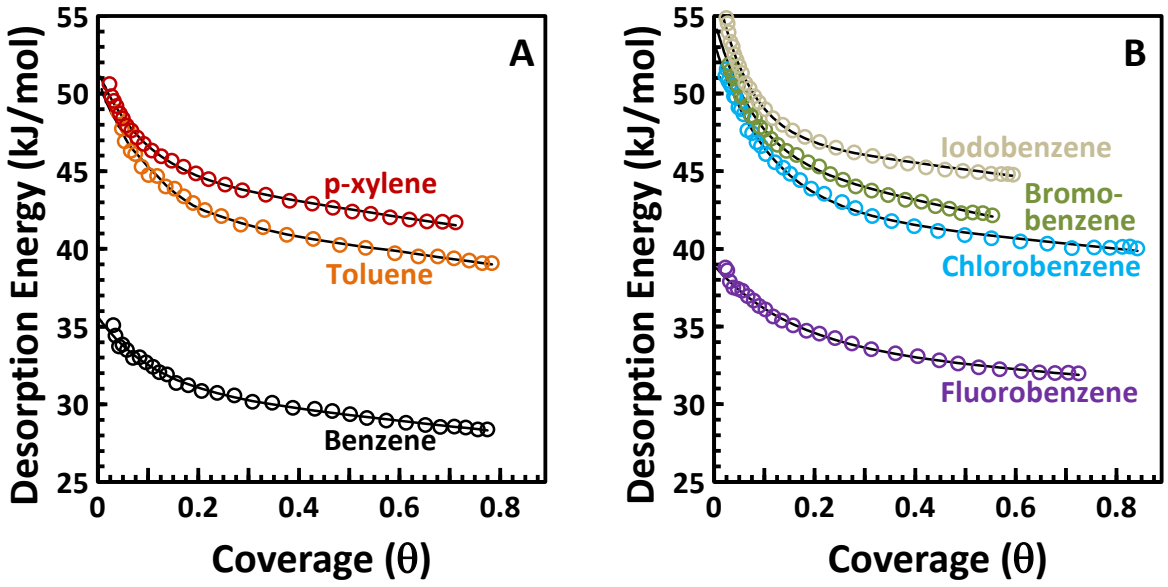

Figure 48. *(A) $E_a(\theta)$ curves for the desorption of benzene, toluene, and p-xylene from partially hydroxylated silica. (B) $E_a(\theta)$ curves for the desorption of chlorobenzene and fluorobenzene from*

partially hydroxylated silica. Open circles are experimental data. Black lines are regression curves generated from ***eq 4.2***

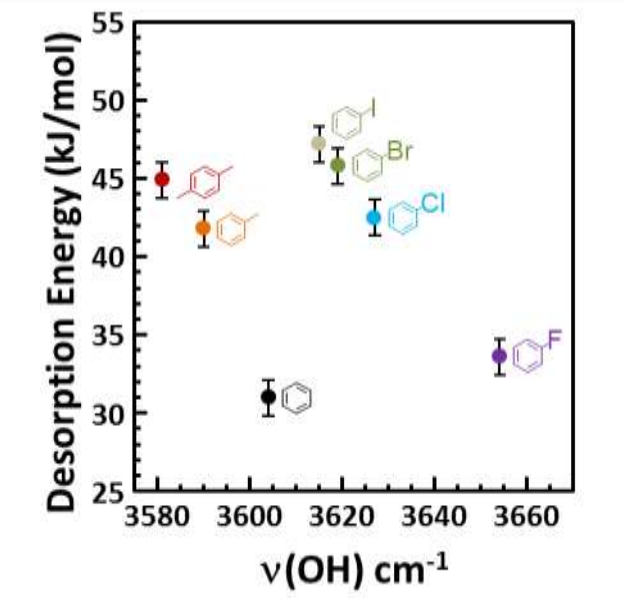

Figure 49. *Plot of ν(OH) versus E_a for benzene and several substituted benzene derivatives. Error values are ± one standard deviation calculated from three separate TPD experiments*

The adsorbate-surface interactions measured here for aromatic molecules are somewhat weaker than several other classes of molecules (carbonyl, thioether, and phosphoryl) measured by the same methods,[40,41,79] which is consistent with the MP2/cc-pVTZ calculation (vide supra) that suggests a relatively long silanol benzene hydrogen bond. However, we note that our experimental results for the desorption energy of benzene are nearly more than 10 kJ/mol lower than previous calculations of benzene adsorption on a hydroxylated silica surface.[125] The source of this variation may lie in differences between the model surface used in the calculations and the aerosil surface employed here. Differences in surface geometry could have a significant effect on E_a for desorption due to the major role played by dispersion forces.

As shown in **Figure 49**, the activation energies for desorption of the aromatic compounds explored in this work fall into one of two categories when plotted against the hydrogen-bonded SiO–H vibrational wavenumbers. We find that the desorption energies are strongly correlated with the red shifts of the O–H vibrational modes for benzene, toluene, and p-xylene. Likewise, the TPD and spectroscopic data are linearly correlated for the aryl halides. Although the slopes for the trends are similar, the Badger–Bauer relationship is discontinuous across this set of seven compounds. That is, although the extent of charge transfer into the SiO–H σ^* orbital is lower for the aryl halides, the desorption energies are offset from the trend formed by the methyl-substituted benzene derivatives by more than 20 kJ/mol.

Within each category, the trend agrees with what one would expect based on how inductive and resonant substituent effects influence the extent of charge transfer and hydrogen bond energies. Specifically, one would hypothesize that as electron density within the aromatic ring of benzene increases, as consequence of methyl substitution, the hydrogen bonding energy should increase because charge transfer, dispersion, and electrostatic contributions to the hydrogen bond increase. Conversely, as the electron density decreases upon replacing the iodo group with more electron withdrawing halogens (Br, Cl, and F) the strength of the hydrogen-bonding interaction should decrease.

The discontinuity in the trend between the desorption energy for benzene and iodobenzene is most likely a consequence of forces that extend beyond the local SiO–H--- π hydrogen bond. We hypothesize that the aryl halides exhibit much larger desorption energies than one would expect based on the electron density within the aromatic ring (and several previously reported gas-phase studies)[22,30–32,99] because the functional groups interact with the surface through dispersion, which significantly strengthens the molecule-surface attraction.[31,119,126] Previous work suggests

that aryl halides attached to a hydrogen-bonding surface by an O–H---π interaction can receive additional stabilization from halogen-surface interactions.[32,127,128] Of particular relevance, chlorobenzene was shown to bind more strongly to a highly hydroxylated TiO_2 surface than benzene, despite indirect evidence that the O–H---π interaction was stronger for benzene. This increased binding energy was attributed to the presence of interactions between the chlorine moiety and the surface. The exact strengths of the halogen-surface interactions have not been determined in our work. However, given the abundance of electron lone pairs around halide groups, it is not unreasonable to attribute a large portion of the 16 kJ/mol energy difference between iodobenzene and benzene to dispersion forces. Therefore, estimates of the total gas-surface adsorption energy, which ultimately governs the uptake and residence time of aromatic containing compounds on surfaces, must include contributions from both O–H---π type hydrogen bonding and dispersion interactions with regions of the surface remote from the site of the hydrogen bond.

4.5 Summary

We have found that the uptake of benzene and substituted benzene derivatives on silica is driven by a combination of SiO–H---π hydrogen bonds and surface-substituent dispersion forces. The extent of charge transfer in the hydrogen bond correlates well with the electron donating and withdrawing nature of the substituents. Furthermore, the extent of charge transfer correlates well with E_a for aromatic molecules with similar substituents. Although the SiO–H---π bonds for the aryl halides appear to be weaker than for benzene, we hypothesize that the E_a values are high largely due to interactions between the electron-rich halogen atoms and the surface. The activation energies for desorption for benzene, toluene, and p-xylene increase from 31.0 to 44.9 kJ/mol across this series. The activation energies for desorption of the aryl halides increase from 33.6 to 47.2

kJ/mol in the order fluoro-, chloro-, bromo-, and iodobenzene. These two trends are offset from each other by dispersion forces, which are significantly stronger for halogen-substituted benzene derivatives than methyl-substituted benzene derivatives.

4.6 Acknowledgements

This material is based upon work supported in part by the U. S. Army Research Laboratory and the U. S. Army Research Office under grant number W911NF-14-1-0159. The authors acknowledge Advanced Research Computing at Virginia Tech for providing computational resources and technical support that have contributed to the results reported within this paper (URL: http://www.arc.vt.edu).

Chapter 5: Uptake, Binding, and Energetics of the CWA Simulant Methyl Salicylate on Amorphous Silica

5.0 Prologue

The previous two chapters discussed fundamental studies into the hydrogen-bonding mechanisms and energetics for simple organic compounds, including CWAs and toxic environmental pollutants, on particulate silica. The methods developed for the work described in those chapters were employed in other projects to explore the nature of hydrogen bonding of more complex multifunctional organic species on silica. For example, methyl salicylate, a common CWA simulant, has aromatic, hydroxyl, and ester functional groups, each of which may play a role in hydrogen bond formation at surfaces. This chapter will discuss our current best knowledge about the adsorption mechanisms and binding energies of methyl salicylate and related aromatic molecules. Although the uptake mechanism for methyl salicylate was not fully characterized in this work, much was learned about the forces involved in its uptake that will be of use in future investigations of this system.

5.1 Introduction

The surface chemistry of methyl salicylate on hydrogen bonding materials is important for addressing health and environmental risks posed by CWAs and toxic industrial compounds (TICs). The relevance to CWA research arises from the common use of methyl salicylate as a simulant for mustard gas (HD), especially in military field tests that involve real equipment or soldiers. The toxicity of methyl salicylate is much lower than 2-CEES, another important HD simulant (see Chapter 2). In fact, methyl salicylate is used in low concentrations as a wintergreen flavoring in food and in higher concentrations as an additive in skin balms for muscle or joint pain relief. More

importantly for its use as a simulant, methyl salicylate has a few similar physical properties to HD. Molecular weight, water solubility, and vapor pressure are similar for HD and methyl salicylate as shown in Chapter 1. Research has shown that fabric and dermal penetration behavior are also similar.[10]

Although the use of methyl salicylate as a substitute for HD can easily be justified to study processes strongly influenced by bulk thermodynamic properties such as evaporation and penetration, little is known about the hydrogen bonding of methyl salicylate on surfaces and whether the molecule-surface attractive forces are similar to those of CWAs. Methyl salicylate has almost nothing in common structurally with HD. The aromatic ring and polar oxygen-containing functional groups associated with methyl salicylate may have a significant effect on the characteristic of binding at surfaces. Therefore, we initiated a study to measure and compare the binding energies and mechanisms of methyl salicylate, 2-CEES, and HD on a partially dehydroxylated silica surface.

A major goal of our work was to learn about the molecular geometry of adsorbed methyl salicylate on an environmentally relevant, hydrogen-bonding surface. As described throughout this thesis silica is one of the most abundant materials on earth and presents hydrogen-bond donor groups (SiOH) to incoming gases that may serve as docking points for polar compounds. Uptake on hydroxylated silica is primarily driven by hydrogen bonds and dispersion forces. Methyl salicylate has three oxygen atoms (carbonyl, ether, and hydroxyl) and an aromatic ring. All of these species are potential hydrogen bond acceptors. Also, the hydrogen atom in the hydroxyl group is a potential hydrogen bond donor. We sought to determine the role each hydrogen-bond donor and acceptor functional group in methyl salicylate plays in uptake. To this end, we systematically studied a selection of structurally simpler molecules with aromatic, carbonyl, and

hydroxyl moieties in order to better understand the behavior of each one. The table of physical and chemical properties for the compounds employed in the work described below is reproduced here for reference (**Table 11**), and molecular structures are provided in **Figure 50**. All of these molecules are used in industrial processes, thus the results in this chapter provide direct insight into to environmental fate of toxic industrial compounds (TICs) and other pollutants. The experiments described below used TPD to measure activation energies of desorption. IR spectroscopy was used to identify changes in the vibrational frequencies of the surface and simulant molecules during uptake and desorption in order to determine the binding mechanism.

Table 11. *Physical and chemical properties for the compounds employed in this work.*[48,50] *The missing values could not be found from any reliable source.*

molecule	dipole (D)	volume (cubic angstroms)	polarizability (cm^3)	vapor pressure at 298 K (kPa)	density of neat liquid (g/mL)	mass (g/mol)	boiling point (K)	melting point (K)
Methyl salicylate	2.2	137		0.00457	1.17	152	495	264
Methyl 2-methyl benzoate		145			1.07	150	480	
Benzaldehyde		103	12.8	0.133	1.04	106	451	216
m-cresol	1.6	109	13.05	0.0147	1.03	108	475	285
Acetone	2.9	65	6.27	30.6	0.78	58	329	179
Benzene	0.0	78	9.95	12.7	0.88	78	353	279

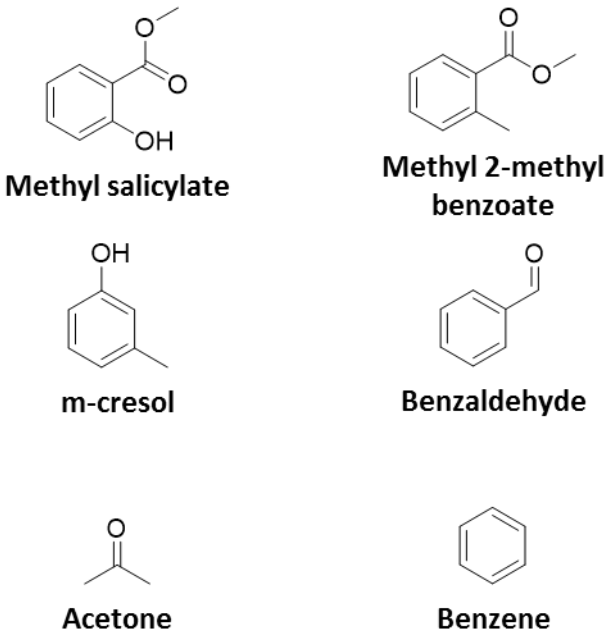

Figure 50. *Schematics for benzene and functionalized aromatic molecules explored in this work*

5.2 Experimental

5.2.1 Preparation of silica

Details about the instruments and experimental procedures used for this project are presented in Chapter 2. Experiments were conducted in an ultra-high vacuum (UHV) chamber at a base pressure of 10^{-9} torr to minimize contamination on the silica surface and to avoid interference from atmospheric gasses on IR and mass spectrometer measurements. To prepare the sample, particulate silica (Aerosil) was pressed into a Tungsten mesh mounted on a X–Y–Z manipulator, which allowed us to precisely and reproducibly adjust the position of the sample in the chamber. The sample was resistively heated with current from a power supply and cooled with liquid nitrogen in direct thermal contact with the sample mount. The surface was heated to 700 K as needed to remove residual contamination from prior experiments. This pretreatment step also partially dehydroxylated the silica sample. IR spectra obtained after heating indicated that the

surface was dominated by isolated silanol groups at a density of about 2 OH/nm^2 (see Chapter 2).[86–89,95]

5.2.2 Dosing

All chemicals used (IUPAC names and molecular structures are listed in **Figure 50**) were purchased from Sigma Aldrich and purified with at least two freeze-pump-thaw cycles immediately before use. The silica sample was cooled to below 220 K before dosing to maximize uptake during a short (3-7 minute) period of exposure to the molecule under investigation. Specific dosing conditions are listed in **Table 12**. The custom manifold and capillary array doser described in Chapter 2 were used to expose the silica sample to vapors of each adsorbate under UHV conditions. Changes in the surface vibrational modes of silica before, during, and after dosing were monitored with a Nicolet Nexus 670 infrared spectrometer set to record 128 scans at 4 cm^{-1} resolution. IR spectra were also used to identify and characterize molecules adsorbed to the surface. Gas-phase spectra for each molecule included in this study were collected in an improvised sealed gas cell with KBr windows on either side. The cell was placed in an IR spectrometer, purged with dry nitrogen, and filled with the gas of interest. These gas-phase spectra used a scan of the nitrogen-filled cell as a reference background.

Table 12. *Experimental conditions for all molecules included in this chapter*

Molecule	Dosing temperature (K)	Dosing duration (minutes)	Anneal temperature (K)
Methyl salicylate	223	3.0-10.5	221-273
Methyl 2-methyl benzoate	223	5.5	255-273
Benzaldehyde	223	5	255-269
m-cresol	223	5.5	255-273
Acetone	223	5	255-263
Benzene	173-223	3.5-5.0	N/A

5.2.3 Annealing

The sample was heated at a rate of 0.2 K/s to a target temperature immediately after the dosing procedure in most experiments to achieve an even distribution of molecules throughout the bed of pressed silica particles. As described in Chapter 2, this step is a necessary requirement for TPD measurements from highly porous materials.[95] The maximum temperature and duration the sample was held at that temperature was varied as a convenient and reproducible method to adjust the amount of adsorbate on the surface. This step was omitted for benzene, which was the most weakly bound molecule in this study, to minimize loss on the surface before commencing the TPD ramp. Anneal temperatures are listed in **Table 12**. Sufficient heating was verified by observing the trailing edges of TPD curves at different surface coverages. Good alignment indicated that the adsorbed molecules were well-distributed throughout the sample.[95] The decision to not heat benzene was validated by confirming that the trailing edges lined up well. The sample was cooled to at least 10 K below the dosing temperature before the start of the TPD experiment to ensure that the desorption rate was essentially zero at the beginning of the experiment.

5.2.4 TPD

TPD data was obtained by heating the sample at a linear rate of 0.2 K/s with a proportional-integral-derivative controller and detecting desorbed species in an axially mounted, doubly differentially pumped mass spectrometer (Extrel) mounted in direct line-of-sight of the sample and tuned to the most abundant mass fragments for that molecule. Apertures restricted the view from the mass spectrometer to a 0.35-cm^2 spot on the surface and a ±0.4° acceptance angle to minimize signal caused by molecules that desorbed from the sample holder. Several of the methyl salicylate experimental runs displayed a significant high-temperature feature in the TPD distribution at about

325 K. The shape of this feature, specifically the rapid decrease in signal, was evidence of zero order desorption, which in turn was indicative of sublimation of molecules that were not hydrogen-bonded to silica. Furthermore, infrared spectra collected during the heating ramp indicated that the majority of adsorbed methyl salicylate molecules desorbed well below 325 K. Therefore, we concluded that the apertures were not always sufficient to completely block molecules that desorbed from the sample holder and developed a procedure to subtract signal attributed to surface sublimation from the TPD distribution.

To subtract the high-temperature feature, its leading (low-temperature) edge was fit to a simple exponential regression equation, which was then subtracted from the entire curve. We chose to use an exponential function because the rise in the rate constant for desorption as a function of temperature is expected to be exponential. The top panel in **Figure 51** shows the mass spectrometer data after baseline correction and signal averaging. Out of twelve experiments, the TPD plots for eight have a high-temperature feature. The exponential regression curves used to remove two of these peaks are displayed in red, and the associated mass spectrometer data are designated with red lines. The bottom panel shows the results after the second peak has been subtracted from all relevant TPD curves. The modified data are designated with green lines. The excellent agreement between modified (green) and non-modified (black) data provide justification for the use of this method of peak subtraction. Further justification is provided by a comparison of results from analysis of only the green traces in the bottom panel of **Figure 51**, only the black traces, and all of them together. The variance among these three results is negligible in comparison to the overall experimental error.

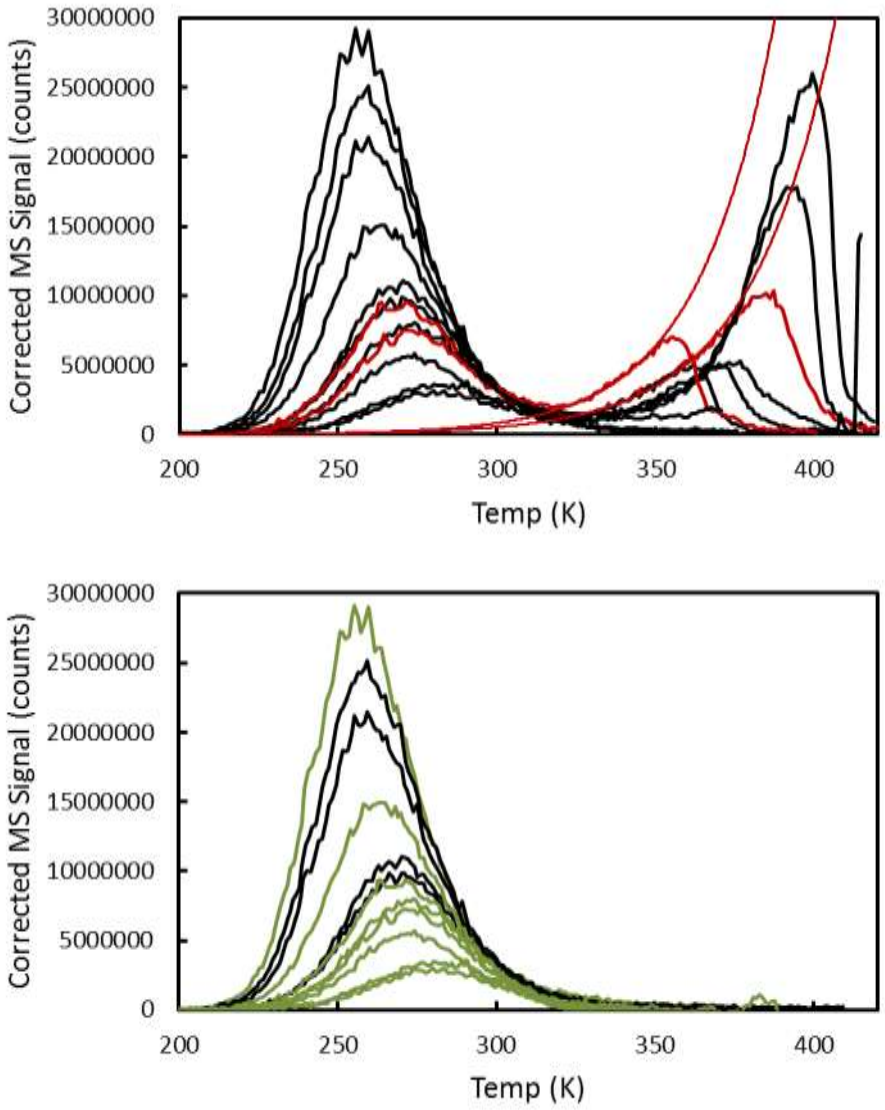

Figure 51. *Mass spectrometer signal intensity as a function of temperature for methyl salicylate desorption from silica after baseline correction and signal averaging. The top panel shows the data prior to peak subtraction (red and black lines) and the exponential functions used to subtract the second peaks (red lines). The bottom panel shows the data after peak subtraction. In the bottom panel, data represented by black lines did not have a second peak and data represented by green lines had the second peak subtracted by the method described in the text.*

Our procedure for TPD data analysis with the inverted Polanyi Wigner equation (**eq 4.2**) and an experimentally determined preexponential factor (ν) is described in Chapter 2. In brief, data from the mass spectrometer was used to determine desorption rate as a function of temperature for several experiments with varying initial fractions of occupied silanol adsorption sites (θ).

Figure 52 shows plots of the desorption rate of methyl salicylate versus temperature for eleven different initial coverages. An initial guess for ν was used to calculate desorption energy as a function of θ for the run with the highest initial θ. This data was then used to simulate plots of desorption rate versus temperature for all of the runs with lower initial values of θ. The same process was repeated for a range of preexponential factors to minimize the difference between experimental and simulated data. **Figure 53** shows the range of prefactor values that were tried for methyl salicylate and the function used to find the best value. The reported results are activation energies of desorption as a function of θ.

$$E_d(\theta) = -k_B T_S ln\left(-\frac{d\theta/dt}{\upsilon\theta}\right) \quad \textbf{(4.2)}$$

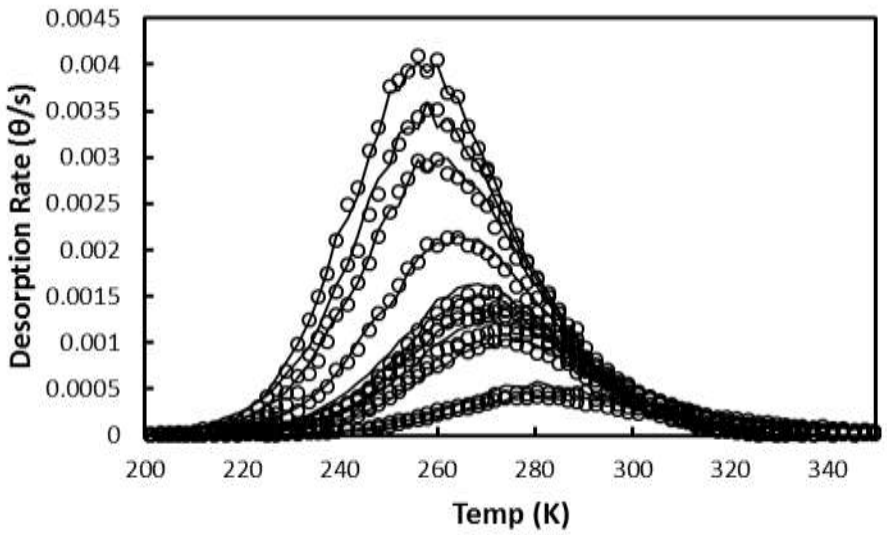

Figure 52. *Experimental (circles) and simulated (lines) plots of desorption rate versus temperature for methyl salicylate at different coverages. This plot was generated after determining*

the best prefactor value. From top to bottom: θ = 0.84, 0.77, 0.66, 0.49, 0.37, 0.34, 0.31, 0.29, 0.23, 0.13, 0.11.

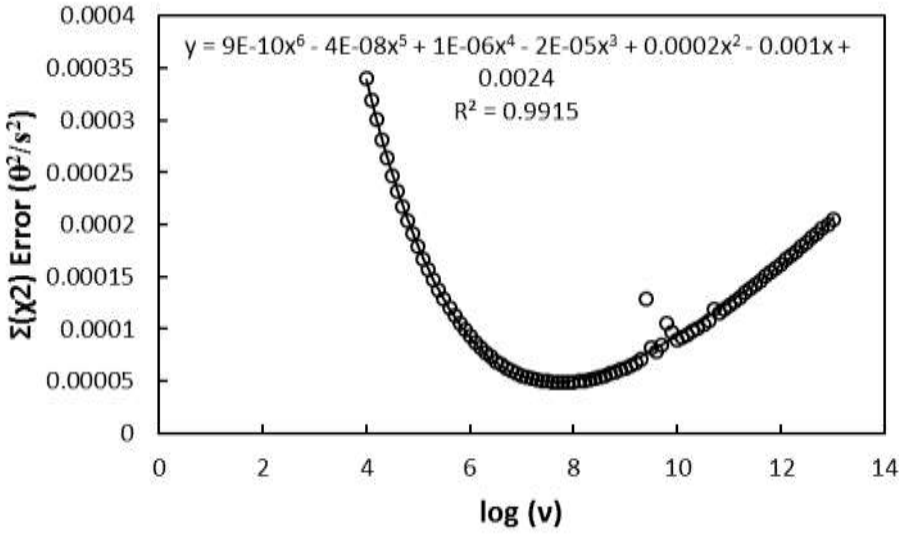

Figure 53. a 6th-order polynomial fit to χ2 error values between simulated and experimental data used to determine the best prefactor value for methyl salicylate. The local minimum of the function was found via the solver functionality in Excel.

5.3 Results and Discussion

5.3.1 IR characterization of adsorption

The IR spectra for gas phase and adsorbed methyl salicylate in **Figure 55** provide evidence that uptake of methyl salicylate is driven by the formation of hydrogen bonds to silica. The frequencies and relative intensities for the IR absorption bands assigned to the aliphatic C-H stretching and aromatic C-C breathing modes are similar in both spectra, which is evidence for molecular adsorption of methyl salicylate without decomposition. The narrow IR band at 3750 cm^{-1}, assigned to the SiOH stretch in free surface silanol groups, decreases with methyl salicylate uptake as two broad IR bands centered at 3440 and 3170 cm^{-1} emerge. This spectral feature is characteristic of the formation of hydrogen bonds and occurs due to charge transfer between the hydrogen bond donor and acceptor orbitals. The lowest-energy unoccupied molecular orbital in

the hydroxyl group is the antibonding σ^* orbital. Electrons from the hydrogen bond acceptor interact with the hydroxyl σ^* orbital and thus weaken the O-H bond. The reduced bond energy is visible spectroscopically as a redshift in the IR absorption band for the hydroxyl group. Likewise, the formation of hydrogen bonds weakens the C=O bond and redshifts the IR bands associated with the stretching mode for that bond. Thus, the ~10 cm^{-1} redshift in the C=O band for methyl salicylate after adsorption evidences an increased extent of charge transfer to the carbonyl group. A similar shift is evident in spectra of all other molecules investigated here that contain carbonyl groups (**Figure 56** to **Figure 60**).

The two distinct IR absorption bands in the hydrogen bonded hydroxyl region in spectra of adsorbed methyl salicylate (see **Figure 55**) provide evidence that multiple types of surface hydrogen bonds are present. Recall that Chapter 3 discussed the uptake of 2-CEES, a molecule with two hydrogen-bond acceptor moieties, on silica. In that case, IR spectra of 2-CEES on silica displayed two distinct features in the absorbance range associated with hydrogen-bonded silanol groups, and these were assigned to SiOH---Cl and SiOH---S hydrogen bonds. In the case of methyl salicylate, assigning IR absorption bands to specific adsorbate-surface hydrogen bonds is less straightforward due to the abundance of potential hydrogen bond donor and acceptor moieties. In fact, IR spectra of gas-phase methyl salicylate (see **Figure 55**), specifically the broad band centered at 3260 cm^{-1} provide evidence of hydrogen bonding before adsorption.

Previous research on the multiple conformers of gas-phase methyl salicylate provides deeper insight into the molecular geometries that give rise to the spectral evidence for hydrogen bonding in gas phase methyl salicylate.[129] The lowest energy geometry of gas-phase methyl salicylate is referred to as ketoB (see **Figure 54**) and has an internal hydrogen bond between the hydroxyl and carbonyl groups. The second lowest energy conformer, referred to as ketoA, has an

internal hydrogen bond between the hydroxyl and ether groups. Experimental[120] and computational[129] results from the literature provide a value of 3262 cm^{-1} for the wavenumber of the O-H stretch for the ketoB form of methyl salicylate, which is in excellent agreement with our result of 3260 cm^{-1} in gas phase methyl salicylate. Computational results for the ketoA conformer provide a value of 3387 cm^{-1} for the O-H stretch.[129] No band is visible at 3387 cm^{-1} in our spectra of adsorbed methyl salicylate (**Figure 55**), which is expected as ketoA is a less energetically favorable configuration than ketoB. Therefore, we conclude that gas-phase methyl salicylate primarily consists of the ketoB conformer.

Although the gas-phase structure of methyl salicylate has been well characterized, a detailed study about the effects of adsorption on the internal hydrogen bond has not yet been published the literature to our best knowledge. Analysis of the two features in the hydrogen-bonded silanol region and the absorption band for the carbonyl stretch in IR spectra of adsorbed methyl salicylate provides important clues about the fate of the internal hydrogen bond after adsorption. Comparisons with IR spectra of other molecules with similar functionalities bound to silica further improve our understanding of the molecular geometry of adsorbed methyl salicylate.

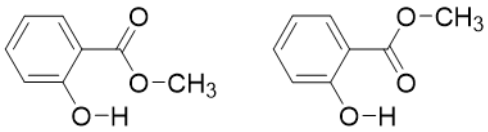

Figure 54. *Schematics of the ketoA and ketoB conformers of methyl salicylate*

Our results provide evidence that the methyl salicylate band centered at 3170 cm^{-1} cannot be assigned to a hydrogen-bonded SiO-H vibration, but is instead likely caused by the hydroxyl group in methyl salicylate. This conclusion can be reached by considering the positions of the SiO-

H IR bands for silanol-benzene, silanol-carbonyl, and silanol-hydroxyl hydrogen bonds in spectra of molecules with simpler uptake mechanism on silica. As shown in Chapter 4, benzene uptake is driven by the formation of hydrogen bonds to the delocalized π electrons. Spectroscopic studies of benzene uptake (**Figure 60**) demonstrate that the absorption band assigned to the silanol-benzene hydrogen bond is around 3600 cm^{-1}. This same band is visible in spectra of adsorbed cresol (**Figure 58**) and benzaldehyde (**Figure 59**) as a shoulder of a larger feature that is attributed to the silanol-hydroxyl hydrogen bond for cresol and the silanol-carbonyl hydrogen bond for benzaldehyde. The IR absorption bands for the hydrogen bonds to oxygen-containing functional groups in cresol, benzaldehyde, and acetone (**Figure 57**) are all centered between 3350 and 3400 cm^{-1}. Regardless of the hydrogen-bond acceptor group, all of the molecules studied here have silanol-adsorbate hydrogen-bond IR bands centered above 3200 cm^{-1}. Therefore, we assign the low-wavenumber 3170 cm^{-1} band for adsorbed methyl salicylate in **Figure 55** to the methyl salicylate O-H stretch, and the 3440 cm^{-1} band to the SiO-H stretch for silanol-methyl salicylate hydrogen bonds.

Our results show that uptake on silica redshifts the O-H IR band for adsorbed methyl salicylate by 80 cm^{-1} compared to the same band in the gas phase. The IR band assigned to the C=O stretch also redshifts (from 1700 to 1680 cm^{-1}) after adsorption. These shifts suggest that the extent of charge transfer to both the methyl salicylate hydroxyl and carbonyl groups is increased by adsorption. This information is insufficient to identify a single most probable molecular geometry for adsorbed methyl salicylate especially due to the width and high degree of overlap of the IR bands. In fact, multiple molecular geometries with similar surface-adsorbate bond energies and IR features likely exist. However, the spectroscopic data presented here provides important clues that narrow the possibilities. Specifically, the low vibrational energies of the C=O and O-H

bonds after uptake suggests that both moieties are likely involved in hydrogen bonds when methyl salicylate is adsorbed on silica.

Therefore, if the ketoA conformer or another configuration with no internal hydrogen bond becomes more probable than the ketoB conformer after adsorption, it is likely that both the hydroxyl and carbonyl groups form hydrogen bonds to silica. The vibrational energies for the O-H and C=O stretches for ketoA have been shown to be larger than for the ketoB conformer.[129] Therefore, blueshifts in the hydroxyl and carbonyl bands would be expected instead of redshifts if the ketoA conformer became the preferred geometry without the formation of a surface-carbonyl hydrogen bond. A blueshift would also be expected if the internal hydrogen bond broke and the carbonyl and hydroxyl groups remained free.

An uptake mechanism where the internal hydrogen bond breaks to allow the methyl salicylate hydroxyl and carbonyl groups to interact with oxygen atoms on the surface of silica and form adsorbate-surface hydrogen bonds is consistent with our IR spectra. It is plausible that such hydrogen bonds could attain more favorable geometries than internal hydrogen bonds and therefore experience a greater extent of charge transfer. However, it is not necessary for the internal hydrogen bond to break for carbonyl-surface or hydroxyl-surface hydrogen bonds to form. Thus, another possible uptake mechanism is that methyl salicylate may remain in the ketoB conformer, and interactions with surface silanol groups provide additional charge transfer to both the hydroxyl and carbonyl groups. Finally, the ketoA conformer may become more energetically favorable, with the carbonyl groups hydrogen bonded to silica and the hydroxyl group involved in two hydrogen bonds (to surface silanol groups and internally to the ether oxygen atoms). Future work, employing synchrotron X-ray diffraction (XRD) analysis for example, will be needed to learn more about the

fate of the internal hydrogen bond in adsorbed methyl salicylate and the roles of the oxygen-containing functional groups in uptake.

Interestingly, in contrast to other functionalized benzene derivatives studied in this chapter and also in the previous chapter, the aromatic ring in methyl salicylate does not appear to play a significant role in hydrogen bonding. This conclusion is based on IR analysis of m-cresol (**Figure 58**) and benzaldehyde (**Figure 59**) uptake on silica. Specifically, the SiOH region in the spectra of adsorbed m-cresol and benzaldehyde both feature two distinct absorption bands. The main band is in the range associated with SiOH---carbonyl and SiOH---hydroxyl hydrogen bonds. A small band, visible as a shoulder, is in a similar position as the SiOH---π bond for benzene (see **Figure 60**). The spectra for adsorbed methyl salicylate (**Figure 55**) and methyl 2-methyl benzoate (**Figure 56**) do not have a visible shoulder in the SiOH---π range. As will be discussed further in the following section, the π---OH interaction is weaker than hydrogen bonds to oxygen-containing hydrogen-bond acceptors such as carbonyl groups. Thus, the abundance of strong hydrogen-bond acceptors in methyl salicylate and methyl 2-methyl benzoate likely dominates the weaker interaction to the aromatic ring.

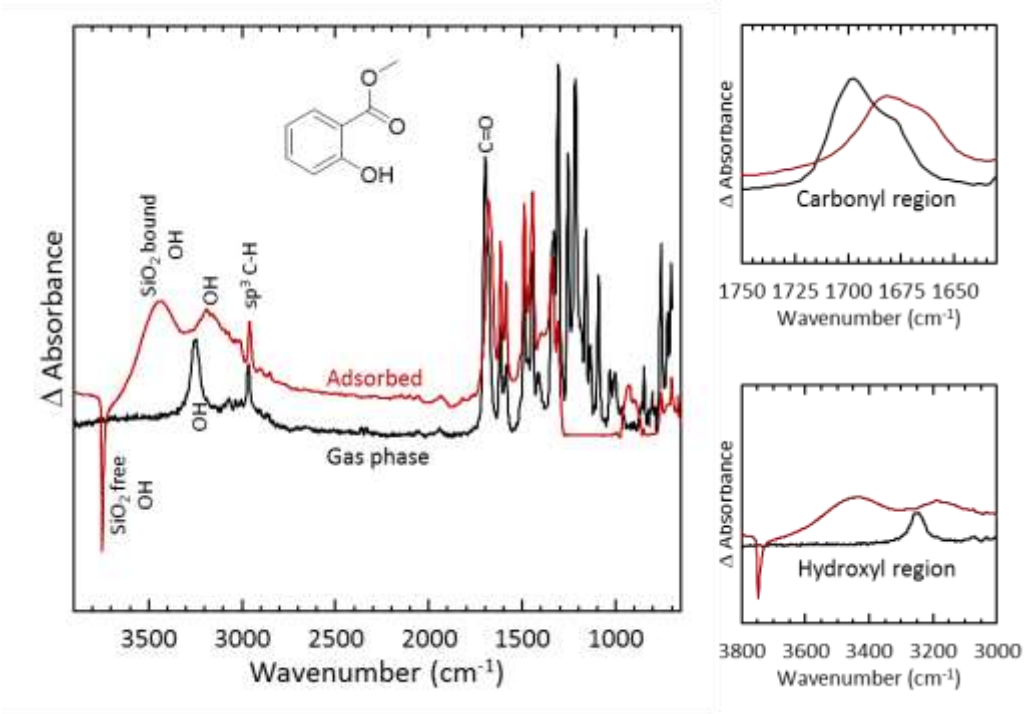

Figure 55. *IR spectra of methyl salicylate in the gas phase (black lines) and adsorbed on silica (red lines). The carbonyl and hydroxyl regions are reproduced at a larger scale in the panels on the right to show details more clearly.*

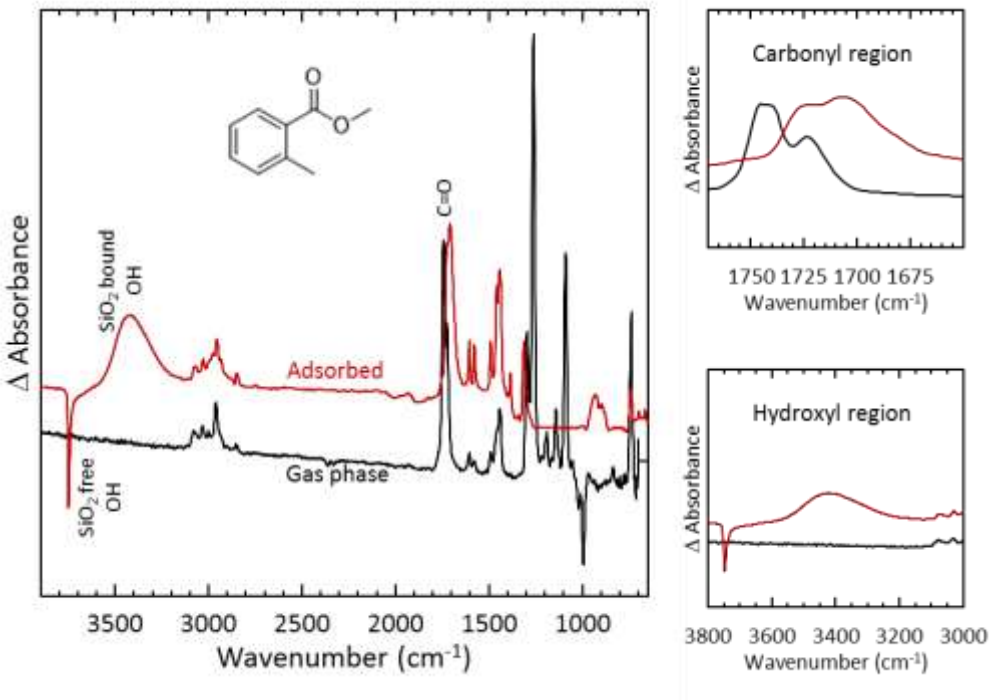

Figure 56. *IR spectra of methyl 2-methyl benzoate in the gas phase (black lines) and adsorbed on silica (red lines). The carbonyl and hydroxyl regions are reproduced at a larger scale in the panels on the right to show details more clearly.*

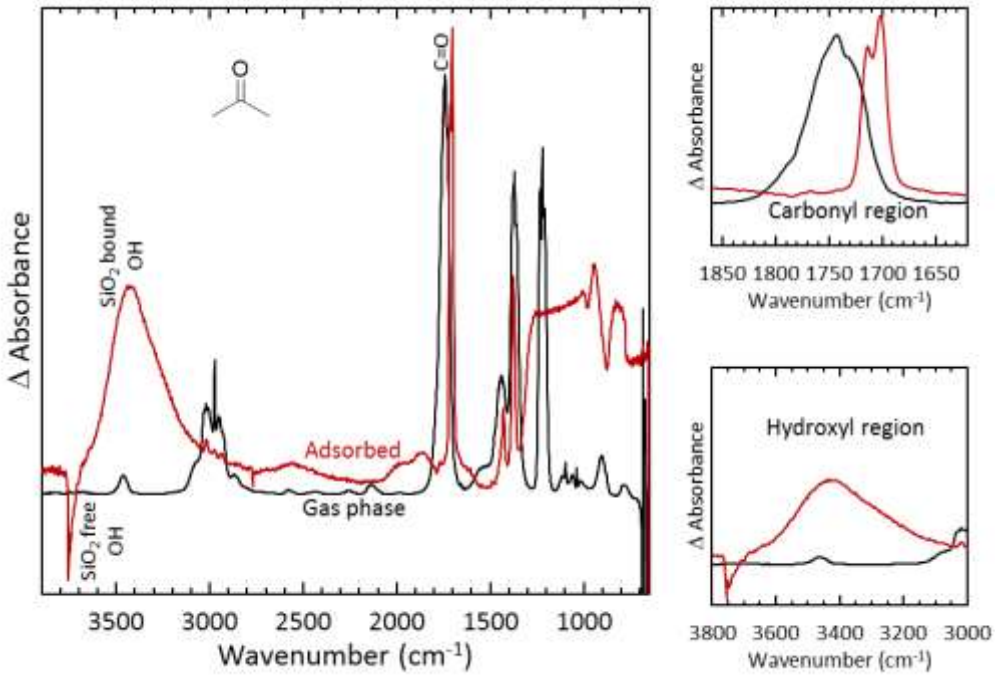

Figure 57. *IR spectra of acetone in the gas phase (black lines) and adsorbed on silica (red lines). The carbonyl and hydroxyl regions are reproduced at a larger scale in the panels on the right to show details more clearly.*

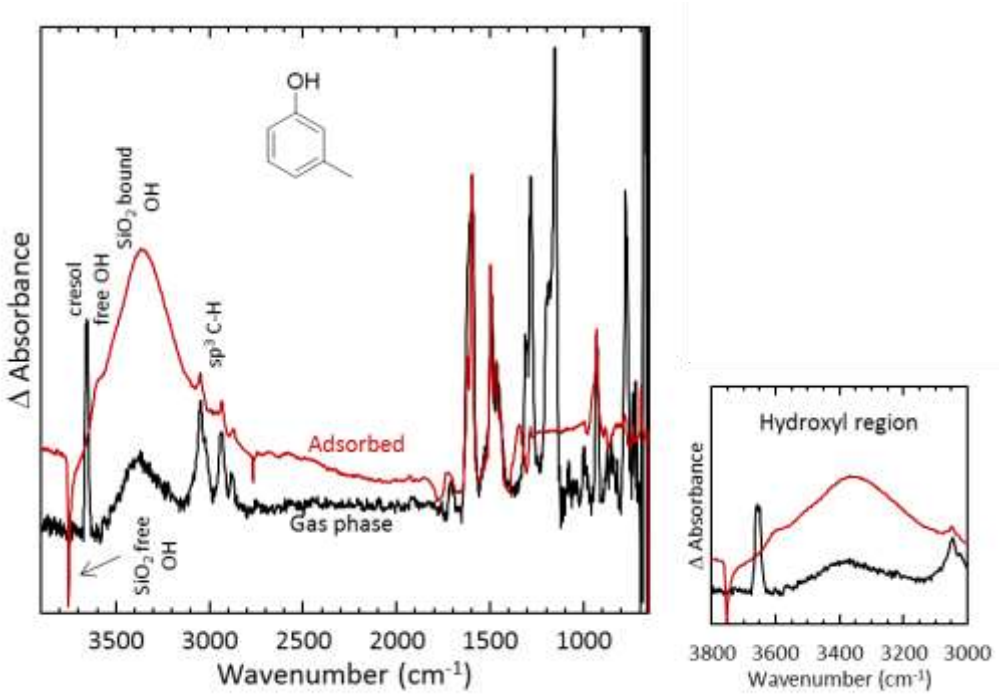

Figure 58. *IR spectra of m-cresol in the gas phase (black lines) and adsorbed on silica (red lines). The hydroxyl region is reproduced at a larger scale in the panel on the right to show details more clearly.*

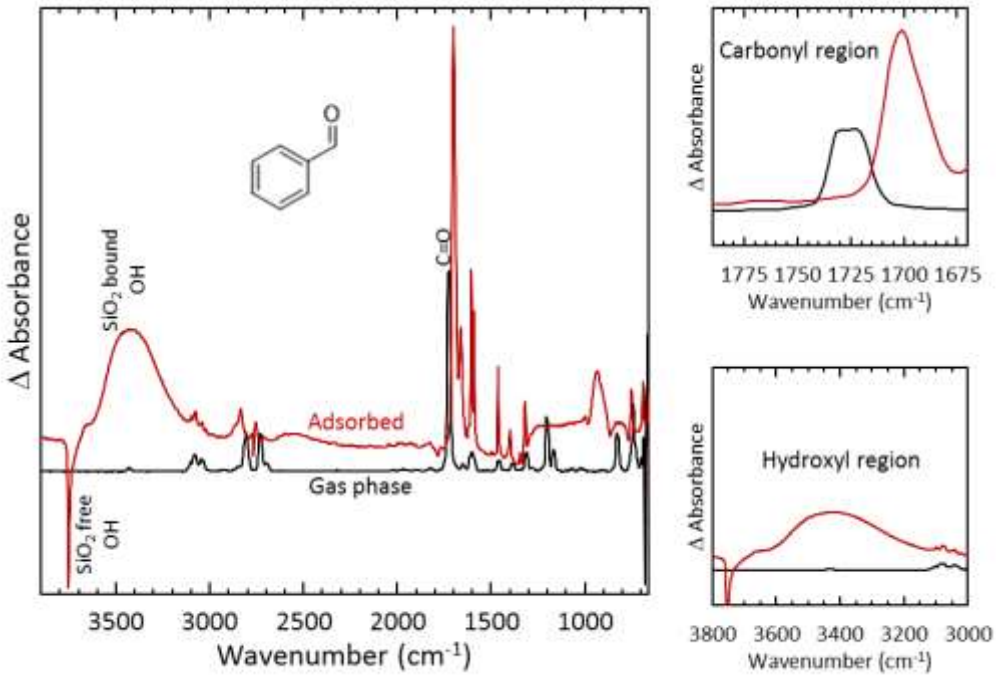

Figure 59. *IR spectra of benzaldehyde in the gas phase (black lines) and adsorbed on silica (red lines). The carbonyl and hydroxyl regions are reproduced at a larger scale in the panels on the right to show details more clearly.*

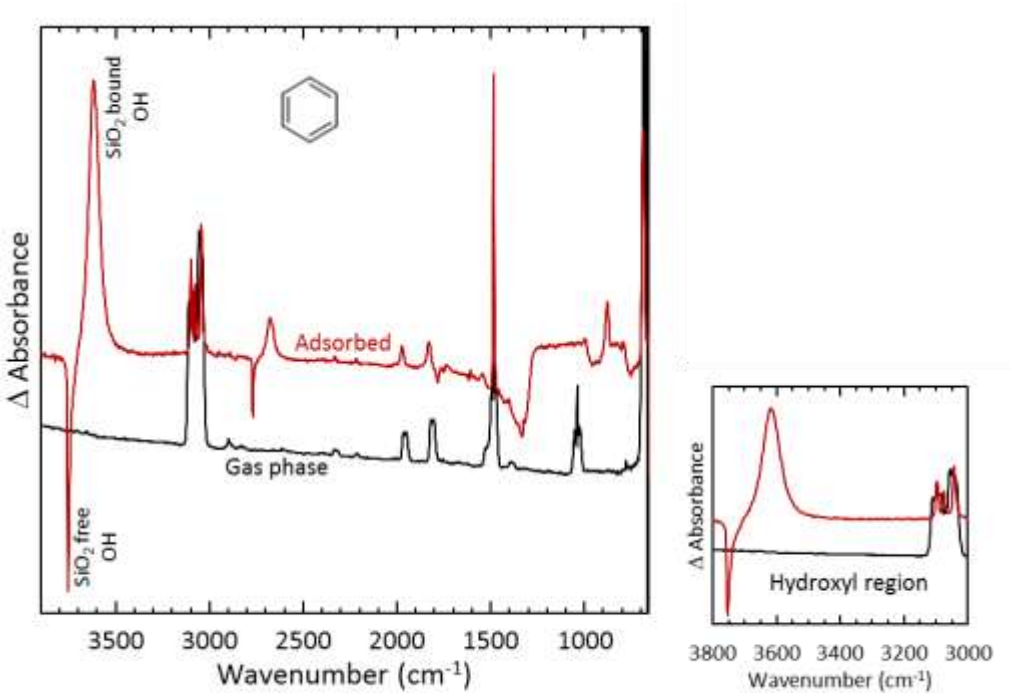

Figure 60. *IR spectra of benzene in the gas phase (black lines) and adsorbed on silica (red lines). The hydroxyl region is reproduced at a larger scale in the panel on the right to show details more clearly.*

5.3.2 TPD determination of molecule-silica binding energies.

The strength of each type of hydrogen bond that can form between methyl salicylate and silica was assessed by measuring the desorption energies for a series of simpler aromatic compounds and acetone with the same TPD and inversion analysis procedures described in previous chapters. The energies, in the limit of zero coverage, are presented in **Table 13 and Figure 61**. Of note, these measurements were collected prior to all others reported in this thesis and prior to several improvements in the data acquisition process. Therefore, experimental reproducibility at this point was less than in later measurements. The experimental error (defined as one standard deviation of multiple TPD measurements on methyl salicylate) in the desorption

energies reported in this chapter is ± 2.9 kJ/mol, which is higher than the error for the data presented in other chapters (± 2.3 kJ/mol).

The desorption energies of acetone and benzene were measured to compare the hydrogen bonding behavior of an aromatic system and a carbonyl functional group with minimal influences from substituents. As discussed in Chapter 4, the SiOH---π hydrogen bond is a weaker interaction than typical hydrogen bonds to oxygen- and nitrogen- containing molecules.[130] Here, this is evident in the ca. 20 kJ/mol energy difference between benzene and acetone. A portion of this difference may be due to dispersion forces rather than the strength of the hydrogen bond since, as discussed in Chapter 3, each methyl group can increase the desorption energy of a substituted hydrocarbon by ca. 5 kJ/mol. However, even if non-hydrogen-bonding contributions to the desorption energy for acetone are considered, a large portion of the energy difference between benzene and acetone can still be attributed to the hydrogen bond. It follows that the aromatic group in methyl salicylate likely provides a much weaker hydrogen bond acceptor than the carbonyl group.

TPD was performed on benzaldehyde to investigate the nature of hydrogen bonding to aromatic and carbonyl moieties when these groups are adjacent to each other in the same molecule. IR spectra of adsorbed benzaldehyde (see **Figure 59**) indicate that both SiOH---π and SiOH---carbonyl hydrogen bonds play a role in benzaldehyde adsorption. However, these interactions may not exist simultaneously in a single molecule. In our results, the desorption energy for benzaldehyde was 4 kJ/mol lower than for acetone. Because TPD measurements probe the sum of all surface-adsorbate interactions, a molecule bound to a surface by two hydrogen bonds would be expected to have a higher desorption energy than a molecule bound by a single hydrogen bond. For example, work by Bermudez et al. showed that bidentate hydrogen bonds can be as much as a factor of two higher in energy than monodentate bonds.[107] If bidentate hydrogen bonds drive

uptake of benzaldehyde, we suggest that the SiOH---π and SiOH---carbonyl hydrogen bonds may be constrained by each other from their most energetically favorable orientations, and each hydrogen bond is therefore weaker than expected.

Alternatively, there may be a distribution of benzaldehyde molecules bound by a lone carbonyl hydrogen bond and the remainder by a lone pi hydrogen bond. In this case, it is interesting that benzaldehyde has a lower desorption energy than acetone, which is a smaller molecule with less potential for dispersion forces. The aromatic system adjacent in benzaldehyde has an electron-withdrawing effect on the carbonyl group, which may therefore result in a weaker SiOH---carbonyl interaction than in acetone. Further work, possibly with crystallographic methods or theory, will be necessary to determine the correct adsorption mechanism for benzaldehyde.

TPD experiments were conducted with m-cresol to compare the desorption energies for aromatic hydroxyl and carbonyl groups. The desorption energy for m-cresol was slightly lower than for benzaldehyde. This can be explained by considering the resonance structures for both molecules. In cresol, resonance gives the oxygen atom a positive charge. In benzaldehyde, resonance gives the oxygen atom a negative charge. The electrostatic component of a hydrogen bond's energy is strengthened by a more negative charge on the hydrogen bond acceptor, thus m-cresol is expected to have a weaker hydrogen bond. It follows that the hydroxyl group in methyl salicylate may also form slightly weaker hydrogen bonds than the carbonyl group for the same reason. However, this difference, if it exists, is too small to be detected by the methods used in this work.

Finally, the desorption energies for methyl salicylate and methyl 2-methyl benzoate were measured to determine the role of the hydroxyl group. Both molecules have higher binding energies than m-cresol or benzaldehyde as expected due to the larger molecular size and increased

number of atoms available to interact with the surface through dispersion forces. Furthermore, methyl salicylate and methyl 2-methyl benzoate have similar desorption energies; the variance is less than the standard deviation of repeated experiments with the same molecule. Thus, the absence of the hydroxyl group does not significantly change the desorption energy. This is further evidence in support of the significant role of the carbonyl group in uptake on silica. The data also suggests that a bidentate structure with a single methyl salicylate molecule bound by both carbonyl and hydroxyl groups simultaneously does not form, as a bidentate structure would be expected to have a higher binding energy.[107] However, the hydroxyl group may still play a significant role in uptake of methyl salicylate. It is likely that the hydroxyl and carbonyl moieties form hydrogen bonds of similar energies, as evidenced by the similar binding energies of m-cresol and benzaldehyde. Therefore, similar to 2-CEES in the previous chapter, a fraction of adsorbed methyl salicylate molecules may form hydrogen bonds through the carbonyl group and the remainder through the hydroxyl group. Methyl 2-methyl benzoate has no hydroxyl group, so all molecules form hydrogen bonds through the carbonyl group with a similar energy as methyl salicylate.

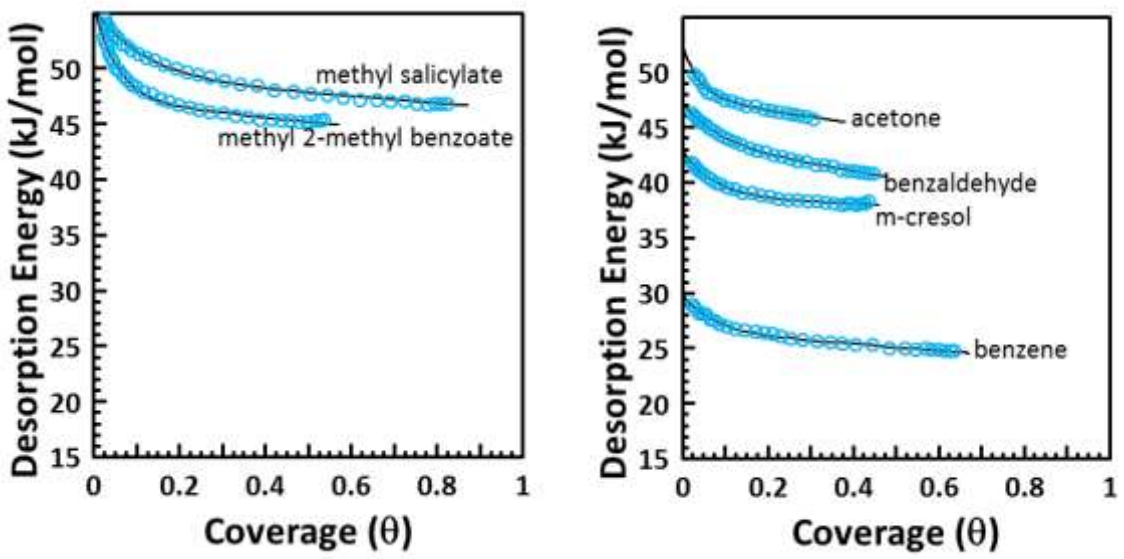

Figure 61*. Activation energies of desorption for methyl salicylate and methyl 2-methyl benzoate (left panel) and acetone, benzaldehyde, m-cresol, and benzene (left panel)*

Table 13. *Activation energies of desorption, prefactors, and wavemunbers of the O-H stretch for all molecules studied in this chapter. Error for the desorption energies were determined by calculating the standard deviation of replicate runs of the same molecule.*

molecule	E_d (± 2.9 kJ/mol)	log(ν) (± 0.6)	ν(OH) (cm^{-1})
Methyl salicylate	49.2	7.6	3444
Methyl 2-methyl benzoate	47.2	7.0	3411
Benzaldehyde	43.6	6.6	3407
m-cresol	38.7	5.9	3342
Acetone	47.7	7.5	3394
Benzene	26.6	4.6	3608

5.4 Summary

Several important observations can be made from our results about the forces involved in uptake of methyl salicylate on a hydrogen-bonding surface. The carbonyl and hydroxyl moieties are both likely significantly involved in hydrogen bonding with a fraction of the molecules bound by the carbonyl group and the remainder by the hydroxyl group. Neither spectroscopic or TPD data is able to differentiate between carbonyl---silanol and hydroxyl---silanol hydrogen bonds;

these interactions likely have similar strengths. The internal hydrogen bond present in gas-phase methyl salicylate may break in favor of an adsorbate---surface hydrogen bond. Alternatively, the internal hydrogen bond may persist while the carbonyl forms a second hydrogen bond with the surface. The aromatic ring, although a viable hydrogen bond acceptor as shown by the uptake of benzene, m-cresol, and benzaldehyde, does not appear to be significantly involved in uptake of methyl salicylate. The role of the ether group was not assessed in this study. The IR mode that could be used to probe the presence or absence of hydrogen bond effects on the oxygen atom is near 780 cm^{-1}, which is part of the region obscured by intense IR absorption bands caused by the bulk vibrational modes of silica. A future study of aromatic ethers or a comparison of acetone to dimethyl ether could potentially reveal further information about the ether oxygen atom in methyl salicylate.

Compared to 2-CEES and HD, methyl salicylate has only a slightly higher binding energy to silica (49.2 versus 44.9 kJ/mol), and a similar prefactor (7.6 versus 8.4). 2-CEES remains the preferred simulant molecule for fundamental surface studies of HD due to its similarity. However, studies that use methyl salicylate could also potentially provide useful information. This is a remarkably fortuitous coincidence since methyl salicylate has nothing in common with 2-CEES or HD structurally.

Chapter 6: Uptake of HD Simulants on UiO-66

6.0 Prologue

For a capstone project, we focused on extending the TPD methods developed and described in previous chapters to more complex molecular solids. In this chapter, we report the first TPD-based studies of adsorption on a porous surface with both organic and inorganic components. Specifically, this chapter describes initial efforts to characterize the uptake of sulfur mustard (HD) simulants on the metal-organic framework (MOF) UiO-66. TPD analysis was initially developed for use on single-crystal surfaces. Single-crystal studies provide important data about the fundamental nature of interfacial interactions. However, studies of uptake on particulate materials are more directly relevant to chemistry in typical ambient conditions and therefore of great interest to surface science research in many fields including catalysis and environmental chemistry. Thus, recent work, including the projects described in the previous chapters, has developed procedures to analyze particulate materials with TPD and IR spectroscopy. Previous such studies have been limited to simple metal oxide or inorganic materials such as SiO_2, and amorphous frozen water. Here, we apply the techniques described in the previous chapters to explore the interactions that drive adsorption on UiO-66.

6.1 Introduction

MOFs are a relatively new type of porous, high-surface area materials that consist of inorganic nodes joined by organic linkers in a crystalline extended network. The narrow distribution of pore sizes and highly-tunable nature of MOFs make them suitable for a wide variety of applications related to gas adsorption including selective adsorption based on molecular size,[56,57] gas storage,[58,59] and catalysis.[60–63] These materials have also attracted much interest in

research related to defense against and decontamination of chemical warfare agents (CWAs) for their ability to adsorb large amounts of agent and catalyze decomposition of the adsorbed molecules.[55,64–66] However, the potential usefulness of many MOFs is compromised by their instability in conditions that exist in typical environmental, military, and industrial applications. For example, MOF-5 (a $Zn_4O(CO_2)_6$-based MOF)[67] and HKUST-1 ($Cu_2(OH)_2(CO_2)_4$-based MOF)[68] both decompose when exposed to atmospheric moisture.

Much recent work has focused on UiO-66 and similar Zr-based MOFs because they exhibit excellent stability against high temperature, moisture, and mechanical stress.[69–71] Researchers have reported that UiO-66 remains stable after exposure to a variety of solvents (e.g. benzene, and acetone), boiling water, dry air at 573 K, and 10,000 g/cm^2 of mechanical pressure.[72,73] Decomposition is not observed until over 773 K.[73] The robustness of UiO-66 has been attributed to the strong bonds that join the inorganic and organic components.[72] A schematic of the structure of UiO-66 is provided in **Figure 62**. The framework consists of $Zr_6O_4(OH)_4$ nodes connected by 1,4-benzenedicarboxylate (BDC) linkers to form a highly regular crystalline arrangement with 0.6 nm openings.[72] The Langmuir surface area is 1187 m^2/g.[72] Although a perfect sample of UiO-66 would have 12 linkers per node, studies indicate that real UiO-66 samples often have 11 or fewer linkers per node.[54,73,74] These missing-linker defect sites have been shown to increase pore volume and surface area and, therefore, have a direct effect on gas adsorption as will be discussed below.[54]

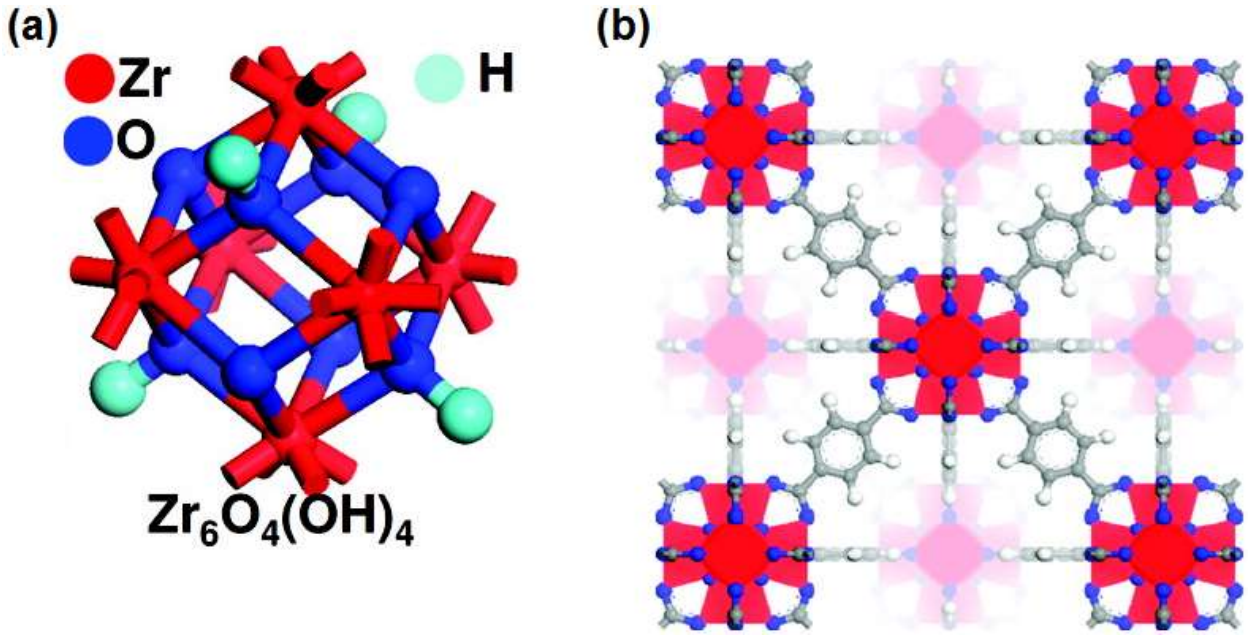

Figure 62. *Schematics of the 3D structure of UiO-66. Panel a on the left depicts the Zr6O4(OH)4 inorganic node. Panel b on the right depicts how the inorganic nodes and organic BDC linkers connect. Zirconium, oxygen, carbon, and hydrogen atoms are red, blue, gray, and white, respectively. Reprinted (adapted) with permission from Cavka, J. H.; Jakobsen, S.; Olsbye, U.; Guillou, N.; Lamberti, C.; Bordiga, S.; Lillerud, K. P. A New Zirconium Inorganic Building Brick Forming Metal Organic Frameworks with Exceptional Stability. J. Am. Chem. Soc.* ***2008****, 130 (42), 13850–13851. Copyright 2016 American Chemical Society.*

Previous research on UiO-66 has carefully characterized how its structure is affected by environmental conditions[73] and explored the molecular geometry of small adsorbed gas molecules such as water, carbon dioxide, and methane.[74,75] When exposed to atmospheric moisture, UiO-66 contains hydroxyl groups in the inorganic nodes. These can be reversibly removed and replaced by exposure to high temperature and water respectively. Both hydroxylated and dehydroxylated forms can bind a large volume of gas, and the Zr metal centers in the nodes have been identified as the likely primary gas adsorption sites.[74,76] The hydroxylated form exhibits higher performance for uptake of CO_2 due to the formation of electrostatic interactions between the adsorbate's oxygen lone pairs and the hydroxyl group.[74] Similar hydrogen bonds may play an important role in enhancing uptake of CWAs.

The Zr metal centers in MOFs have been identified as key adsorption sites; therefore, access to the inorganic nodes inside pores is important. For example, uptake of water molecules has been shown to increase when the synthesis of UiO-66 is modified to increase the number of missing linker defects, which increases both pore volume and surface area.[54] In addition to small gas uptake, researchers have explored MOFs for the uptake and possible decomposition of CWAs. In those studies, access to the nodes was also found to be critically important. For example, a 30-fold improvement in decomposition rate was achieved by using dehydrated NU-1000 instead of UiO-66 for decomposition of the nerve agent simulant dimethyl 4-nitrophenyl phosphate (DMNP). [77] These MOFs are similar, but the framework of NU-1000 consists of eight inorganic nodes instead of twelve and has an extended structure with pores approximately three times larger than UiO-66.[78] The improved performance of NU-1000 was attributed to an increased ability for adsorbate molecules to fit inside of the pores and access the catalytically active Zr nodes.

Although the improved performance of MOFs with larger pores likely applies to all CWAs, smaller agents such as HD (see Chapter 1 for information about properties and the molecular structure of HD) may able to completely permeate UiO-66 and access all binding sites in the pores. A detailed study of HD uptake on UiO-66 has not yet been reported in the literature. 2-CEES is a common HD simulant with similar molecular structure but sufficiently low toxicity avoid the strict safety restrictions imposed on CWAs. Studies show that 2-CEES is a good surrogate for HD in surface studies.[79] For example, as shown in Chapter 3, both molecules have similar uptake behaviors on a hydrogen-bonding surface.

The work presented here explores the uptake of 2-CEES on UiO-66. In this study, we combined IR spectroscopy and TPD measurements to study multiple aspects of the adsorption mechanism for 2-CEES on UiO-66. Specifically, IR was used to observe changes in surface and

adsorbate vibrational modes and thus probe the extent of charge transfer in the hydrogen bonds that formed during uptake on hydroxylated UiO-66. Temperature programmed desorption was used to measure the combined strength of MOF-adsorbate interactions for 2-CEES and the series of closely related molecules shown in **Figure 63**. Chemical and physical properties of these compounds are discussed in Chapter 1. The binding energies and IR spectra recorded here provided new insight how dispersion forces and hydrogen bonding contribute to 2-CEES uptake.

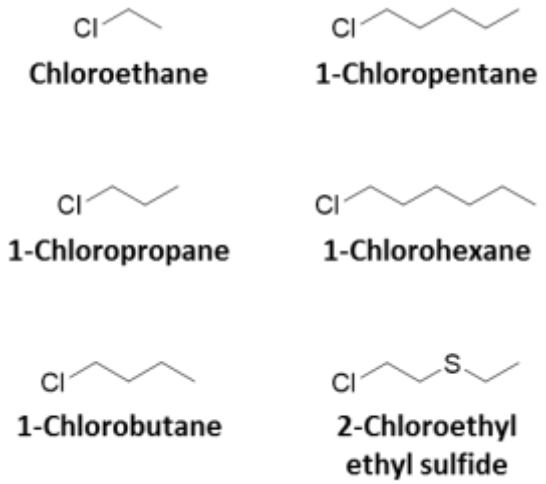

Figure 63. *IUPAC names and schematics for the molecules studied in this chapter.*

6.2 Experimental

6.2.1 Preparation of UiO-66

The UiO-66 employed in this work was synthesized by Hill et al. at Emory University with a procedure already described.[85] The general steps were to dissolve $ZrCl_4$ and benzenedicarboxylic acid in a 1:1 mole ratio in dimethylformamide (DMF) and place the resulting mixture in an oven held at 373 K for 36 hours. Some synthesis procedures reported in the literature[131] used a modulator

such as HCl with the effect of increased reaction rate, increased surface area in the MOF product, and a greater number of missing-linker defects in the MOF. However, no such modulator was used during the synthesis for the samples studied here. After removal from the oven, the product was placed in a 333 K water bath and rinsed with ethanol for 3 days. The clean powder was then filtered from the suspension and dried under vacuum at room temperature. After drying, IR spectra shown in the Results and Discussion section below indicated that DMF solvent remained trapped in the pores after drying. Therefore, samples were activated by heating to 573 K in a vacuum chamber prior to adsorption experiments. PXRD patterns collected on the UiO-66 particles synthesized for this work indicate that they contain missing-linker defects. The PXRD pattern of UiO-66, shown in **Figure 64**, contains two broad, symmetry forbidden reflections for the topological space group (Fm-3m, 225) at 2θ lower than the (111) reflection. These features have previously been attributed to missing-linker defects.[69,132]

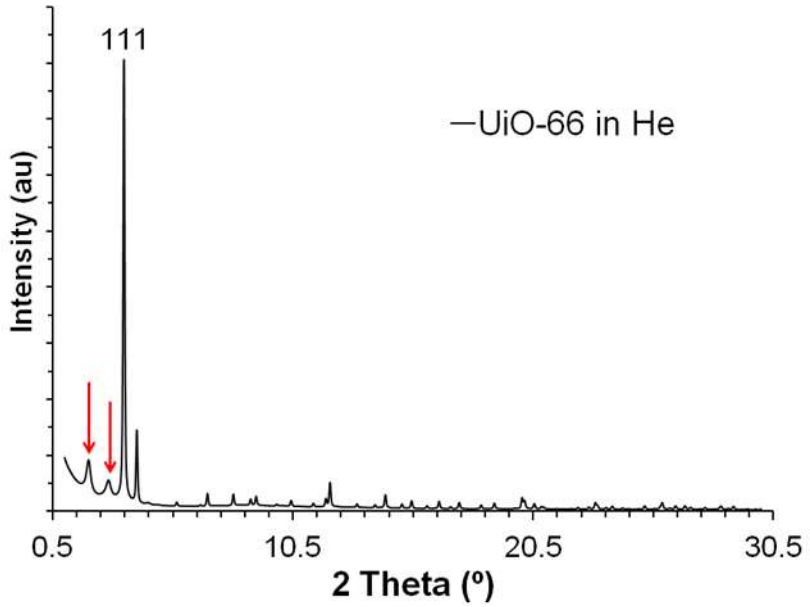

Figure 64*. PXRD pattern of UiO-66 collected in He, red arrows indicate diffuse, symmetry-forbidden peaks, indicating the presence of missing linker defects within the framework.*

All experiments were conducted in a UHV chamber with a base pressure of 10^{-9} torr to minimize surface contamination and reduce interference from background gasses on mass spectrometer measurements. Details about the UHV chamber are provided in Chapter 2. UiO-66 powder was pressed into a tungsten mesh with the same procedure used for silica. Immediately after pressing, all excess UiO-66 not trapped in the holes of the mesh was carefully scraped away with a clean razor blade. This extra step reduced the thickness of the pressed UiO-66 sample and was necessary to obtain sufficient IR signal through the sample. The mesh was mounted on an X-Y-Z manipulator to allow precise control over sample position within the chamber. Sample temperature, measured by type K thermocouple, was increased by resistive heating with current from a power supply and decreased by direct thermal contact with liquid nitrogen. The temperature was regulated by a proportional-integral-derivative controller that used a feedback loop to adjust current from the power supply.

6.2.2 Dosing

All chemicals used (IUPAC names and molecular structures are listed in **Figure 63**) were purchased from Sigma Aldrich and purified with at least two freeze-pump-thaw cycles immediately before use. The custom manifold and capillary array doser described in Chapter 2 were used to expose the UiO-66 sample to vapors of each adsorbate under UHV conditions. The UiO-66 sample was cooled to cryogenic temperatures to maximize uptake during the period of exposure to the molecule under investigation. Dosing conditions for each molecule are listed in **Table 14**. For all experiments except those with chloroethane, dosing time was about 4 minutes. The interaction between UiO-66 and chloroethane was too weak for rapid uptake even at the lowest temperature attainable by our equipment (125 K). Ambient heat from thermal contact of the sample with the room-temperature exterior of the manipulator and chamber prevented the sample from reaching the same temperature as the liquid nitrogen (77 K) inside of the manipulator tube and feedthrough. Therefore, dosing time was increased to 60 minutes for chloroethane to obtain sufficient uptake for the desired measurements. Based on the results in Chapter 3 for chloroethane on silica, the temperature limitations of the chamber likely prevent measurement of binding energies below 25 kJ/mol. Changes in the surface vibrational modes of UiO-66 before, during, and after dosing were monitored with a Nicolet Nexus 670 infrared spectrometer set to record 64 scans at 4 cm^{-1} resolution. IR spectra were also used to identify and characterize molecules adsorbed to the surface.

Table 14. *Experimental conditions for chloroalkanes on dehydroxylated UiO-66*

Molecule	Dosing temperature (K)	Dosing duration (minutes)	Anneal temperature (K)
Chloroethane	126	60	167-217
1-Chloropropane	132	4	233-283
1-Chlorobutane	132	4	253-313
1-Chloropentane	144	4	263-303
1-Chlorohexane	144	4	273-333

6.2.3 Post-dosing sample treatment

The sample was heated immediately after the dosing procedure to achieve an even distribution of molecules throughout the bed of pressed UiO-66 particles, a necessary requirement for TPD measurements from highly porous materials.[95] The maximum temperature and duration of the anneal process was varied as a convenient and reproducible method to adjust the amount of adsorbate on the surface. Anneal temperatures are listed in **Table 14**. Sufficient annealing was verified by good alignment of the trailing edges of TPD curves at different surface coverages, which indicated that the adsorbed molecules were well-distributed throughout the sample.[95] The sample was cooled to the dosing temperature before the start of the TPD experiment to ensure that the desorption rate was near zero at the beginning of the experiment.

6.2.4 TPD measurements

TPD data was obtained by heating the sample at a linear rate of 0.2 K/s with a proportional-integral-derivative controller and detecting desorbed species in an axially mounted, doubly differentially pumped mass spectrometer (Extrel) tuned to the most abundant mass fragments for that molecule. Apertures restricted the view from the mass spectrometer to a 0.35-cm^2 spot on the

surface and ± 0.4° acceptance angle to minimize signal caused by molecules that desorbed from the sample holder.

Our procedure for TPD data analysis with the inverted Polanyi Wigner equation (eq 4.2) and an experimentally determined preexponential factor is described in Chapter 2. In brief, data from the mass spectrometer was used to determine desorption rate as a function of temperature for several experiments with varying initial coverages. The desorption rate was used to calculate the activation energies of desorption as a function of temperature. Results are reported as activation energies of desorption in the limit of zero coverage.

Inversion analysis requires a reliable method to evaluate initial coverage. For silica, the spectroscopic signature of the O-H vibration indicates the fraction of occupied silanol groups, and saturation (or $\theta = 1$) is defined as 100% silanol occupation. The same method was used for hydroxylated UiO-66, where saturation was defined by 100% hydroxyl occupation. However, dehydroxylated UiO-66 lacks a spectroscopic band that changes in intensity proportionally with uptake. Therefore, saturation was defined by the profile of the TPD curves. **Figure 65** shows TPD plots for desorption of 1-chloropropane and 1-chlorobutane from dehydroxylated UiO-66 at several different initial coverages. The lowest coverages have a single feature and align on the trailing (high-temperature) edges, as expected for first order desorption from strong surface binding sites. The highest coverage data with a single feature was used to define saturation ($\theta = 1$) of the sites available for strong molecule-MOF interactions. θ for each experiment with a sub-saturation initial coverage was determined by calculating the ratio of the integrated area under its TPD distribution to the area under the TPD distribution for $\theta = 1$.

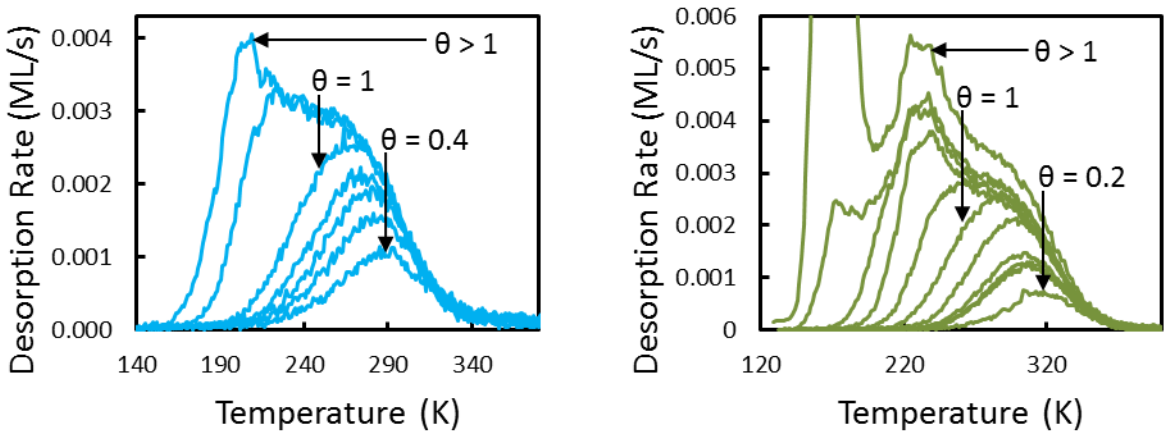

Figure 65. *Desorption rate vs temperature plots for several multilayer and sub-monolayer initial coverages of 1-chloropropane (left) and 1-chlorobutane (right) from dehydroxylated UiO-66. As described in the text, θ = 1 represents saturation of the strong surface binding sites.*

TPD plots with initial coverages higher than saturation have additional low-temperature features that are centered at the same temperature regardless of initial coverage. The shape of these peaks indicates a narrow distribution of binding energies among these weakly-interacting molecules or an inability for them to find the strongest available binding sites before desorption.[94] In the case of desorption from silica, the low-temperature peaks might be attributed to the presence of multilayers, as described in Chapter 4. However, the presence of nanometer-scale pores allows an alternative interpretation. A high occupancy of pores could restrict the motions of molecules or cause molecule-molecule interactions to dominate over molecule-MOF interactions even at sub-monolayer coverages. In either case (multilayers or high occupancy), only the data associated with the highest temperature TPD is representative of both strong adsorbate-MOF interactions and high diffusion rate of adsorbates with respect to the temperature ramp rate. Inversion analysis was therefore only performed on data with initial coverages below saturation, data with a single peak, to determine desorption energies. Leading edge analysis was performed on data with multiple peaks to calculate the desorption energy for these more weakly bound molecules.

6.3 Results and Discussion

We have explored the fundamental nature of 2-CEES and linear chloroalkane adsorption on UiO-66 to determine the uptake mechanism and build an understanding for how the structure and functionality of linear alkanes affect the energetics of adsorbate-MOF binding. In this work, IR spectroscopy was used to probe adsorption mechanisms. TPD measurements were used to determine activation energies for desorption and thus gain insight into the overall strength of the interactions between the adsorbed molecules and the MOF. These techniques provided new insight into the accessibility of adsorption sites inside pores with nanometer-scale diameters for uptake of functionalized linear alkanes. These studies are the first to apply UHV-based surface science methods to the study of gas uptake into MOFs.

6.3.1 Effects of vacuum, temperature, and exposure to chemicals on UiO-66

Other research groups have shown that UiO-66 displays excellent stability when exposed to vacuum, high temperature, and chemicals.[72,73] Consistent with this previous work, our studies show that the IR spectra and PXRD patterns of UiO-66 change little upon thermal treatment and following chemical exposure. **Figure 66** shows IR spectra of UiO-66 before and after initial exposure to vacuum and subsequent heating. The elevated baseline from 3660 to 2200 cm^{-1} under ambient conditions is attributed to physisorbed solvent from synthesis, likely DMF. Initial exposure to vacuum removed a portion of the solvent, but a significant amount remained until the sample was heated. After heating to 575 K and immediately cooling back to room temperature, the signal between 3660 and 2200 cm^{-1} decreased significantly in intensity and did not decrease further with continued heating. All TPD experiments were performed after pretreating the sample with a temperature ramp to 575 K to remove the residual solvent from synthesis and any other

contaminants. Subsequent exposure to water, acetone, and repeated temperature ramps during several weeks of TPD experiments did not cause a visible change to the spectrum of UiO-66 as long as the sample was immediately cooled after reaching 575 K. XRD spectra (see **Figure 67**) collected by Frenkel et al. at Brookhaven National Lab show the excellent stability of the crystal structure of UiO-66 up to 500 K in an inert atmosphere.

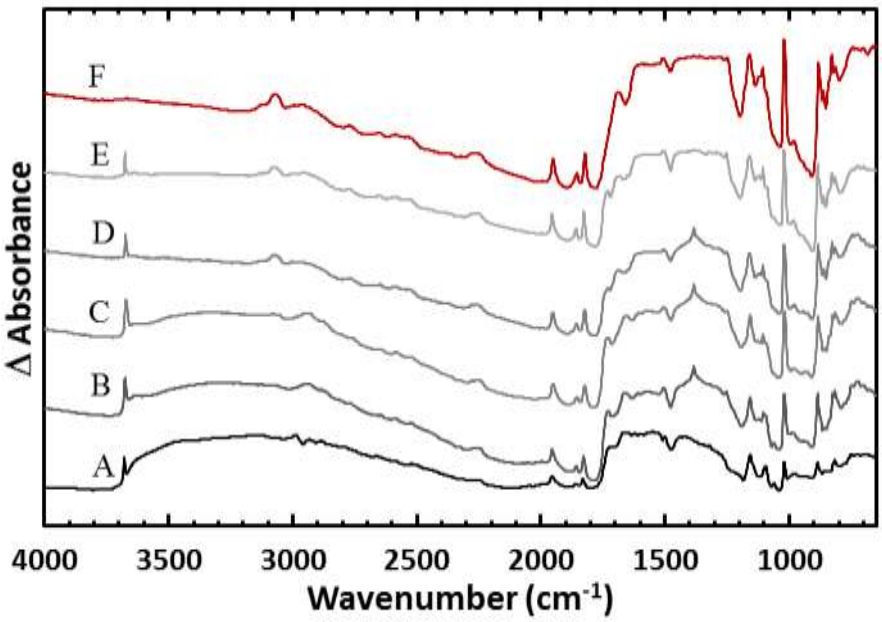

Figure 66. *IR spectra of UiO-66 after exposure to vacuum, chemicals, and high temperature. A) Ambient conditions. B) Immediately after exposure to vacuum. C) After 0.2 K/s temperature ramp 440 K. D) After 0.2 K/s temperature ramp to 575 K E) After exposure to several solvents including water and acetone. F) After overnight heating at 575 K.*

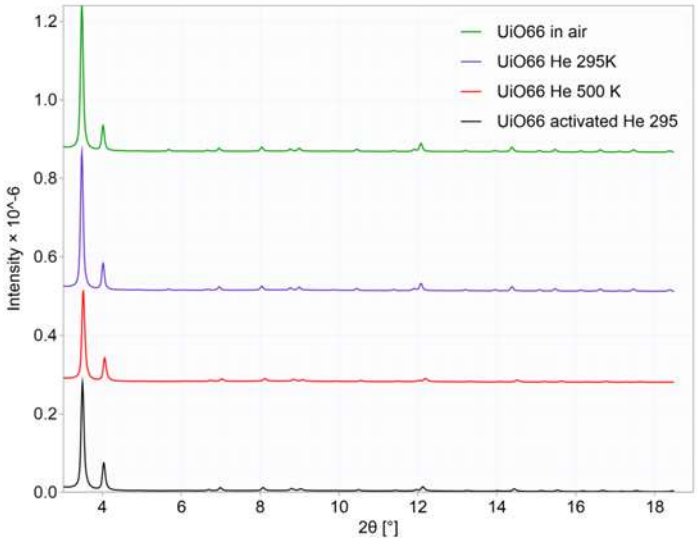

Figure 67. *XRD Spectra of UiO-66 before, during, and after exposure to 500 K for two hours in a helium flow (5 cc/min).*

Prolonged exposure to high temperature removed the hydroxyl groups from UiO-66. A sharp band centered at 3670 cm^{-1}, the expected position and shape for free O-H stretches, was present in spectra of UiO-66 under ambient conditions and remained largely unaffected by multiple brief exposures to 575 K. However, allowing the sample to remain at 575 K for several minutes caused a gradual decline in the free hydroxyl band until it was no longer present after several hours (see **Spectrum F** in **Figure 66**). The dehydroxylated UiO-66 samples studied in this chapter were prepared by overnight heating at 575 K. This procedure is in agreement with a previous manuscript that carefully characterized the structure of hydroxylated and dehydroxylated UiO-66 and demonstrated with XRD that the crystal structure of UiO-66 remains intact after heating.[73]

6.3.2 Rehydroxylation of UiO-66

Previous work has indicated that dehydroxylation of UiO-66 is a fully reversible process.[73] In that study, a dehydroxylated sample was exposed to moist air at 100% humidity to generate a hydroxylated sample. Rehydroxylation in the UHV chamber used in this work posed a technical challenge because the turbo pumps could not be exposed to pressures above high vacuum. In an

initial attempt at rehydroxylation (**Figure 68, spectrum A**), a sample was exposed to water at 10^{-6} torr near room temperature (290 K). In this experiment, the water had minimal interaction with the surface after 30 minutes. Next (**Figure 68, spectra B and C**), the sample was cooled to 175 K and exposed to water for up to 1 hour at 10^{-6} torr to create a layer of frozen water on the surface. The surface was then heated at 0.2 K/s to test if water molecules would diffuse into the pores before desorbing into vacuum and regenerate hydroxyl groups. This approach had some success, but much of the frozen water layer appeared to desorb into the gas phase without increasing the extent of hydroxylation.

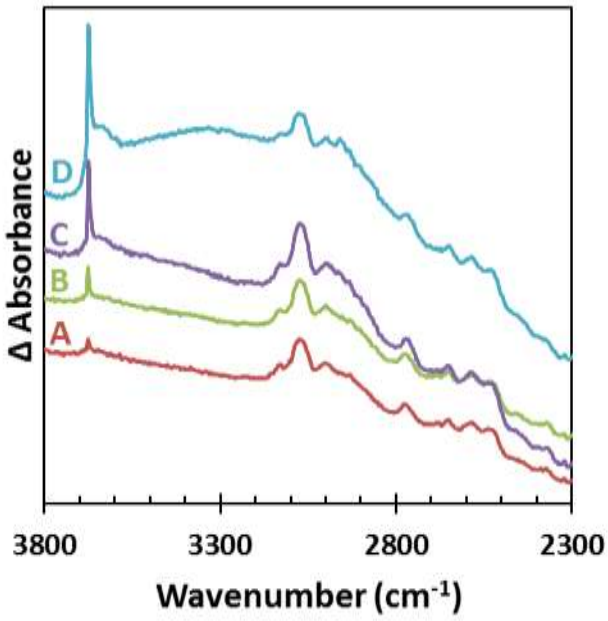

Figure 68. *Spectra of UiO-66 after several attempts at rehydroxylation. A) After exposure to water at 10^{-6} torr for 30 minutes at 290 K. B) After exposure to water at 10^{-6} torr for 30 minutes at 175 K, then heating to 475 C. C) After exposure to water at 10^{-6} torr for 1 hour at 175 K, then heating to 475 C. D) After exposure to water at 1 torr for 1 hour at room temperature.*

The lack of success at reydroxylation under vacuum drove us to devise a procedure to carefully expose a dehydroxylated sample to water at near-ambient pressures without completely venting the chamber. The mass spectrometer filament was turned off, the gate valve between the

chamber and the main turbo pump was closed to minimize the volume exposed to water, and all turbo pumps were turned off. Then the chamber was backfilled with water at its vapor pressure for up to one hour (valves in the dosing manifold described in Chapter 2 were opened to directly expose the UHV chamber to vapors from a stainless steel vial filled with water). This method (see results in **Figure 68, spectrum D**) regenerated more than double the number of hydroxyl groups (as judged by the integrated area of the free hydroxyl IR band and assuming Beer's Law) compared to the aforementioned attempts to dose under UHV conditions. One day of pump-down was required to regain sufficiently low UHV pressures before recommencing TPD studies. For comparison, 2-5 days are typically required to achieve adequate vacuum after fully venting to the ambient atmosphere.

6.3.3 Hydrogen bonding on hydroxylated UiO-66 under ambient conditions

In comparison to the silica surface studied in previous chapters, UiO-66 appears reluctant to form hydrogen bonds with small polar adsorbates under ambient conditions. As discussed in Chapter 2, freshly synthesized silica particles readily form hydrogen bonds with atmospheric gasses (mainly water) and between neighboring hydroxyl groups (for samples with sufficiently high hydroxyl coverages). Exposure to vacuum and high temperature drives off adsorbed molecules and partially dehydroxylates the sample. The consequent increase in the number of free hydroxyl groups is visible spectroscopically as an intensity increase in the band associated with free hydroxyl groups (see Chapter 2, **Figure 14**). When a freshly synthesized, fully hydroxylated UiO-66 sample is exposed to vacuum and heated, the free hydroxyl band does not increase in intensity by a noticeable amount. Thus, although heating does drive off molecules as evidenced by the decrease in absorption between 3600 and 2400 cm^{-1}, the number of free hydroxyl groups does

not appear to be affected. The molecules trapped in UiO-66 under ambient conditions are therefore likely not involved in hydrogen bonds. Furthermore, the hydroxyl groups in UiO-66 do not appear to form hydrogen bonds with each other.

The lack of hydrogen bonds between neighboring hydroxyl groups can be explained by the structure of UiO-66. Hydroxyl groups in UiO-66 are located only in the inorganic $Zr_6O_4(OH)_4$ nodes. The four hydroxyl groups are not oriented in a way that allows interactions with each other,[73] and the length of the linkers prevents hydroxyl groups on adjacent nodes from interacting with each other (see **Figure 62** above).

UiO-66 has previously been shown to behave as an effective sorbent material for water;[75] thus the absence of evidence for MOF-adsorbate hydrogen bonds ambient conditions may seem surprising. The lack of MOF-water hydrogen bonds may be due to residual solvent from synthesis, because DMF has a higher affinity for UiO-66 than water.[73] That is to say, water may not be able to adsorb to an unactivated sample of UiO-66. The spectra of UiO-66 under ambient conditions presented in **Figure 68** were collected before thermal activation to remove the solvent molecules (DMF in this case) that occupy the pores of UiO-66 after synthesis. However, the presence of DMF is not a satisfactory explanation for the lack of MOF-adsorbate hydrogen bonds because the carbonyl group in DMF should also behave as a hydrogen bond acceptor.

Adsorption mechanisms other than hydrogen bonding must be considered for molecules such as water and DMF that are small enough to diffuse throughout the pores of a MOF. As will be discussed in a later section, dispersion forces play an important role in uptake within UiO-66 and may provide a similar binding energy as a single hydrogen bond even for a small molecule such as water or DMF. The Zr metal centers, which are strongly acidic, also play an important role. A computational study of CO_2 and CH_4 uptake on UiO-66 investigated the binding energies

of both molecules to hydroxyl, ester oxygen, and defect sites on a simulated Zr_8 metal center designed to mimic the inorganic $Zr_6O_4(OH)_4$ nodes in UiO-66.[74] For both adsorbates, the binding energy on hydroxyl sites was only slightly higher than on undercoordinated Zr sites (24.8 versus 22.3 kJ/mol for CH_4 and 29.9 versus 22.4 kJ/mol for CO_2). This result can be interpreted as evidence that binding energies to hydroxyl groups and metal centers are similar.

On a perfect sample of UiO-66 with no defects, the binding energy to undercoordinated Zr sites would not be possible. However, studies have reported that UiO-66 samples often have fewer than the expected 12 linkers per node.[54,73,74] A typical sample may have 11 or fewer linkers per node, and therefore at least one Zr site per node available for adsorption. XRD patterns collected on the UiO-66 sample employed in our work indicate that they also contain a significant number of missing-linker defects. Hydrogen bonds are sensitive to orientation and are unlikely to form if the donor and acceptor groups are beyond 0.4 nm apart.[24,26] Therefore, a water or solvent molecule bound by dispersion forces or an electrostatic interaction with a metal center may not be oriented in the correct way to form a hydrogen bond with one of the inorganic nodes. The lack of spectroscopic evidence of MOF-adsorbate hydrogen bonding under ambient conditions combined with the elevated baseline are evidence that dispersion forces may play a larger role than hydrogen bond formation in the uptake mechanism for small polar molecules on UiO-66. Any hydrogen bonds in the MOF under ambient conditions that contribute to the elevated baseline are likely from small adsorbate clusters (e.g. DMF-water or water-water) inside the pores.

6.3.4 2-CEES – UiO-66 hydrogen-bond formation

Unlike uptake of water and DMF, 2-CEES uptake on hydroxylated UiO-66 causes the formation of hydrogen bonds with hydroxyl groups (Zr-OH) in the metal oxide nodes. Evidence

of these hydrogen bonds is visible in spectra of 2-CEES (**Figure 69**) where the free OH band at 3670 cm^{-1} decreases in intensity as a broad band centered at 3558 cm^{-1} emerges. This band is in the IR spectral range associated with the hydroxyl O-H stretch, but is redshifted from the free hydroxyl band. As discussed in previous chapters, the vibrational energy of the hydroxyl O–H bond is highly sensitive to the formation of hydrogen bonds. Charge transfer between the OH groups and the electron lone pairs of hydrogen bond acceptor increases occupation of the O–H lowest energy unoccupied molecular orbital, the σ* orbital, and thus weakens the O–H bond. IR spectroscopy detects this reduction in bond order as a redshift in the hydroxyl absorption band. The magnitude of the shift is directly correlated to the extent of charge transfer, as discussed in previous chapters and elsewhere in the literature.[43,102] Therefore, IR spectroscopy serves as a probe of the extent of charge transfer in MOF-adsorbate hydrogen bonds.

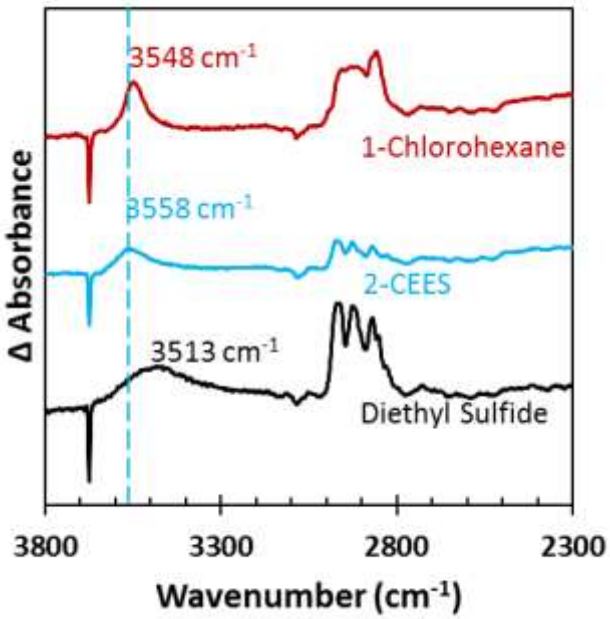

Figure 69. *IR spectra of adsorbed 1-chlorohexane, 2-CEES, and diethyl sulfide. Note the similarities in wavenumber for the OH stretch (H-bonded) for 2-CEES and 1-chlorohexane binding.*

The polar, electron-rich chloro and thioether moieties in 2-CEES can both potentially behave as hydrogen-bond acceptors when paired with surface hydroxyls. Our studies of 2-CEES uptake on silica, which are reported in Chapter 3, revealed the presence of two distinct IR bands in the wavenumber range associated with hydrogen-bonded O-H vibrations. Spectra of diethyl sulfide and 1-chlorobutane adsorbed on silica (see **Figure 70**) provided evidence that the low and high wavenumber bands in spectra of 2-CEES on silica were associated with Cl···H–O and S···H–O hydrogen bonds respectively. Thus, in that case, both the chloro and thioether moieties in 2-CEES were found to form hydrogen bonds with silanol groups, and these interactions appeared to have similar strengths in TPD studies.

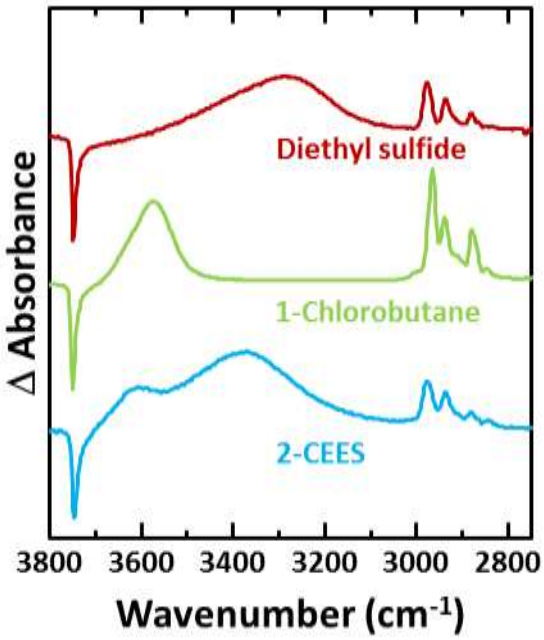

Figure 70. *Infrared spectra of adsorbed diethyl sulfide (top, red), 1-chlorobutane (middle, green), and 2-CEES (bottom, blue) on silica.*

Here, on UiO-66, the OH region in spectra of adsorbed 2-CEES only displays one broad IR band centered at 3558 cm^{-1}. We studied the uptake of diethyl sulfide and 1-chlorohexane to better understand how Cl···H–O and S···H–O hydrogen bonds affect the vibrational frequency of the H–O bond in UiO-66. Spectra of adsorbed diethyl sulfide (see **Figure 69**) display a broad band at 3513 cm^{-1}. A well-defined band or shoulder is not visible in this region in spectra of adsorbed 2-CEES. The band associated with the OH bond in spectra of 1-chlorohexane on UiO-66 is centered at 3548 cm^{-1}, which is close to the 3558 cm^{-1} 2-CEES band. The 10 cm^{-1} difference is consistent with work in Chapter 3, which provided evidence that the extent of charge transfer in a chloroalkane Cl···H–O hydrogen bond is higher than in the 2-CEES Cl···H–O hydrogen bond. Therefore, the 3558 cm^{-1} band in the spectrum of 2-CEES is likely due largely to the formation of Cl···H–O hydrogen bonds

It must be noted that the bands for Cl and S hydrogen bonds in 1-chlorohexane and diethyl sulfide have some overlap. Therefore, the possibility of S···H–O hydrogen bonds in adsorbed 2-CEES cannot be completely dismissed. It is possible that the extent of redshift for bonding through the thioether group of 2-CEES is much smaller than our prediction based on spectra of diethyl sulfide and small enough to allow the Cl···H–O and S···H–O bands to be indistinguishable in spectra of adsorbed 2-CEES. Future computational work may be able to provide further insight into the role of S···H–O hydrogen bonds in 2-CEES uptake on UiO-66.

The IR signatures of hydrogen bonding in spectra of adsorbed 2-CEES, diethyl sulfide, and 1-chlorohexane provide evidence that these molecules were all able to access adsorption sites inside the pores of UiO-66. Hydroxyl groups in UiO-66 are part of the inorganic $Zr_6O_4(OH)_4$ nodes. Some of these nodes may be exposed to the exterior surface of individual MOF particles, but the majority are expected to reside inside of pores. Transmission IR spectroscopy of UiO-66 powder mounted in mesh cannot differentiate between hydroxyl groups on the surface and inside pores. Exposing hydroxylated UiO-66 to 2-CEES, diethyl sulfide, or 1-chlorohexane eventually causes full saturation of the hydroxyl groups, as evidenced by complete conversion of the free OH IR band to a hydrogen bonded IR feature. Therefore, we concluded that these molecules are small enough to thoroughly permeate UiO-66 and travel through the pores. The interpretation that chloroakanes diffuse into the pores is supported by other work in our group. We have demonstrated that larger molecules, such as dimethyl methyl phosphonate (DMMP), which is an excellent hydrogen bond acceptor, occupy only 10% of the free hydroxyl groups during exposure. Therefore, we estimate that nearly 90% of the free hydroxyl groups reside inside of the MOF pores.

The infrared spectral assignments above reveal that the formation of hydrogen bonds is important for uptake of 2-CEES on hydroxylated UiO-66. However, this does not assess the

possibility of other contributions to the overall uptake mechanisms. The same forces that drive uptake of water and DMF without the formation of MOF-adsorbate hydrogen bonds may also have an important effect on uptake of 2-CEES. To test this, we performed a series of TPD studies on both hydroxylated and dehydroxylated samples of UiO-66 in order to determine the overall energy required to rupture all adsorbate-MOF interactions and drive molecules from the surface.

6.3.5 Effects of dispersion forces on chloroalkane uptake

Mass spectra collected during desorption of 2-CEES from dehydroxylated UiO-66 indicate molecular adsorption without significant reaction or decomposition. The relative intensities of the various mass fragments in a scan collected during a TPD experiment are similar to those in a NIST[120] mass spectrum of pure 2-CEES. A similar comparison was not performed for chloroalkanes because their reactivity is much lower than 2-CEES (a reactive electrophilic agent),[133] and they are likely very stable within the MOF under the conditions used for the TPD experiments. Furthermore, XPS analysis of UiO-66 samples after exposure to 2-CEES and other chloroalkanes demonstrate that minimal Cl remains in the material after the completion of UiO-66 experiments.

In the absence of hydroxyl groups available for hydrogen-bonding interactions on dehydroxylated UiO-66 (see **Figure 71** for spectra of dehydroxylated UiO-66 before and after 1-chlorobutane uptake), dispersion interactions are likely the primary driving force for uptake. The total strength of dispersion forces per molecule is known to increase proportionally with the size of straight-chain adsorbates. For example, others have shown a ~3-5 kJ/mol energy gain in binding energy per methylene unit for desorption of linear alkanes from metal oxides.[47] Also, in Chapter 3, we demonstrated a 5 kJ/mol increase in dispersion forces per methylene unit for linear chloroalkanes from silica. Similar measurements have not yet been performed on a MOF to the best of our knowledge. Therefore, we performed TPD analysis for linear chloroalkanes on dehydroxylated UiO-66 to investigate if the same trend between desorption energy and adsorbate chain length is observed on a MOF. Preliminary results from these experiments are provided in **Figure 72**, which shows plots of desorption rate versus temperature for chloroethane, 1-chloropropane, 1-chlorobutane, 1-chloropentane, and 1-chlorohexane from dehydroxylated UiO-66.

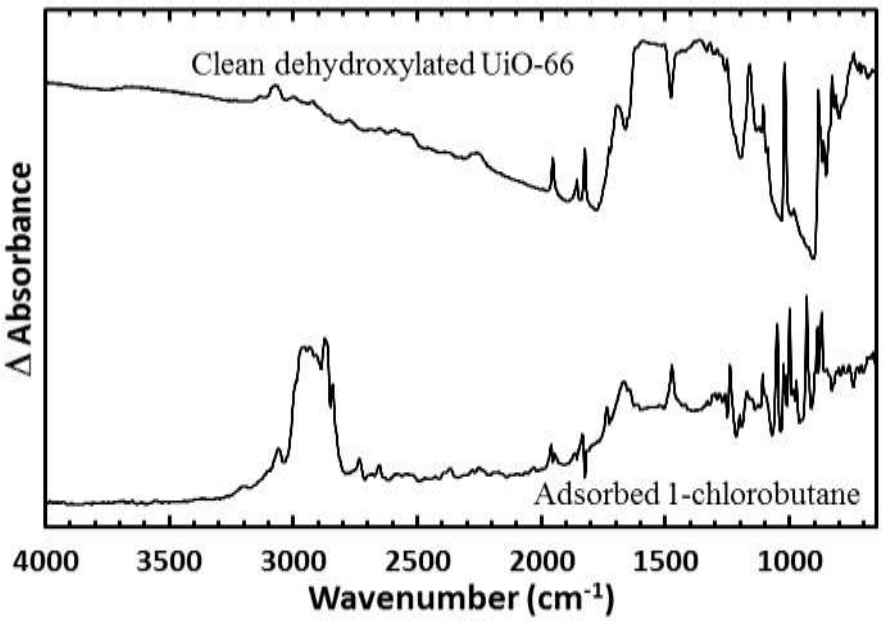

Figure 71. *IR spectra of clean dehydroxylated UiO-66 (top) and 1-chlorobutane adsorbed on dehydroxylated UiO-66 (bottom)*

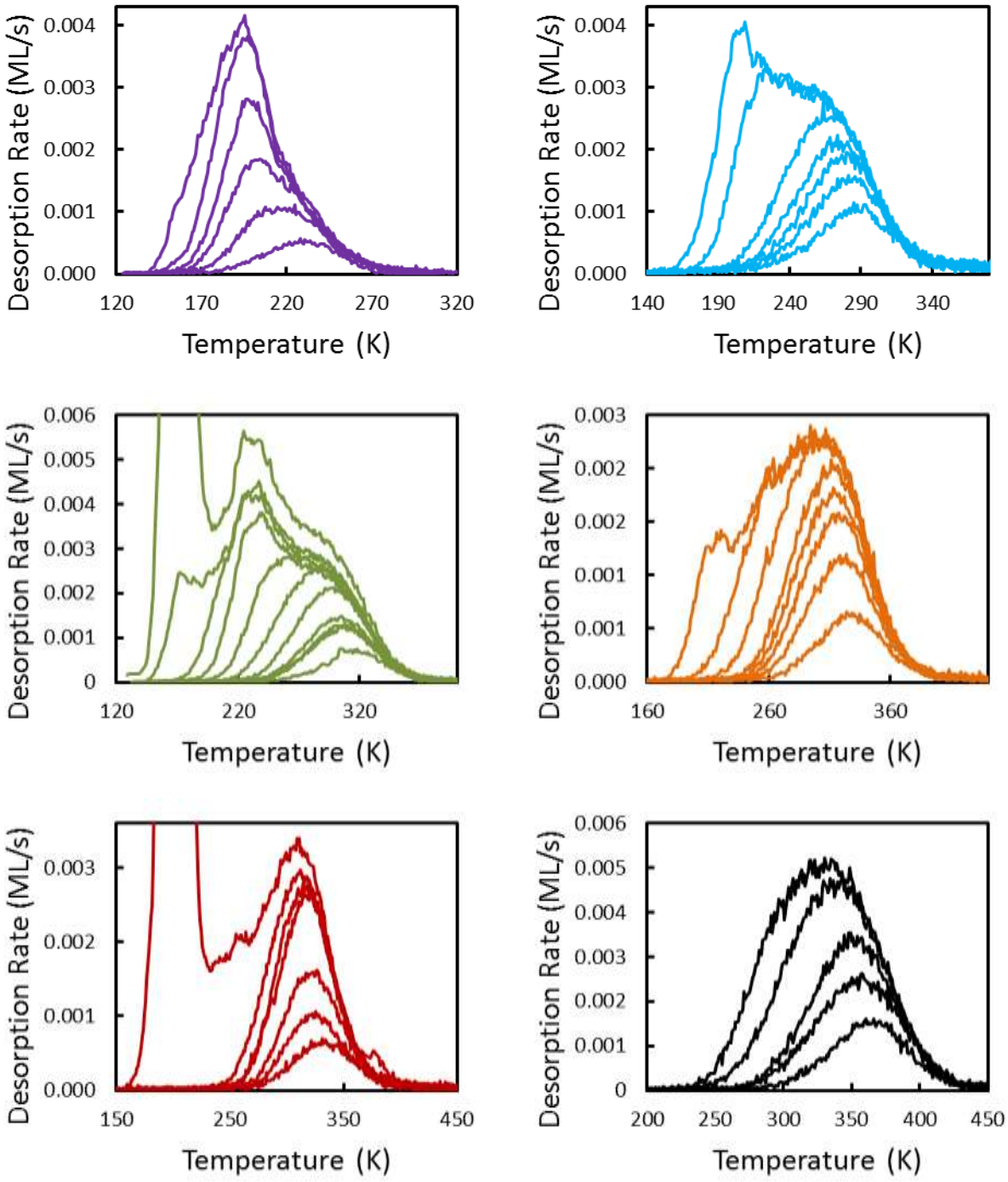

Figure 72. *Plots of desorption rate versus temperature for chloroethane (purple) 1-chloropropane (blue), 1-chlorobutane (green), 1-chloropentane (orange), and 1-chlorohexane (red) on*

dehydroxylated UiO-66.Plots of desorption rate versus temperature for 2-CEES on hydroxylated UiO-66

Inversion analysis of the high-temperature TPD data reveals a correlation between alkane chain length and binding energy similar to the trends observed on other surfaces. Plots of desorption energy as a function of coverage for each molecule tested are shown in **Figure 73**. Each molecule was tested multiple times on two different samples in order to determine the reproducibility of our results. The desorption energy in the limit of zero coverage for each test was calculated individually. **Table 15** lists the average zero-limit desorption energy for each molecule. The standard deviation of the zero-limit desorption energies from five different 1-chloropentane tests was used to quantify the worst-case error of replicate measurements. The large variations observed in the data reflect the preliminary nature of these results. The mass spectrometer data used for the lower energy 1-chlorohexane result had a noisy mass spectrometer signal due to poor alignment, but were not discarded for the sake of completeness. Further work is needed to fully understand the source of the large variations observed in the energies measured for the other chloroalkanes.

Table 15. *Desorption energies and pre exponential factors for all molecules tested in this chapter. Error values are ± one standard deviation calculated from four separate 1-chloropentane TPD experiments.*

Adsorbate	Surface	E_d (± 5.7 kJ/mol)	log(ν) (± 0.7)
Chloroethane	Dehydroxylated	26.9	8.4
1-Chloropropane	Dehydroxylated	36.0	8.6
1-Chlorobutane	Dehydroxylated	38.3	6.0
1-Chloropentane	Dehydroxylated	43.1	8.4
1-Chlorohexane	Dehydroxylated	46.5	8.3
2-CEES	Hydroxylated	49.2	8.5

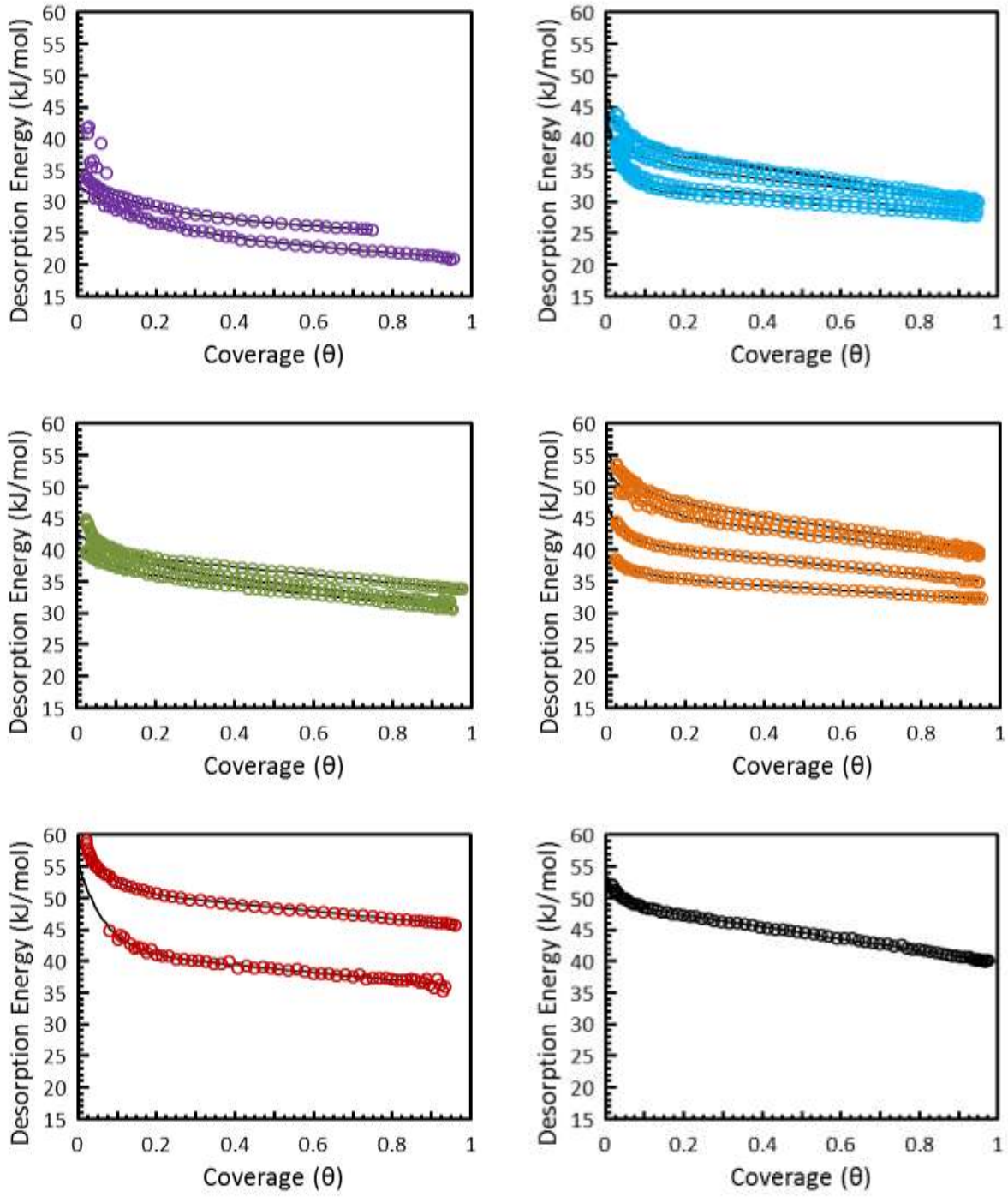

Figure 73. *Plots of desorption energy versus coverage for the following systems from left to right, bottom to top: chloroethane (purple) 1-chloropropane (blue), 1-chlorobutane (green),*

1-chloropentane (orange) and 1-chlorohexane (red) from dehydroxylated UiO-66; 2-CEES (black) from hydroxylated UiO-66

Even with the large standard deviation for replicate measurements, the effect of increasing the hydrocarbon chain length appears to be a proportional increase in desorption energy for the series of chloroalakanes tested here. A plot of desorption energies as a function of alkyl chain length is provided in **Figure 74** . In **Figure 75**, the temperature at which desorption rate was highest for an initial coverage of $\theta = 1$ for each molecule is plotted against alkyl chain length. In both figures, the interaction strength of the linear alkanes on dehydroxylated UiO-66 generally increases proportionally with chain length. Dispersion forces are likely the main surface-adsorbate interaction in this system. Therefore, the increase in binding energy with adsorbate chain length can be attributed to an increase in the total energy of the dispersion forces with additional methylene groups in agreement with previous work on other surfaces discussed in Chapter 3 and elsewhere in the literature.[47,134]

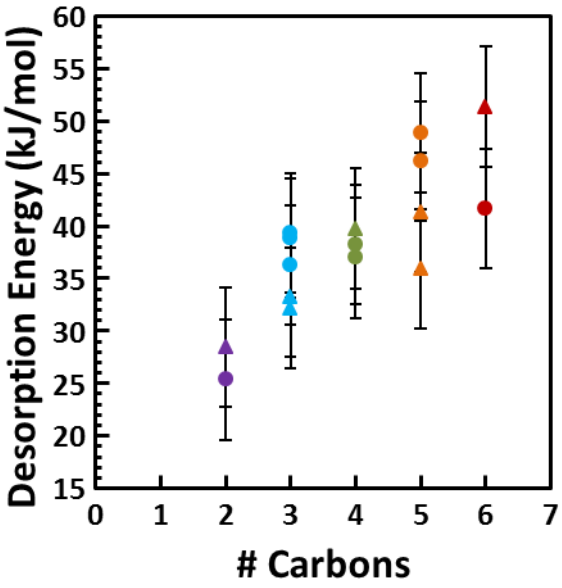

Figure 74. *Plot of desorption energies of linear chloroalkanes versus alkyl chain length. The circles and triangles represent data from two different UiO-66 samples. Error bars are the standard deviation of replicate runs of 1-chloropentane, which had the poorest reproducibility of all molecules included in this figure.*

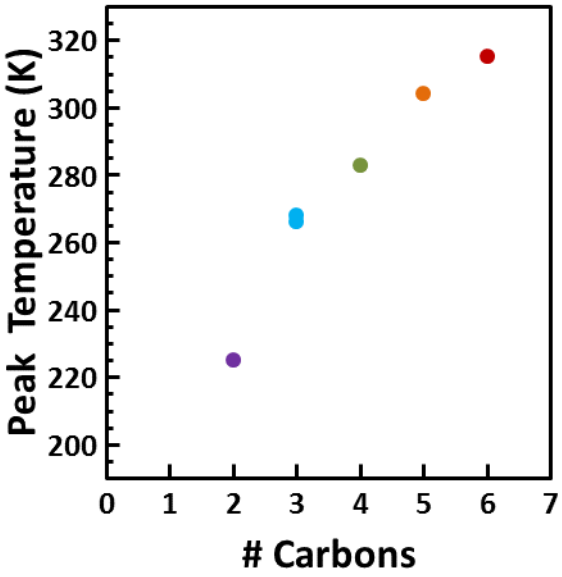

Figure 75. *Plot of the temperature at which desorption rate was highest for an initial coverage of $\theta = 1$ for each molecule versus alkyl chain length.*

The TPD results indicate that multiple types of binding mechanisms are likely associated with uptake of chloroalkanes on dehydroxylated UiO-66. TPD plots for all molecules in **Figure 72** except chloroethane display low-temperature features that do not align on the trailing, high temperature edge. Rather, the maximum desorption energy is observed at the same temperature regardless of initial coverage. This alignment is characteristic of first order desorption with either a narrow distribution of binding site energies or a lack of sufficient mobility for the adsorbates to diffuse to the strongest available binding sites before desorption.[94] Leading edge analysis was used to determine the desorption energy of the molecules that left the surface during the lowest-temperature peak for each molecule. In Chapter 2 and in previous work, leading edge analysis of zero-order TPD data yielded values nearly equivalent to the sublimation energies of the adsorbates. That is to say, as expected, the desorption energies in those instances were representative of breaking adsorbate-adsorbate interactions from multilayers. Here, for desorption of chloroalkanes from UiO-66, the results of leading edge analysis for data with initial coverages beyond saturation are consistently ca. 15 kJ/mol lower than the literature values for sublimation energies and also somewhat lower that the desorption energies measured for each molecule. Therefore, the molecules that desorb first likely do not come from multilayers and also do not share the same binding mechanism as the molecules that desorb later.

The presence of multiple types of desorption energies for simple chloroalkanes on UiO-66 clearly illustrates the complexity of the surface. Initial uptake appears to be driven by the formation of MOF-adsorbate interactions in a similar way as uptake on silica. Further adsorption occurs on sites where only weaker bonds form. While the data collected for this work do not provide a complete understanding of the uptake mechanism, especially for the molecules associated with the low-temperature TPD peak, dispersion forces between adsorbates and the MOF likely play a major

role for uptake of the initial molecules. Subsequent adsorption may be driven by weaker interactions with the MOF or by the formation of weak interactions with adsorbates already on the surface. The low binding energies measured in this work compared to the sublimation energies indicate that the formation of islands and multilayers of adsorbates may be restricted despite being more energetically favorable than adsorption to the MOF. One explanation is that the sublimation energy reflects the energy needed for a single molecule to leave an extended network of like molecules, and is higher than the dimerization energy. For example, the dimerization and sublimation energies for water have been reported as 13 and 51 kJ/mol respectively. Thus the interaction energy for a single molecule with the MOF is stronger than the interaction energy for two single molecules with each other. The dimensions of the pores may also help restrict the formation of multilayers.

Dehydroxylation appears to have minimal effect on the amount of uptake. The spectra in **Figure 76** show 1-chlorohexane adsorbed on both hydroxylated and dehydroxylated samples at similar temperatures (ca. 150 K). These spectra have been normalized to account for differences in instrument sensitivity and amount of UiO-66 in the IR beam path. They have also been normalized to represent the same θ value where $\theta = 1$ is defined as full occupation of hydroxyl groups for the hydroxylated sample and as saturation of the high-energy binding sites for dehydroxylated samples. With these adjustments, the intensities of the IR bands assigned to C-H stretches in 1-chlorobutane do not appear to be sensitive to the extent of hydroxylation of the surface. Therefore, as the intensity of an IR band is directly proportional to the amount of species, we conclude that hydroxylated and dehydroxylated UiO-66 have similar capacities for chloroalkane uptake.

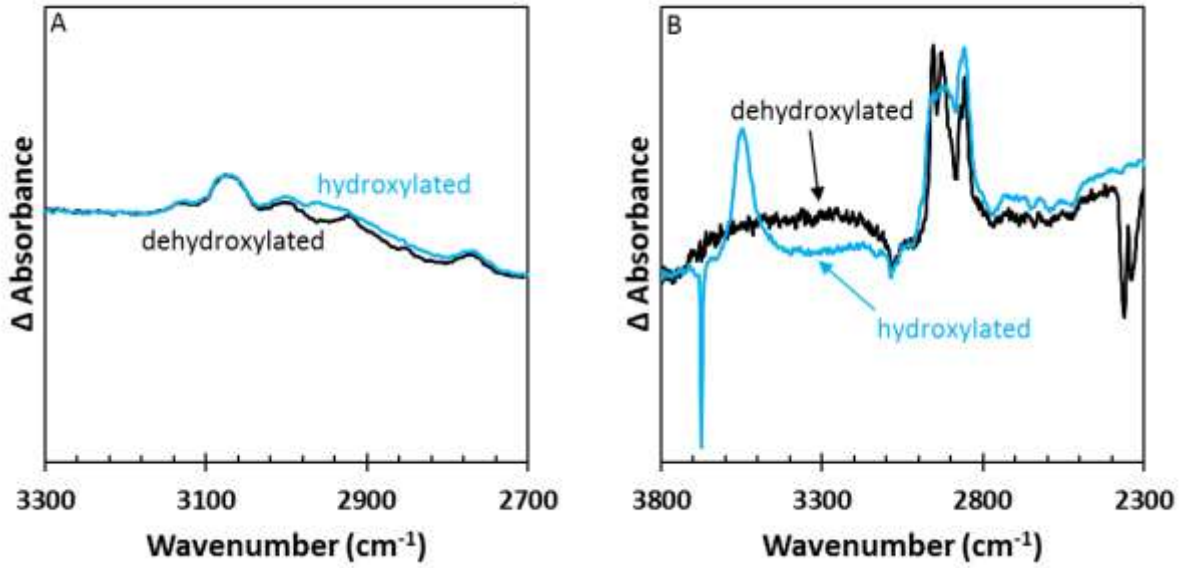

Figure 76. *A) Spectra of hydroxylated and dehydroxylated UiO-66 normalized such that the intensities of the bands for bulk modes are similar. Both spectra use a clean spot on the mesh as a reference background. The spectrum of hydroxylated UiO-66 has been multiplied by a factor of 1.25 to account for differences in instrument sensitivity and amount of sample B). Spectra of 1-chlorohexane on a dehydroxylated sample at a coverage of 26% saturation and on a hydroxylated sample at a coverage of 72% saturation. The spectra have been normalized to account for the differences in percent saturation, amount of sample, and instrument sensitivity.*

6.3.6 Comparison of 2-CEES uptake on UiO-66 and silica

Finally, we have measured the activation energy for desorption of 2-CEES from hydroxylated UiO-66. Inversion analysis of the TPD yields a result of 49.2 ± 5.7 kJ/mol. This is a higher energy than for any of the chloroalkanes on dehydroxylated UiO-66, but not by a large margin. Specifically, 2-CEES requires an extra 11 kJ/mol for desorption than 1-chlorobutane, a molecule expected to have a similar amount of dispersion interactions. To put this value in perspective, consider that the difference in binding energies for these same molecules on silica is 9 kJ/mol. Unfortunately, the necessary TPD data to directly compare chloroalkane versus 2-CEES on hydroxylated and dehydroxylated UiO-66 has not yet been collected. However, the trend in the data that was collected strongly suggests that the binding energy for 2-CEES on dehydroxylated

UiO-66 would also be near 49 kJ/mol. The lack of hydrogen bonding sites on dehydroxylated UiO-66 appears to have minimal effect on not only the amount of adsorbed molecules but also the binding energy.

6.4 Summary

In this chapter, we performed TPD and IR measurements designed to characterize uptake of HD simulants on UiO-66. The results provided evidence that uptake of 2-CEES on UiO-66 is driven by a combination of MOF-adsorbate forces. Hydrogen bonds, mainly of the type Cl···H–OH, appeared to play an important role for uptake on hydroxylated UiO-66. Uptake on dehydroxylated UiO-66 may be driven in part by interactions with undercoordinated Zr sites at missing-linker inorganic nodes. Dispersion forces provided additional contributions to the desorption energy on dehydroxylated UiO-66, and the same is likely true for hydroxylated UiO-66. Despite the difference in uptake mechanisms, the number of adsorption sites and desorption energies appeared to be similar for the hydroxylated and dehydroxylated forms of UiO-66. Spectroscopic evidence showed that all molecules tested in this chapter were able to access adsorption sites inside of pores with no restrictions detectable by the analytical techniques used here. Based on the results in this chapter, we predict that UiO-66 has potential as a sorbent material for HD, which is structurally similar to 2-CEES.

The TPD and transmission IR measurements performed in this chapter were the first of their kind on a MOF and were therefore preliminary. Future work will be needed to verify the results and conclusions provided here. In particular, experiments performed by other members of the Morris group indicate that diffusion of adsorbates through the pores may affect the results of TPD measurements in a way that is not accounted for by the inversion analysis used here.

Experiments are in progress to further explore these diffusion effects and determine if they have a significant effect on TPD analysis. Also, additional experiments will seek to address the large standard deviation among binding energies and prefactors measured in replicate TPD experiments. Finally, further work will explore the nature of surface-adsorbate interactions on other MOFs closely related to UiO-66 such as UiO-67 and NU-1000. These experiments will be designed to investigate how the larger pore sizes in these systems affect binding energies and diffusion rates.

Chapter 7: Conclusions

7.0 Summary of findings

The primary objective for the research described in this thesis was to undertake fundamental studies of the interfacial hydrogen bonds and dispersion interactions that drive the uptake of sulfur mustard (HD), mustard simulants, and other similar small molecules. This knowledge is important for the development of new materials to protect personnel from exposure to HD and decontaminate areas after an attack. Initial studies investigated uptake on silica as a simple, well-characterized material that is highly relevant to the environmental fate of HD due to its abundance in nature. Later experiments examined uptake on UiO-66, a metal-organic framework (MOF) that is known to bind and break down CWA molecules. Although hydrogen bonding is arguably the most important reversible force in surface science, there are few studies of hydrogen bonding at the gas-surface interface. Together with previous work in the Morris group,[83] this thesis provides the most comprehensive experimental study of interfacial hydrogen bonding to date.

Researchers often use simulants to mimic the physical or chemical properties of live agent with lower toxicity. However, the effects of the differences in molecular structure on hydrogen bonding are not well understood. Hydrogen bonding is important for initiating catalysis and predicting environmental fate. Furthermore, insight into the molecular geometries of both simulants and live agent molecules can help researchers make a more informed assessment about the suitability of a simulant for a given experiment. Therefore, we designed a series of experiments to investigate how each moiety in methyl salicylate and 2-CEES, two of the most commonly used HD simulants hydrogen bonds to silica. Silica was chosen because: (1) it is a good model surface that can be reproducibly made; (2) previous theory provides a wealth of information about its structure and properties; and (3) it is highly relevant from the perspective of environmental studies and catalysis. Moreover, results for methyl salicylate and 2-CEES on silica were directly compared to results of live agent on silica provided by collaborators to identify similarities and differences. Beyond simple simulant-agent comparisons, our methods provided a deeper understanding of the fundamental nature of interfacial hydrogen bonds and dispersion forces that are critically important to many facets of surface science.

All experiments were conducted in an ultra-high vacuum (UHV) chamber to maintain excellent control over the surface and adsorbates during the experiment. UHV is also an experimental requirement for the mass spectrometer measurements that were performed during this work. An existing UHV chamber was modified to conduct temperature programmed desorption experiments for weakly bound molecules on silica and thus measure their desorption energy. The design and testing of these modifications along with the development of new experimental procedures comprised a significant portion of the work performed for this thesis. Additional adjustments were made to the instrument and procedures to investigate the desorption

of weakly bound molecules from the metal-organic framework (MOF) UiO-66. Infrared spectroscopy was used to characterize surface-adsorbate hydrogen bonds and was a critical component of experiments because it reported on both the surface concentration and binding mechanism of adsorbates. As IR spectroscopy is non-destructive, it could be performed in situ with uptake and desorption experiments. Together, IR spectroscopy and TPD measurements were used to accomplish several key research goals. Among the other achievements described in detail below, we: (1) explored the interplay between the charge transfer and electrostatic components of hydrogen bonds; (2) established a correlation between chain length and dispersive binding forces for linear chloroalkanes on both silica and UiO-66; and (3) found evidence that 2-CEES, and likely also HD, is small enough to diffuse throughout the bulk of UiO-66.

We found that the uptake of 2-CEES on silica is driven primarily by the formation of hydrogen bonds to the thioether and chloro moieties. Although both types of hydrogen bonds have similar overall strengths, the contributions to bond strength from charge transfer and other forces are different. Specifically, the S···H–OSi bond has a larger charge transfer contribution, and the Cl···H–OSi bond has a larger contribution from other intermolecular forces including electrostatics. Dispersion forces between the hydrocarbon segments of the adsorbed molecules and surface atoms provide additional stabilization of ca 5 kJ/mol per CH_2. Although the sulfur and chlorine atoms have sufficient spacing to span adjacent silanol groups, each adsorbed 2-CEES molecule occupies a single silanol group in a 1:1 bonding motif.

Based on our results and data provided by collaborators at ECBC, we predict that mustard gas binds to silica with a similar mechanism as 2-CEES; namely, with Cl···H–OSi and Cl···H–OSi hydrogen bonds plus other weak surface-adsorbate interactions that may be as strong as 45 kJ/mol overall. This result is significant because hydrogen bonding is critical to the environmental

transport of this highly toxic CWA as it strongly influences uptake prior to subsequent diffusion into the bulk of materials or reaction on the surface of catalytic materials. Our results on silica are particularly relevant because sand is ubiquitous in the environment, and silica is a common component of many artificial materials including polymeric coatings. Future work may provide further insight into the ratio of molecules bound by Cl···H–OSi versus Cl···H–OSi hydrogen bonds. Future work may also investigate mixed catalysts where silanol hydrogen bonds may help sequester the molecules for catalytic decomposition.

Several new insights emerged from our study of the forces involved in uptake of methyl salicylate on a hydrogen-bonding surface. The carbonyl and hydroxyl moieties both appear to accept hydrogen bonds from surface silanol groups with a fraction of the molecules bound by the carbonyl group and the remainder by the hydroxyl group. Neither spectroscopic or TPD data were able to differentiate between carbonyl---silanol and hydroxyl---silanol hydrogen bonds; these interactions likely have similar strengths. The internal hydrogen bond present in gas-phase methyl salicylate may break in favor of an adsorbate---surface hydrogen bond. Alternatively, the internal hydrogen bond may persist while the carbonyl forms a second hydrogen bond with the surface. The aromatic ring, although a viable hydrogen bond acceptor as shown by the uptake of benzene, m-cresol, and benzaldehyde, does not appear to be significantly involved in uptake of methyl salicylate. The role of the ether group was not assessed in this study. The IR mode that could be used to probe the presence or absence of hydrogen bond effects on the ether is near 780 cm^{-1}, which is part of the region obscured by intense IR absorption bands caused by the bulk vibrational modes of silica. A future study of aromatic ethers or a comparison of acetone to dimethyl ether could reveal further information about the ether oxygen atom in methyl salicylate.

Compared to 2-CEES and HD, methyl salicylate has a marginally higher desorption energy from silica (49.2 versus 44.9 kJ/mol), and a similar prefactor (7.6 versus 8.4). 2-CEES remains the preferred simulant molecule for many fundamental surface studies of HD due to its similarity in structure. However, our results indicate that methyl salicylate may also be a reasonable HD simulant to study processes strongly influenced by the strength of surface-adsorbate interactions.

Our investigation into the role of π hydrogen bonds in methyl salicylate adsorption motivated additional experiments to learn more about how this type of interaction is affected by substituents on the aromatic system. We found that the uptake of benzene and substituted benzene derivatives on silica is driven by a combination of SiO–H---π hydrogen bonds and surface-substituent dispersion forces. The extent of charge transfer in the hydrogen bonds correlates well with the electron donating and withdrawing nature of the substituents. However, the extent of charge transfer does not correlate well with the desorption energies when the substituents are not similar. The activation energies for desorption for benzene, toluene, and p-xylene increase from 31.0 to 44.9 kJ/mol across this series. The activation energies for desorption of the aryl halides increase from 33.6 to 47.2 kJ/mol in the order fluoro-, chloro-, bromo-, and iodobenzene. Although the SiO–H---π bonds for all of the aryl halides appear to be weaker than for benzene, we hypothesize that their desorption energies are higher largely due to interactions between the electron-rich halogen atoms and the surface. Thus, we suggest that these two trends are offset from each other by dispersion forces, which are significantly stronger for halogen substituents than methyl substituents.

The capstone study for my research involved extending the TPD method to more complex systems that have been shown to be catalytically active for the decomposition of CWAs. Interestingly, the work described above for silica provided an important framework for

understanding chemistry on the MOFs because hydrogen bonding also plays a key role in uptake, diffusion, and desorption. We found that uptake of 2-CEES on UiO-66 is driven by a combination of different MOF-adsorbate forces. The formation of hydrogen bonds, mainly of the type Cl···H–OH, plays an important role for uptake on hydroxylated samples. Uptake on dehydroxylated samples may be driven in part by interactions with uncoordinated Zr sites at missing-linker inorganic nodes. Dispersion forces provide additional contributions to the desorption energy on dehydroxylated UiO-66, and the same is likely true for hydroxylated UiO-66. Despite the difference in uptake mechanisms, desorption energies and the number of adsorption sites appear to be similar for the hydroxylated and dehydroxylated forms of UiO-66. Spectroscopic evidence shows that linear chloroalkanes and thioethers were able to access adsorption sites inside of pores with no restrictions detectable by the analytical techniques used. Based on these results, we predict that UiO-66 has potential as a sorbent material for HD, which is structurally similar to 2-CEES. Perhaps most importantly, we have demonstrated that UHV-based TPD methods, coupled with infrared spectroscopy, can be effectively employed to study gas-MOF interactions. This experience will serve as a stepping-stone for future work in MOF-based catalysis, which our group is currently pursuing.

An important goal of this thesis was to investigate surface hydrogen bonding from a fresh perspective that is emerging from related gas and solution phase studies. The classical perspective often taught in textbooks depicts hydrogen bonds as a mainly electrostatic interaction between a donor and acceptor pair. Recent work has demonstrated the importance of charge transfer and dispersion forces in gas and solution phase hydrogen bonds. In fact, a revision to the IUPAC definition that explicitly includes contributions from charge transfer and dispersion has been proposed. However, these types of studies had not yet been performed at the gas-surface interface

to the best of our knowledge. Here, we have investigated the nature of SiOH---π, SiOH---Cl, SiOH---S, SiOH---HO, SiOH---O=C bonds on silica along with OH---Cl and OH---S hydrogen bonds on UiO-66.

In agreement with the recent work in the gas and solution phases, the results in this thesis clearly illustrate that surface hydrogen bond energy is comprised of contributions from charge transfer and electrostatics.[25,35,124,135] In the case of similar hydrogen bonds, such as the SiOH---π interaction for substituted benzene derivatives, the extent of charge transfer correlates well with the total strength of the hydrogen bond. However, in the case of dissimilar hydrogen bonds such as SiOH---Cl and SiOH---S, differences in the extent of charge transfer are a poor predictor for total hydrogen bond strength. Furthermore, dispersion forces between the surface and regions other than the hydrogen bond acceptor moiety in the adsorbate can enhance the total binding energy by more than 5 kJ/mol for a methylene unit and up to 15 kJ/mol for a halide moiety. These examples all serve to support the emerging realization that, in the words of Frank Weinhold, "The forces involved in the formation of a hydrogen bond include those of an electrostatic origin, those arising from charge transfer between the donor and acceptor leading to partial covalent bond formation between H and Y, and those originating from dispersion".[124] Therefore, a high-level discussion of surface hydrogen bonding must address all three (charge transfer, electrostatic, and dispersion) components along with any other substituent-surface interactions that may further enhance the overall activation energy for desorption.

7.1 Future work

Future work in the Morris group will continue to investigate uptake of CWA simulants on MOFs. Experiments are already in progress to characterize uptake of HD simulants on MOFs with

larger pore openings than UiO-66 such as UiO-67 and NU-1000. These materials are expected to bind larger volumes of gas molecules, but the difference in binding energy is unknown. Other classes of CWA simulants, mainly organophosphate surrogates of sarin, will also be tested to develop a fundamental understanding of how these molecules behave on MOFs. Another important goal of future studies will be to further refine the data acquisition and analysis procedures for TPD measurements. Preliminary results indicate that diffusion rates may play an important role in temperature programmed desorption measurements that has not yet been fully accounted for in the data reported in this thesis. Therefore, future experiments will carefully explore how diffusion through the MOF affects TPD measurements.

The work on UiO-66 presented in this thesis was an important component of a multi-university initiative that is the first research program in fundamental surface science geared entirely toward developing a comprehensive understanding of the reaction mechanisms and kinetics that govern chemistry within MOFs. Previously, the vast majority of MOF-based catalysts were developed through chemical intuition and an Edisonian approach to new materials. Now, this field of materials science is poised for the types of large breakthroughs that tend to emerge from basic research. By deciphering how reaction pathways, efficiency, and poisoning depend on the structure and functionality of particular MOF/vapor combinations, one can then provide well-educated strategies for designing more effective systems that are tailored to achieve the desired outcome. The ultimate impact of this research will be to guide new filtration, decontamination, and soldier protection strategies.

Chapter 8: References

(1) Tucker, J. B. *War of Nerves : Chemical Warfare From World War I to Al-Qaeda*; Pantheon Books: New York, 2006.

(2) Gupta, R. C. (Ramesh C. *Handbook of Toxicology of Chemical Warfare Agents*; Elsevier/Academic Press, 2009.

(3) Sanjarmoosavi N, Sanjarmoosavi N, Shahsavan M, H.-N. M. Teratogenic Effects of Sulfur Mustard on Mice Fetuses. *Iran J Basic Med Sci.* **2012**, *15* (3), 853–859.

(4) Hague, T. Convention on the Prohibition of the Development, Production, Stockpiling and Use of Chemical Weapons and on Their Destruction. The Hague 2005.

(5) Brevett, C. A. S.; Sumpter, K. B.; Wagner, G. W.; Rice, J. S. Degradation of the Blister Agent Sulfur Mustard, bis(2-Chloroethyl) Sulfide, on Concrete. *J. Hazard. Mater.* **2007**, *140* (1–2), 353–360.

(6) Bartelt-Hunt, S. L.; Barlaz, M. A.; Knappe, D. R.; Kjeldsen, P. Fate of Chemical Warfare Agents and Toxic Industrial Chemicals in Landfills. *Environ. Sci. Technol.* **2006**, *40* (13), 4219–4225.

(7) Saunders, S. E.; Bartz, J. C.; Bartelt-Hunt, S. L. Influence of Prion Strain on Prion Protein Adsorption to Soil in a Competitive Matrix. *Environ. Sci. Technol.* **2009**, *43* (14), 5242–5248.

(8) Bartelt-Hunt, S. L.; Knappe, D. R. U.; Barlaz, M. A. A Review of Chemical Warfare Agent Simulants for the Study of Environmental Behavior. *Crit. Rev. Environ. Sci. Technol.* **2008**, *38* (2), 112–136.

(9) Jain, A. K.; Tewari-Singh, N.; Gu, M.; Inturi, S.; White, C. W.; Agarwal, R. Sulfur Mustard Analog, 2-Chloroethyl Ethyl Sulfide-Induced Skin Injury Involves DNA Damage and

Induction of Inflammatory Mediators, in Part via Oxidative Stress, in SKH-1 Hairless Mouse Skin. *Toxicol. Lett.* **2011**, *205* (3), 293–301.

(10) Riviere, J. E.; Smith, C. E.; Budsaba, K.; Brooks, J. D.; Olajos, E. J.; Salem, H.; Monteiro-Riviere, N. A. Use of Methyl Salicylate as a Simulant to Predict the Percutaneous Absorption of Sulfur Mustard. *J. Appl. Toxicol.* **2001**, *21* (2), 91–99.

(11) Willis, M. P.; Varady, M. J.; Pearl, T. P.; Fouse, J. C.; Riley, P. C.; Mantooth, B. A.; Lalain, T. A. Physics-Based Agent to Simulant Correlations for Vapor Phase Mass Transport. *J. Hazard. Mater.* **2013**, *263*, 479–485.

(12) Saxena, A.; Srivastava, A. K.; Singh, B. Kinetics of Adsorption of 2-CEES and HD on Impregnated Silica Nanoparticles Under Static Conditions. *AIChE J.* **2009**, *55* (5), 1236–1245.

(13) FACTS & FIGURES FOR THE CHEMICAL INDUSTRY. *Chem. Eng. News Arch.* **2003**, *81* (27), 25–66.

(14) Panayotov, D. A.; Paul, D. K.; Yates, J. T. Photocatalytic Oxidation of 2-Chloroethyl Ethyl Sulfide on TiO2-SiO2 Powders. *J. Phys. Chem. B* **2003**, *107* (38), 10571–10575.

(15) Ugliengo, P.; Sodupe, M.; Musso, F.; Bush, I. J.; Orlando, R.; Dovesi, R. Realistic Models of Hydroxylated Amorphous Silica Surfaces and MCM-41 Mesoporous Material Simulated by Large-Scale Periodic B3LYP Calculations. *Adv. Mater.* **2008**, *20* (23), 4579–4583.

(16) Rimola, A.; Costa, D.; Sodupe, M.; Lambert, J.-F.; Ugliengo, P. Silica Surface Features and Their Role in the Adsorption of Biomolecules: Computational Modeling and Experiments. *Chem. Rev.* **2013**, *113* (6), 4216–4313.

(17) Tsyganenko M.A., A. A. . B. Infrared Spectrum of Ammonia Adsorbed by Si-OH Groups on a Silica Surface. *Opt. Spectrosc.* **1983**, *54* (6), 665–666.

(18) Civalleri, B.; Ugliengo, P. First Principles Calculations of the Adsorption of NH3 on a Periodic Model of the Silica Surface. *J. Phys. Chem. B* **2000**, *104* (40), 9491–9499.

(19) Tsubomura, H. Nature of the Hydrogen Bond. III. The Measurement of the Infrared Absorption Intensities of Free and Hydrogen-Bonded OH Bands. Theory of the Increase of the Intensity Due to the Hydrogen Bond. *J. Chem. Phys.* **1956**, *24* (5), 927–931.

(20) Kjaergaard, H. G.; Garden, A. L.; Chaban, G. M.; Gerber, R. B.; Matthews, D. A.; Stanton, J. F. Calculation of Vibrational Transition Frequencies and Intensities in Water Dimer: Comparison of Different Vibrational Approaches. *J. Phys. Chem. A* **2008**, *112* (18), 4324–4335.

(21) Takahashi, K. Theoretical Study on the Effect of Intramolecular Hydrogen Bonding on OH Stretching Overtone Decay Lifetime of Ethylene Glycol, 1,3-Propanediol, and 1,4-Butanediol. *Phys. Chem. Chem. Phys.* **2010**, *12* (42), 13950–13961.

(22) Morita, M.; Takahashi, K. Theoretical Study on the Difference of OH Vibrational Spectra Between OH-(H2O)(3) and OH-(H2O)(4). *Phys. Chem. Chem. Phys.* **2012**, *14* (8), 2797–2808.

(23) Petkovic, M. O-H Stretch in Phenol and Its Hydrogen-Bonded Complexes: Band Position and Relaxation Pathways. *J. Phys. Chem. A* **2012**, *116* (1), 364–371.

(24) Wilkinson, C. by A. D. M. and A. IUPAC. Compendium of Chemical Terminology.

(25) Weinhold, F.; Klein, R. A. What Is a Hydrogen Bond? Mutually Consistent Theoretical and Experimental Criteria for Characterizing H-Bonding Interactions. *Mol. Phys.* **2012**, *110* (9–10), 565–579.

(26) Arunan, E.; Desiraju, G. R.; Klein, R. a.; Sadlej, J.; Scheiner, S.; Alkorta, I.; Clary, D. C.; Crabtree, R. H.; Dannenberg, J. J.; Hobza, P.; et al. Definition of the Hydrogen Bond

(IUPAC Recommendations 2011). *Pure Appl. Chem.* **2011**, *83* (8), 1637.

(27) Wagner, G. W.; Bartram, P. W.; Koper, O.; Klabunde, K. J. Reactions of VX, GD, and HD with Nanosize MgO. *J. Phys. Chem. B* **1999**, *103* (16), 3225–3228.

(28) Panayotov, D. A.; Morris, J. R. Uptake of a Chemical Warfare Agent Simulant (DMMP) on TiO2: Reactive Adsorption and Active Site Poisoning. *Langmuir* **2009**, *25* (6), 3652–3658.

(29) Barth, H.-D. D.; Buchhold, K.; Djafari, S.; Reimann, B.; Lommatzsch, U.; Brutschy, B. Hydrogen Bonding in (Substituted Benzene)·(Water)n Clusters with n≤4. *Chem. Phys.* **1998**, *239* (1–3), 49–64.

(30) Kandziolka, M. V; Kidder, M. K.; Gill, L.; Wu, Z.; Savara, A. Aromatic-Hydroxyl Interaction of an Alpha-Aryl Ether Lignin Model-Compound on SBA-15, Present at Pyrolysis Temperatures. *Phys. Chem. Chem. Phys.* **2014**, *16* (44), 24188–24193.

(31) Mishra, B. K.; Karthikeyan, S.; Ramanathan, V. Tuning the C–H···π Interaction by Different Substitutions in Benzene–Acetylene Complexes. *J. Chem. Theory Comput.* **2012**, *8* (6), 1935–1942.

(32) Nagao, M.; Suda, Y.; Sudat, Y. Adsorption of Benzene, Toluene, and Chlorobenzene on Titanium Dioxide. *Langmuir* **1989**, *5* (1), 42–47.

(33) Pohle, W. Infrared Study of the Adsorption of Aromatic Molecules onto Silica and Chlorinated Silica. Application of the Charge-Transfer Theory to the Data. *J. Chem. Soc. Faraday Trans. 1 Phys. Chem. Condens. Phases* **1982**, *78* (7), 2101–2109.

(34) Saggu, M.; Levinson, N. M.; Boxer, S. G. Experimental Quantification of Electrostatics in X − H ⋯ π Hydrogen Bonds. **2012**.

(35) Saggu, M.; Levinson, N. M.; Boxer, S. G. Direct Measurements of Electric Fields in Weak

OH···π Hydrogen Bonds. *J. Am. Chem. Soc.* **2011**, *133* (43), 17414–17419.

(36) Zecchina, A.; Versino, C.; Appiano, A.; Occhiena, G. Infrared Study of Benzene Adsorption on Aerosil. *J. Phys. Chem.* **1968**, *72* (5), 1471–1474.

(37) Pinto, M. L.; Pires, J. Porous and Hybrid Clay Based Materials for Separation of Hydrocarbons. *Microporous Mesoporous Mater.* **2012**, *151* (0), 403–410.

(38) Derewenda, Z. S.; Lee, L.; Derewenda, U. The Occurrence of C-H...O Hydrogen Bonds in Proteins. *J. Mol. Biol.* **1995**, *252* (2), 248–262.

(39) Badger, R. M.; Bauer, S. H. Spectroscopic Studies of the Hydrogen Bond. II. The Shift of the O–H Vibrational Frequency in the Formation of the Hydrogen Bond. *J. Chem. Phys.* **1937**, *5* (11), 839–851.

(40) Wilmsmeyer, A. R.; Gordon, W. O.; Davis, E. D.; Troya, D.; Mantooth, B. A.; Lalain, T. A.; Morris, J. R. Infrared Spectra and Binding Energies of Chemical Warfare Nerve Agent Simulants on the Surface of Amorphous Silica. *J. Phys. Chem. C* **2013**, *117* (30), 15685–15697.

(41) Wilmsmeyer, A. R.; Uzarski, J.; Barrie, P. J.; Morris, J. R. Interactions and Binding Energies of Dimethyl Methylphosphonate and Dimethyl Chlorophosphate with Amorphous Silica. *Langmuir* **2012**, *28* (30), 10962–10967.

(42) Badger, R. M. A Relation Between Internuclear Distances and Bond Force Constants. *J. Chem. Phys.* **1934**, *2* (3), 128–131.

(43) Freindorf, M.; Kraka, E.; Cremer, D. A Comprehensive Analysis of Hydrogen Bond Interactions Based on Local Vibrational Modes. *Int. J. Quantum Chem.* **2012**, *112* (19), 3174–3187.

(44) Panayotov, D.; Yates, J. T. Bifunctional Hydrogen Bonding of 2-Chloroethyl Ethyl Sulfide

on TiO2-SiO2 Powders. *J. Phys. Chem. B* **2003**, *107* (38), 10560–10564.

(45) Thompson, T. L.; Panayotov, D. A.; Yates, J. T. Adsorption and Thermal Decomposition of 2-Chloroethyl Ethyl Sulfide on TiO2 Surfaces. *J. Phys. Chem. B* **2004**, *108* (43), 16825–16833.

(46) Thompson, T. L.; Panayotov, D. A.; Yates, J. T.; Martyanov, I.; Klabunde, K. Photodecomposition of Adsorbed 2-Chloroethyl Ethyl Sulfide on TiO2: Involvement of Lattice Oxygen. *J. Phys. Chem. B* **2004**, *108* (46), 17857–17865.

(47) Tait, S. L.; Dohnálek, Z.; Campbell, C. T.; Kay, B. D. N-Alkanes on MgO(100). II. Chain Length Dependence of Kinetic Desorption Parameters for Small N -Alkanes. *J. Chem. Phys.* **2005**, *122* (16), 1–13.

(48) Bartmess, J. E.; Mallard, W. G.; Lindstrom, P. J. *NIST Chemistry WebBook*; 2005; Vol. 69.

(49) Aparicio, S.; Alcalde, R. On the Structure of Liquid Methyl Salicylate: The Role of Intramolecular Hydrogen Bonding. *Eur. J. Chem.* **2010**, *1* (3), 162–167.

(50) molinspiration http://www.molinspiration.com/cgi-bin/properties (accessed Oct 12, 2016).

(51) A.D. McNaught, A. W. IUPAC Compendium of Chemical Terminology; Royal Society of Chemistry: Cambridge, UK, 1997.

(52) Varsányi, G. and S. S. *Vibrational Spectra of Benzene Derivatives*; Academic Press: New York, 1969.

(53) Rosenthal, J.; Schuster, D. I. The Anomalous Reactivity of Fluorobenzene in Electrophilic Aromatic Substitution and Related Phenomena. *J. Chem. Educ.* **2003**, *80* (6), 679.

(54) Ghosh, P.; Colon, Y. J.; Snurr, R. Q. Water Adsorption in UiO-66: The Importance of Defects. *Chem. Commun.* **2014**, *50* (77), 11329–11331.

(55) Moon, S. Y.; Wagner, G. W.; Mondloch, J. E.; Peterson, G. W.; DeCoste, J. B.; Hupp, J.

T.; Farha, O. K. Effective, Facile, and Selective Hydrolysis of the Chemical Warfare Agent VX Using Zr6-Based Metal-Organic Frameworks. *Inorg. Chem.* **2015**, *54* (22), 10829–10833.

(56) Banerjee, D.; Simon, C. M.; Plonka, A. M.; Motkuri, R. K.; Liu, J.; Chen, X.; Smit, B.; Parise, J. B.; Haranczyk, M.; Thallapally, P. K. Metal-Organic Framework with Optimally Selective Xenon Adsorption and Separation. *Nat. Commun.* **2016**, *7* (May), ncomms11831.

(57) Plonka, A. M.; Chen, X.; Wang, H.; Krishna, R.; Dong, X.; Banerjee, D.; Woerner, W. R.; Han, Y.; Li, J.; Parise, J. B. Light Hydrocarbon Adsorption Mechanisms in Two Calcium-Based Microporous Metal Organic Frameworks. *Chem. Mater.* **2016**, *28* (6), 1636–1646.

(58) Sumida, K.; Rogow, D. L.; Mason, J. A.; McDonald, T. M.; Bloch, E. D.; Herm, Z. R.; Bae, T. H.; Long, J. R. Carbon Dioxide Capture in Metal-Organic Frameworks. *Chem. Rev.* **2012**, *112* (2), 724–781.

(59) Suh, M. P.; Park, H. J.; Prasad, T. K.; Lim, D.-W. Hydrogen Storage in Metal-Organic Frameworks. *Chem. Rev.* **2011**, *112* (20), 782–835.

(60) Decoste, J. B.; Peterson, G. W. Metal-Organic Frameworks for Air Purification of Toxic Chemicals. *Chem. Rev.* **2014**, *114* (11), 5695–5727.

(61) Furukawa, H.; Cordova, K. E.; O'Keeffe, M.; Yaghi, O. M. The Chemistry and Applications of Metal-Organic Frameworks. *Science (80-.).* **2013**, *341* (August), 974.

(62) Lee, J.; Farha, O. K.; Roberts, J.; Scheidt, K. A.; Nguyen, S. T.; Hupp, J. T.; Hoskins, B. F.; Robson, R.; Fujita, M.; Kwon, Y. J.; et al. Metal–organic Framework Materials as Catalysts. *Chem. Soc. Rev.* **2009**, *38* (5), 1450.

(63) Stassen, I.; Bueken, B.; Reinsch, H.; Oudenhoven, J.; Wouters, D.; Hajek, J.; Van Speybroeck, V.; Stock, N.; Vereecken, P. M.; Van Schaijk, R.; et al. Towards Metal-

Organic Framework Based Field Effect Chemical Sensors: UiO-66-NH $_2$ for Nerve Agent Detection. *Chem. Sci.* **2016**, *111*, 5345–5403.

(64) Moon, S. Y.; Liu, Y.; Hupp, J. T.; Farha, O. K. Instantaneous Hydrolysis of Nerve-Agent Simulants with a Six-Connected Zirconium-Based Metal-Organic Framework. *Angew. Chemie - Int. Ed.* **2015**, *66*, 6795–6799.

(65) Mondloch, J. E.; Katz, M. J.; Isley III, W. C.; Ghosh, P.; Liao, P.; Bury, W.; Wagner, G. W.; Hall, M. G.; Decoste, J. B.; Peterson, G. W.; et al. Destruction of Chemical Warfare Agents Using Metal–organic Frameworks. *Nat. Mater.* **2015**, *14* (March), 512–516.

(66) Liu, Y.; Howarth, A. J.; Hupp, J. T.; Farha, O. K. Selective Photooxidation of a Mustard-Gas Simulant Catalyzed by a Porphyrinic Metal-Organic Framework. *Angew. Chemie - Int. Ed.* **2015**, *54* (31), 9001–9005.

(67) Ming, Y.; Purewal, J.; Yang, J.; Xu, C.; Soltis, R.; Warner, J.; Veenstra, M.; Gaab, M.; Müller, U.; Siegel, D. J. Kinetic Stability of MOF-5 in Humid Environments: Impact of Powder Densification, Humidity Level, and Exposure Time. *Langmuir* **2015**, *31* (17), 4988–4995.

(68) Todaro, M.; Buscarino, G.; Sciortino, L.; Alessi, A.; Messina, F.; Taddei, M.; Ranocchiari, M.; Cannas, M.; Gelardi, F. M. Decomposition Process of Carboxylate MOF HKUST-1 Unveiled at the Atomic Scale Level. *J. Phys. Chem. C* **2016**, *120* (23), 12879–12889.

(69) Shearer, G. C.; Chavan, S.; Ethiraj, J.; Vitillo, J. G.; Svelle, S.; Olsbye, U.; Lamberti, C.; Bordiga, S.; Lillerud, K. P. Tuned to Perfection: Ironing out the Defects in Metal-Organic Framework UiO-66. *Chem. Mater.* **2014**, *26* (14), 4068–4071.

(70) Mondloch, J. E.; Katz, M. J.; Planas, N.; Semrouni, D.; Gagliardi, L.; Hupp, J. T.; Farha, O. K. Are Zr6-Based MOFs Water Stable? Linker Hydrolysis vs. Capillary-Force-Driven

Channel Collapse. *Chem. Commun.* **2014**, 8944–8946.

(71) Bai, Y.; Dou, Y.; Xie, L.-H.; Rutledge, W.; Li, J.-R.; Zhou, H.-C. Zr-Based Metal–organic Frameworks: Design, Synthesis, Structure, and Applications. *Chem. Soc. Rev.* **2016**, *45* (8), 2327–2367.

(72) Cavka, J. H.; Jakobsen, S.; Olsbye, U.; Guillou, N.; Lamberti, C.; Bordiga, S.; Lillerud, K. P. A New Zirconium Inorganic Building Brick Forming Metal Organic Frameworks with Exceptional Stability. *J. Am. Chem. Soc.* **2008**, *130* (42), 13850–13851.

(73) Valenzano, L.; Civalleri, B.; Chavan, S.; Bordiga, S.; Nilsen, M. H.; Jakobsen, S.; Lillerud, K. P.; Lamberti, C. Disclosing the Complex Structure of UiO-66 Metal Organic Framework: A Synergic Combination of Experiment and Theory. *Chem. Mater.* **2011**, *23* (7), 1700–1718.

(74) Wu, H.; Chua, Y. S.; Krungleviciute, V.; Tyagi, M.; Chen, P.; Yildirim, T.; Zhou, W. Unusual and Highly Tunable Missing-Linker Defects in Zirconium Metal–Organic Framework UiO-66 and Their Important Effects on Gas Adsorption. *J. Am. Chem. Soc.* **2013**, *135* (28), 10525–10532.

(75) Ghosh, P.; Colon, Y. J.; Snurr, R. Q. Water Adsorption in UiO-66: The Importance of Defects. *Chem. Commun.* **2014**, *50* (77), 11329–11331.

(76) Yildirim, T.; Hartman, M. R. Direct Observation of Hydrogen Adsorption Sites and Nanocage Formation in Metal-Organic Frameworks. *Phys. Rev. Lett.* **2005**, *95* (21), 3–6.

(77) Mondloch, J. E.; Katz, M. J.; Isley III, W. C.; Ghosh, P.; Liao, P.; Bury, W.; Wagner, G. W.; Hall, M. G.; Decoste, J. B.; Peterson, G. W.; et al. Destruction of Chemical Warfare Agents Using Metal–organic Frameworks. *Nat. Mater.* **2015**, *14* (March), 512–516.

(78) Katz, M. J.; Brown, Z. J.; Colón, Y. J.; Siu, P. W.; Scheidt, K. a; Snurr, R. Q.; Hupp, J. T.;

Farha, O. K. A Facile Synthesis of UiO-66, UiO-67 and Their Derivatives. *Chem. Commun. (Camb).* **2013**, *49* (82), 9449–9451.

(79) Abelard, J.; Wilmsmeyer, A. R.; Edwards, A. C.; Gordon, W. O.; Durke, E. M.; Karwacki, C. J.; Troya, D.; Morris, J. R. Adsorption of 2-Chloroethyl Ethyl Sulfide on Silica: Binding Mechanism and Energy of a Bifunctional Hydrogen-Bond Acceptor at the Gas–Surface Interface. *J. Phys. Chem. C* **2014**, *119* (1), 365–372.

(80) Abelard, J.; Wilmsmeyer, A. R.; Edwards, A. C.; Gordon, W. O.; Durke, E. M.; Karwacki, C. J.; Troya, D.; Morris, J. R. Adsorption of Substituted Benzene Derivatives on Silica: Effects of Electron Withdrawing and Donating Groups. *J. Phys. Chem. C* **2016**, *120* (24), 13024–13031.

(81) Tait, S. L.; Dohnalek, Z.; Campbell, C. T.; Kay, B. D. N-Alkanes on MgO(100). I. Coverage-Dependent Desorption Kinetics of N-Butane. *J. Chem. Phys.* **2005**, *122* (16).

(82) Uzarski, J. R. Reflection Absorption Infrared Spectroscopic Studies of Surface Chemistry Relevant to Chemical and Biological Warfare Agent Defense, Virginia Polytechnic Institute and State University: Ann Arbor, 2009.

(83) Wilmsmeyer, A. R. Ultrahigh Vacuum Studies of the Fundamental Interactions of Chemical Warfare Agents and Their Simulants with Amorphous Silica, Virginia Polytechnic Institute and State University: Ann Arbor, 2012.

(84) Panayotov, D. A.; Yates, J. T. Spectroscopic Detection of Hydrogen Atom Spillover from Au Nanoparticles Supported on TiO2: Use of Conduction Band Electrons. *J. Phys. Chem. C* **2007**, *111* (7), 2959–2964.

(85) Kandiah, M.; Nilsen, M. H.; Usseglio, S.; Jakobsen, S.; Olsbye, U.; Tilset, M.; Larabi, C.; Quadrelli, E. A.; Bonino, F.; Lillerud, K. P.; et al. Synthesis and Stability of Tagged UiO-

66 Zr-MOFs. **2010**, No. 10, 6632–6640.

(86) Dijkstra, T. W.; Duchateau, R.; van Santen, R. A.; Meetsma, A.; Yap, G. P. A. Silsesquioxane Models for Geminal Silica Surface Silanol Sites. A Spectroscopic Investigation of Different Types of Silanols. *J. Am. Chem. Soc.* **2002**, *124* (33), 9856–9864.

(87) Ghiotti, G.; Garrone, E.; Morterra, C.; Boccuzzi, F. Infrared Study of Low Temperature Adsorption. 1. Carbon Monoxide on Aerosil. An Interpretation of the Hydrated Silica Spectrum. *J. Phys. Chem.* **1979**, *83* (22), 2863–2869.

(88) Hoffmann, P.; Knözinger, E. Novel Aspects of Mid and Far IR Fourier Spectroscopy Applied to Surface and Adsorption Studies on SiO2. *Surf. Sci.* **1987**, *188* (1–2), 181–198.

(89) Van Roosmalen, A. J.; Mol, J. C. An Infrared Study of the Silica Gel Surface. 1. Dry Silica Gel. *J. Phys. Chem.* **1978**, *82* (25), 2748–2751.

(90) Zhuravlev, L. T. The Surface Chemistry of Amorphous Silica. Zhuravlev Model. *Colloids Surfaces A Physicochem. Eng. Asp.* **2000**, *173* (1–3), 1–38.

(91) NIST ITS-90 Thermocouple Database http://srdata.nist.gov/its90/main/ (accessed Jun 30, 2016).

(92) Mosaic Documentation Web, Type K Thermocouple Calibration http://www.mosaic-industries.com/embedded-systems/microcontroller-projects/temperature-measurement/thermocouple/type-k-calibration-table (accessed Jun 30, 2016).

(93) McQuarrie, D. Statistical Mechanics. *StatMechBook*. 1976.

(94) Zubkov, T.; Smith, R. S.; Engstrom, T. R.; Kay, B. D. Adsorption, Desorption, and Diffusion of Nitrogen in a Model Nanoporous Material. I. Surface Limited Desorption Kinetics in Amorphous Solid Water. *J. Chem. Phys.* **2007**, *127* (18).

(95) Zubkov, T.; Smith, R. S.; Engstrom, T. R.; Kay, B. D. Adsorption, Desorption, and

Diffusion of Nitrogen in a Model Nanoporous Material. II. Diffusion Limited Kinetics in Amorphous Solid Water. *J. Chem. Phys.* **2007**, *127* (18), 184708.

(96) W.E. Acree J.S. Chickos, J. No Title. In *NIST Chemistry WebBook, NIST Standard Reference Database Number 69*; Mallard, P. J. L. and W. G., Ed.; National Institute of Standards and Technology: Gaithersburg MD, 20899.

(97) Jędrzejewski-Szmek, Z.; Muftakhidinov, B.; Winchen, T.; Trande, A.; Weingrill, J.; Lane, D. Engauge Digitizer. 2016.

(98) Zubkov, T.; Smith, R. S.; Engstrom, T. R.; Kay, B. D. Adsorption, Desorption, and Diffusion of Nitrogen in a Model Nanoporous Material. I. Surface Limited Desorption Kinetics in Amorphous Solid Water. *J. Chem. Phys.* **2007**, *127* (18).

(99) McDonald, R. S. Surface Functionality of Amorphous Silica by Infrared Spectroscopy. *J. Phys. Chem.* **1958**, *62* (10), 1168–1178.

(100) Takei, T.; Kato, K.; Meguro, A.; Chikazawa, M. Infrared Spectra of Geminal and Novel Triple Hydroxyl Groups on Silica Surface. *Colloids Surfaces A* **1999**, *150* (1–3), 77–84.

(101) Daschbach, J. L.; Kim, J.; Ayotte, P.; Smith, R. S.; Kay, B. D. Adsorption and Desorption of HCl on Pt(111). *J. Phys. Chem. B* **2005**, *109* (32), 15506–15514.

(102) Ramesh, S. G.; Re, S.; Hynes, J. T. Charge Transfer and OH Vibrational Frequency Red Shifts in Nitrate−water Clusters. *J. Phys. Chem. A* **2008**, *112* (15), 3391–3398.

(103) Cioslowski, J.; Liu, G. H.; Castro, R. A. M. Badger's Rule Revisited. *Chem. Phys. Lett.* **2000**, *331* (5–6), 497–501.

(104) Joshi, R.; Ghanty, T. K.; Mukherjee, T. Substituent Effect on Ionization Potential, O-H Bond Dissociation Energy and Intra-Molecular Hydrogen Bonding in Salicylic Acid Derivatives. *J. Mol. Struct.* **2010**, *948* (1–3), 47–54.

(105) Rivera-Rivera, L. A.; McElmurry, B. A.; Scott, K. W.; Lucchese, R. R.; Bevan, J. W. The Badger-Bauer Rule Revisited: Correlation of Proper Blue Frequency Shifts in the OC Hydrogen Acceptor with Morphed Hydrogen Bond Dissociation Energies in OC-HX (X = F, Cl, Br, I, CN, CCH). *J. Phys. Chem. A* **2013**, *117* (35), 8477–8483.

(106) Edwards, A. *Guassian Calculations Performed Using Gaussian 09 Package Focusing on the Method B97D*; 2014.

(107) Bermudez, V. M. Computational Study of the Adsorption of Trichlorophosphate, Dimethyl Methylphosphonate, and Sarin on Amorphous SiO2. *J. Phys. Chem. C* **2007**, *111* (26), 9314–9323.

(108) Tait, S. L.; Dohnalek, Z.; Campbell, C. T.; Kay, B. D. N-Alkanes on MgO(100). II. Chain Length Dependence of Kinetic Desorption Parameters for Small N-Alkanes. *J. Chem. Phys.* **2005**, *122* (16).

(109) Bratos, S. Profiles of Hydrogen Stretching IR Bands of Molecules with Hydrogen-Bonds - Stochastic Theory .1. Weak and Medium Strength Hydrogen-Bonds. *J. Chem. Phys.* **1975**, *63* (8), 3499–3509.

(110) Bratos, S.; Ratajczak, H. Profiles of Hydrogen Stretching IR Bands of Molecules with Hydrogen-Bonds - A Stochastic-Theory .2. Strong Hydrogen-Bonds. *J. Chem. Phys.* **1982**, *76* (1), 77–85.

(111) Hertl, W.; Hair, M. L. Hydrogen Bonding Between Adsorbed Gases and Surface Hydroxyl Groups on Silica. *J. Phys. Chem.* **1968**, *72* (13), 4676–4682.

(112) Mawhinney, D. B.; Rossin, J. A.; Gerhart, K.; Yates, J. T. Adsorption and Reaction of 2-Chloroethylethyl Sulfide with Al2O3 Surfaces. *Langmuir* **1999**, *15* (14), 4789–4795.

(113) Murthy, A. S. N.; Rao, C. N. R. Spectroscopic Studies of the Hydrogen Bond. *Appl.*

Spectrosc. Rev. **1968**, *2* (1), 69–191.

(114) Rao, C. N. R.; Dwivedi, P. C.; Ratajczak, H.; Orvillethomas, W. J. Relation Between O-H Stretching Frequency and Hydrogen-Bond Energy - Re-Examination of Badger-Bauer Rule. *J. Chem. Soc. Trans. Ii* **1975**, *71*, 955–966.

(115) Ratajczak, H.; Orvillethomas, W. J. Charge-Transfer Properties of Hydrogen-Bonds .6. Charge-Transfer Theory and Dipole-Moments of Hydrogen-Bonded Complexes. *J. Mol. Struct.* **1975**, *26* (2), 387–391.

(116) Ratajczak, H.; Orvillethomas, W. J.; Rao, C. N. R. Charge-Transfer Properties of Hydrogen-Bonds - Relations Between Vibrational-Spectra and Energy of Hydrogen-Bonds. *Chem. Phys.* **1976**, *17* (2), 197–216.

(117) Bertilsson, L.; Engquist, I.; Liedberg, B. Interaction of Dimethyl Methylphosphonate with Alkanethiolate Monolayers Studied by Temperature-Programmed Desorption and Infrared Spectroscopy. *J. Phys. Chem. B* **1997**, *101* (31), 6021–6027.

(118) Wheeler, S. E. Understanding Substituent Effects in Noncovalent Interactions Involving Aromatic Rings. *Acc. Chem. Res.* **2012**, *46* (4), 1029–1038.

(119) Bloom, J. W. G.; Raju, R. K.; Wheeler, S. E. Physical Nature of Substituent Effects in XH/π Interactions. *J. Chem. Theory Comput.* **2012**, *8* (9), 3167–3174.

(120) NIST Mass Spec Data Center director, S. E. S. NIST Chemistry WebBook, NIST Standard Reference Database Number 69; Mallard, P. J. L. and W. G., Ed.; Gaithersburg MD, 20899.

(121) Taylor, D. E.; Runge, K.; Cory, M. G.; Burns, D. S.; Vasey, J. L.; Hearn, J. D.; Henley, M. V. Binding of Small Molecules to a Silica Surface: Comparing Experimental and Theoretical Results. *J. Phys. Chem. C* **2011**, *115* (50), 24734–24742.

(122) Frisch, M. J.; Trucks, G. W.; Schlegel, H. B.; Scuseria, G. E.; Robb, M. A.; Cheeseman, J.

R.; Scalmani, G.; Barone, V.; Mennucci, B.; Petersson, G. A.; et al. Gaussian 09. Gaussian, Inc.: Wallingford, CT, USA 2009.

(123) Troya, D. *Guassian Calculations Performed Using Gaussian 09 Package Focusing on the Method B97D*; 2015.

(124) Weinhold, F.; Landis, C. R. *Valency and Bonding: A Natural Bond Orbital Donor-Acceptor Perspective*; Cambridge University Press, 2005.

(125) Rimola, A.; Civalleri, B.; Ugliengo, P. Physisorption of Aromatic Organic Contaminants at the Surface of Hydrophobic/hydrophilic Silica Geosorbents: A B3LYP-D Modeling Study. *Phys. Chem. Chem. Phys.* **2010**, *12* (24), 6357–6366.

(126) Nikolova, V.; Ilieva, S.; Galabov, B.; Schaefer, H. F.; Schaefer 3rd, H. F. Experimental Measurement and Theory of Substituent Effects in π-Hydrogen Bonding: Complexes of Substituted Phenols with Benzene. *J. Org. Chem.* **2014**, *79* (15), 6823–6831.

(127) Lee, E. C.; Kim, D.; Jurečka, P.; Tarakeshwar, P.; Hobza, P.; Kim, K. S. Understanding of Assembly Phenomena by Aromatic−Aromatic Interactions: Benzene Dimer and the Substituted Systems. *J. Phys. Chem. A* **2007**, *111* (18), 3446–3457.

(128) Yuzawa, H.; Aoki, M.; Itoh, H.; Yoshida, H. Adsorption and Photoadsorption States of Benzene Derivatives on Titanium Oxide Studied by NMR. *J. Phys. Chem. Lett.* **2011**, *2* (15), 1868–1873.

(129) Massaro, R. D.; Dai, Y.; Blaisten-barojas, E.; Uni, V. Energetics and Vibrational Analysis of Methyl Salicylate Isomers. **2009**, 10385–10390.

(130) Levitt, M.; Perutz, M. F. Aromatic Rings Act as Hydrogen Bond Acceptors. *J. Mol. Biol.* **1988**, *201* (4), 751–754.

(131) Katz, M. J.; Brown, Z. J.; Colón, Y. J.; Siu, P. W.; Scheidt, K. a; Snurr, R. Q.; Hupp, J. T.;

Farha, O. K. A Facile Synthesis of UiO-66, UiO-67 and Their Derivatives. *Chem. Commun. (Camb).* **2013**, *49* (82), 9449–9451.

(132) Øien, S.; Wragg, D.; Reinsch, H.; Svelle, S.; Bordiga, S.; Lamberti, C.; Lillerud, K. P. Detailed Structure Analysis of Atomic Positions and Defects in Zirconium Metal–Organic Frameworks. *Cryst. Growth Des.* **2014**, *14* (11), 5370–5372.

(133) Liu, J.; Powell, K. L.; Thames, H. D.; MacLeod, M. C. Detoxication of Sulfur Half-Mustards by Nucleophilic Scavengers: Robust Activity of Thiopurines. *Chem. Res. Toxicol.* **2010**, *23* (3), 488–496.

(134) Tait, S. L.; Dohnalek, Z.; Campbell, C. T.; Kay, B. D. N-Alkanes on Pt(111) and on C(0001)/Pt(111): Chain Length Dependence of Kinetic Desorption Parameters. *J. Chem. Phys.* **2006**, *125* (23), 15.

(135) Saggu, M.; Levinson, N. M.; Boxer, S. G. Experimental Quantification of Electrostatics in X–H···π Hydrogen Bonds. *J. Am. Chem. Soc.* **2012**, *134* (46), 18986–18997.